Montanuniversität Leoben

Intermetallic NiAl precipitate analysis by means of atom probe and complementary methods

Diploma thesis
by
Christoph Lerchbacher

Accomplished at the Department of Physical Metallurgy and Material Testing of the University of Leoben.

Leoben, September 2009

Affidavit

I declare in lieu of oath, that I wrote this thesis and performed the associated research myself, using only literature cited in this volume.

Leoben, September 2009 Christoph Lerchbacher

Acknowledgments

I would like to thank Univ. Prof. Dipl.-Ing. Dr.mont. Helmut Clemens for giving me the opportunity to perform my diploma thesis at the Department of Physical Metallurgy and Materials Testing at the University of Leoben.

My sincere gratitude is due to my supervisors Dipl.-Ing. Dr.mont. Harald Leitner and Dipl.-Ing. Michael Schober for assigning this work to me. My special thanks go to Michael Schober, for the detailed discussions, his guidance and finally his endless patience and energy he invested in me and my diploma thesis.

Furthermore, I would like to express my thanks to Dipl.-Ing. Elisabeth Eidenberger for introducing and supporting me in all SANS affairs, and for correcting my sometime amateurish English.

My thanks are due to all colleagues of the Department of Physical Metallurgy and Materials Testing for supporting me in my experimentations.

My final and special thanks go to my family for their everlasting support throughout all my life. Without their encouragement it would have never been possible to graduate this study.

Leoben, September 2009 Christoph Lerchbacher

Abbreviations

γ	Surface energy
η	Scattering contrast
λ	Wave length
μ	Magnetic moment
ρ	Density
τ	Shear stress
Φ	Heat flow
Θ	Scattering angle
3DAP	3-dimensional atom probe
A	Area
b	Burgers vector, Nuclear scattering length
bcc	Body centered cubic
c	Concentration
d_{max}	Separation distance
DSC	Differential scanning calorimetry
e	Elementary charge
ESA	Emission spectral analysis
f	Volume fraction
F	Electric field
fcc	Face centred cubic
G	Gibbs free enthalpy, Shear modulus
GeNF	Geesthacht Neutron Facility
HV	Vickers hardness
JMA	Johnson-Mehl-Avrami
K	Calibration factor
l	Particle spacing
LRO	Long range order
m	Mass
n	Time exponent, Number density, Charge
N_{min}	Minimum number of atoms
p	Magnetic scattering length
PH	Precipitation hardened
q	Scattering vector
Q	Integral intensity, Thermal energy
r, R	Radius
R_g	Gas constant

S	…………………………………	Entropy
SANS	…………………………………	Small angle neutron scattering
SLDD	…………………………………	Scattering length density difference
SRO	…………………………………	Short range order
T	…………………………………	Temperature
t	…………………………………	Time
TEM	…………………………………	Transmission electron microscopy
Tm	…………………………………	Melting point
V	…………………………………	Volume, Voltage
VEC	…………………………………	Valence electron concentration
X	…………………………………	Mole fraction

1 Introduction

Technically relevant structural materials gain their exceptional mechanical properties from several microstructural features. One of these features is the fine dispersion of second phase particles such as precipitates which affect the dislocation mobility, thus, increasing the strength of the material. Their influence on the mechanical properties of the material is controlled by characteristics, like size distribution, shape, number density and volume fraction. The control of these characteristics by performing appropriate mechanical and thermal treatments to gain required microstructure is of great interest for materials producing and processing industry.

Investigations are preferably performed on model alloys, due to the fact that in simpler systems it is easier to identify and characterize precipitation reactions as it is in complex technical materials. The B2 ordered intermetallic NiAl phase has been identified to be responsible for strengthening effects in several Fe-based materials [1]. For reasonable simulations of the development of characteristics like composition, size, distribution or shape of the precipitates the early stages have to be understood.

Ab-initio calculations simulate nucleation and growth from nuclei consisting of a few atoms. The experimental investigations in the present work have been carried out in order to support such simulations. Due to high sensitivity and resolution especially the use of atom probe (3DAP) [2] and small-angle neutron scattering (SANS) [3] is suitable for analyzing the results of precipitation reactions. In order to obtain information on the transformation kinetics differential scanning calorimetry (DSC) provides high resolution as well. The advantage of SANS is that quantitative values like size and number density of the precipitates can be measured within a rather large volume compared to direct microscopy, such as atom probe. Additionally, the magnetic and nuclear scattering contrasts between matrix and precipitates provide information on the chemical composition development of matrix and precipitates. Implementing in-situ SANS experiments enables observing subsequent development of precipitation parameters and chemical composition. In combination with 3DAP measurements the results can be critically compared and the applicability and the accuracy of the complementary characterization methods can be assessed.

The DSC is a useful tool to investigate the alloys with respect to transformation kinetics. Information on the starting temperature of the precipitation reaction as well as transformation kinetic parameters can be gained. Since isothermal experiments are very time consuming DSC measurements have been accomplished at constant heating rates.

The intention of the present work is the characterization of the precipitation behavior of a Fe-based model alloy with additions of Al and Ni. Three ferritic alloys with different additions of Al and Ni have been produced and investigated by the mentioned characterization methods.

2 Theoretical basics

2.1 Second phase precipitation

Many technologically important properties of materials are essentially controlled by the presence of precipitated particles of a second phase. The classical procedure to achieve a precipitation reaction is to produce a supersaturated solid solution and to perform an aging treatment. The alloy is heated up into a region in the phase diagram where the solubility of the alloying element is high. Figure 2.1(a) exemplarily shows a phase diagram for a visualization of the described heat treatment. The temperature is kept for sufficient time to guarantee that all atoms of the alloying element are dissolved. After this homogenization treatment (temperature 1) the alloy is quenched and a supersaturated solid solution is present at room temperature. Subsequently, the precipitates develop during isothermal aging at a temperature that is situated in the two phase region in the phase diagram, like temperature 2 in Figure 2.1(a). The formation of the precipitates, especially distribution, size and shape are controlled by the heat treatment parameters like temperature and time. A second but unusual possibility to generate a precipitation reaction is an adjacent cooling into the two phase region immediately after homogenization. The procedure of isothermal aging is preferentially used in industrial processes as well as for scientific investigations of decomposition processes due to the fact that it is easier to handle and interpret.

The thermodynamic equilibrium is reached by minimizing Gibbs free enthalpy

$$G = H - TS \,, \tag{2-1}$$

where H is the enthalpy, T stands for the temperature and S represents the entropy [4]. In the case of a supersaturated solid solution a lowering of free enthalpy G takes place by demixing into two phases. As seen in Figure 2.1(a) the miscibility gap in the phase diagram of the binary compound consists of two regions A and B which describe different mechanisms of decomposition. The line which separates the two regions is called spinodal and the trend in the phase diagram is caused by the inflection points of the free enthalpy curves. This spinodal can only occur for the case that the two phases belong to the same G-x curve which requires that these represent the same state of matter and are solid solutions of the same crystal structure [5]. The free enthalpy is a function of temperature and therefore the curve in Figure 2.1(b) provides only the characteristic points of the phase diagram for temperature T_2 in Figure 2.1(a). The two minima in the free enthalpy curve separate the one phase (α) region from the two phase ($\alpha_1 + \alpha_2$) region in the phase diagram, whereas the two deflection points of the free enthalpy curve define the position of the spinodal. Composition X_1 and X_2 represent the equilibrium compositions of the two phases.

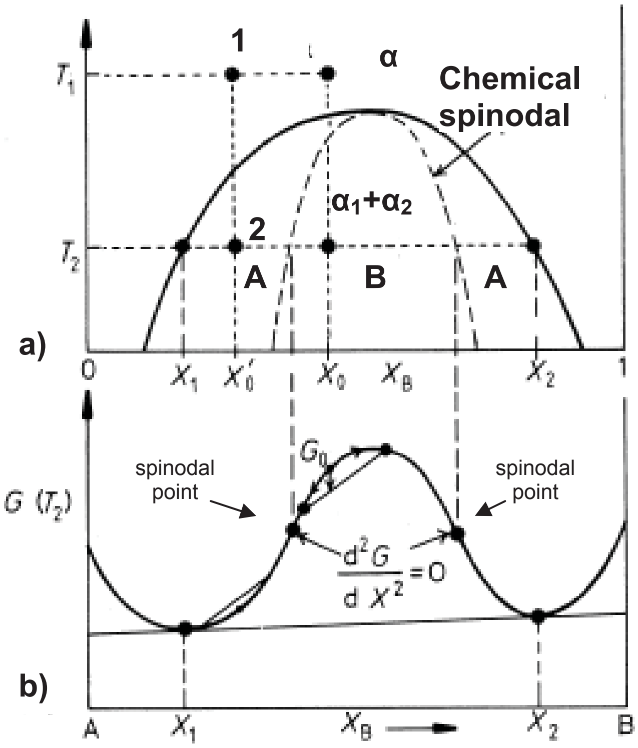

Figure 2.1: Alloys inside region B are unstable and can decompose into two coherent phases α_1 and α_2 without overcoming an activation energy barrier. The spinodal in the phase diagram is calculated from the spinodal points in the free energy curve. Alloys inside region A are metastable and can decompose only after nucleation of the second phase [6].

2.1.1 Classical Nucleation

In region A of Figure 2.1(a), the metastable region of the miscibility gap, demixing is initiated via the formation of energetically stable solute rich clusters. These are the product of thermal composition fluctuations with sufficiently large compositional amplitudes, lowering the free energy of the system. The change of the free energy ΔG has several contributions, a gain of energy ΔG_V due to building new volume of the second phase and an increase in free energy due to generating new surface and to compensate lattice difference associated strains ΔG_S. In case of heterogeneous nucleation a free energy lowering contribution ΔG_D due to defects as for example vacancies, dislocations, grain boundaries is added [7]. For the assumption of spherical clusters with a radius r and by ignoring the variation of surface energy γ with interface orientation the equation for ΔG is written as

$$\Delta G = -\frac{4}{3}\pi r^3\left(\Delta G_V - \Delta G_S\right) + 4\pi r^2\gamma - \Delta G_D \quad . \tag{2-2}$$

Differentiating equation 2-2 with respect to r allows for the calculation of the nucleation barrier $\Delta G*$ and a critical radius r* which have to be exceeded for forming stable and continuously growing nuclei.

$$r* = \frac{2\gamma}{\left(\Delta G_V - \Delta G_S\right)} \tag{2-3}$$

$$\Delta G* = \frac{16\pi\gamma^3}{3\left(\Delta G_V - \Delta G_S\right)^2} \tag{2-4}$$

An incubation period for stable nucleation is associated to this barrier, because it needs time until the formed clusters exceed the critical radius. Temperature is the most important parameter for the nucleation rate, on the one hand enough undercooling is necessary to provide sufficient driving force for the nucleation and on the other hand diffusion controlled processes require high temperatures. Figure 2.2 schematically shows the characteristics of the difference of free enthalpy ΔG with respect to the radius r. The positive surface related contribution shows a r^2 dependence, whereas the negative volume contribution has a r^3 dependence. The sum of these contributions results in the characteristic ΔG curve which yields the nucleation barrier ΔG* and the critical radius r*.

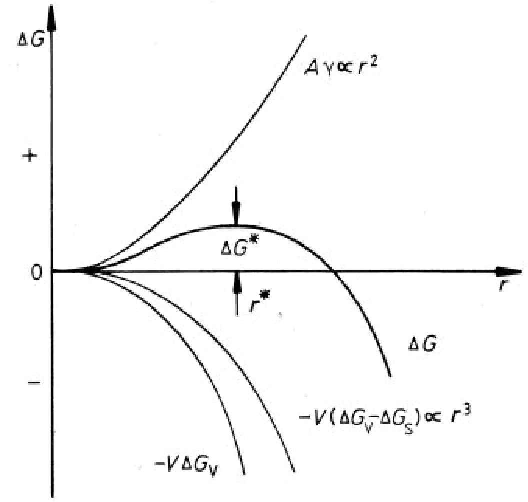

Figure 2.2: Difference in free enthalpy ΔG as a function of radius r for a homogeneous nucleus. There is an activation energy barrier $\Delta G*$ and a critical radius r* which have to be exceeded for stable growth of the nucleus [6].

In Figure 2.3 the schematic composition variation with time in case of an alloy that is aged in the metastable region of the phase diagram is represented. The compositions of Figure 2.3 are related to the compositions of Figure 2.1.

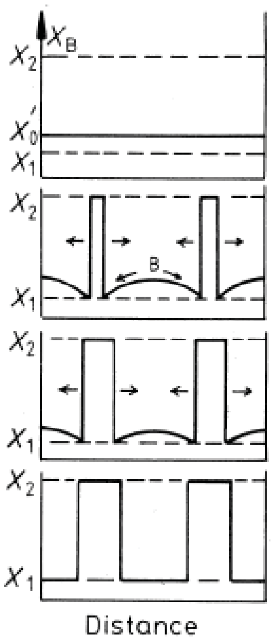

Figure 2.3: Schematic composition profiles at increasing aging times of an alloy quenched into the region outside the spinodal points [6].

It starts with the homogenized composition X_0', but with moving into the metastable region of the miscibility gap thermal composition fluctuations with high amplitudes cause clusters with equilibrium composition. B atoms from the matrix move to the clusters until the matrix reaches equilibrium composition X_1 and therefore the clusters grow.

2.1.2 Spinodal decomposition

As already mentioned region A in Figure 2.1 has been found to be metastable, region B represents an unstable state. The unstable solid solution decomposes via the spontaneous formation and subsequent growth of coherent composition fluctuations with small amplitudes. A schematic of the decomposition process is shown in Figure 2.4.

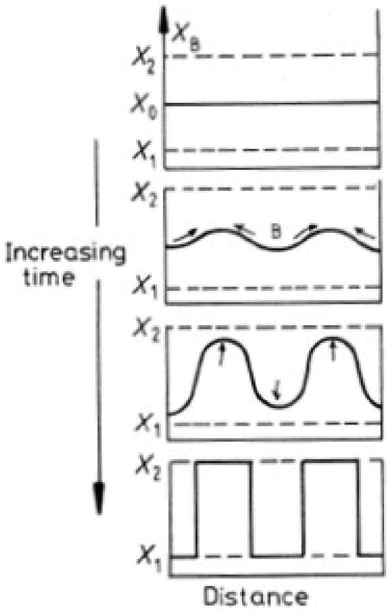

Figure 2.4: Schematic composition profiles at increasing times in an alloy quenched into the spinodal region [6].

At the beginning the matrix also has a homogenous composition of X_0. After moving into the two phase region thermal composition fluctuations with small amplitudes occur, which increase with time until they reach the equilibrium compositions X_1 and X_2 of the two phases. The process of approaching the equilibrium composition occurs in form of an uphill diffusion. B atoms move to B enriched regions in the alloy and vice versa.

In fact, the cluster kinetic models and the spinodal theories can be seen as two different approaches used to describe phase separation. Classical nucleation shows an incubation period, whereas spinodal decomposition starts spontaneously. For classical nucleation the clusters start with the equilibrium composition, whereas for spinodal decomposition the particles approach the equilibrium composition with time. The dynamics are controlled by the same mechanisms: diffusion of solute and solvent atoms, driven by the gradient of chemical potential [7].

2.1.3 Particle Growth

As described above clusters which have exceeded the critical radius r* are stable and achieve the state of growth. Figure 2.5 represents the characteristic concentration profile of the particle – matrix interface which explains classical particle growth.

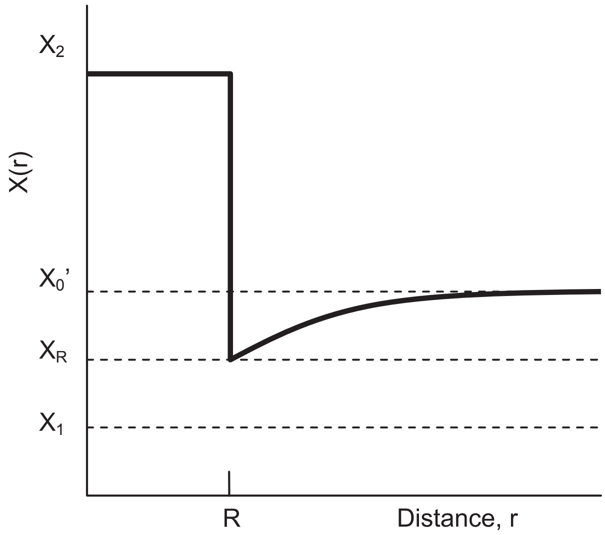

Figure 2.5: Schematic concentration field in the matrix surrounding a nucleus with radius R and composition X_2.

The profile shows four different concentrations: X_2 is the particle concentration, X_0' and X_1 are the local and the equilibrium matrix concentration, respectively, and X_R is the matrix concentration at the interface. According to the Gibbs-Thomson equation 2-5 the matrix concentration of a curved interface is a function of R

$$X_R(R) = X_1 \cdot \exp\left(\frac{2\gamma \cdot V_\beta}{R_g T} \cdot \frac{1}{R} \right), \tag{2-5}$$

where γ is the surface energy, V_β the molar volume of the second phase, R_g the gas constant and T is the absolute temperature. Due to the concentration gradient in Figure 2.5 a diffusional flow of second phase atoms from matrix to interface occurs associated with interface movement which is a synonym for particle growth [8]. The mobility of the interface depends on the kind of the interface and on the crystal structures of the two neighbouring phases. Therefore, the shape of the precipitates is controlled by the specific mobility of the interfaces. Details concerning the growth behaviour of the different interfaces can be found in [6].

The development of the volume fraction f of the second phase in equation 2-6 follows a Johnson-Mehl-Avrami law, which is a simple approach to describe several similar time dependent processes,

$$f = 1 - \exp^{(-Bt)^n}, \tag{2-6}$$

where n is a numerical exponent whose value can vary from approximately 1 to 4, and B is a function of nucleation rate and growth rate, which can be a function of time, and therefore B is sensitively dependent on temperature.

2.2 Particle strengthening

The main task of particles concerning strengthening is the decrease of dislocation mobility, thus it is important to consider the interaction mechanism of precipitate and dislocation which principally depends on the existing phase boundary and the particle radius. The characteristics of the interface that separates the growing clusters and nuclei from the matrix depend on different parameters e.g. crystal structure, interatomic distance, orientation and composition. Figure 2.6 schematically illustrates the different possible phase boundaries. In the early stages coherency (Figure 2.6(a)) is found but increasing particle radius is associated with increasing lattice misfit which causes so-called coherency strains. The result is an increase of the free energy of the system. With rising coherency strains the material has to generate misfit dislocations (Figure 2.6(b)) on the phase boundary to compensate them which leads to semi-coherent phase boundaries. Due to large misfits it can become energetically favourable to induce incoherent phase boundaries (Figure 2.6(c)), which are nearly free of strains.

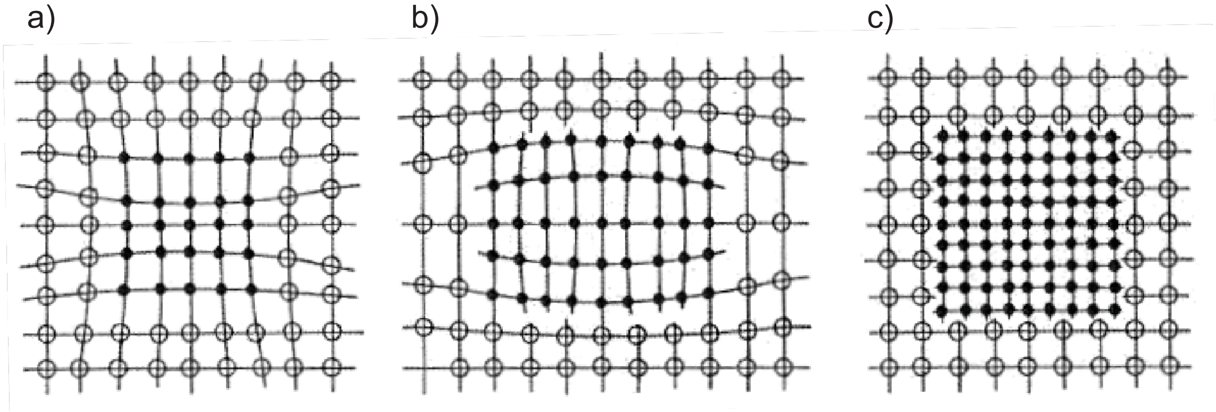

Figure 2.6: Phase boundaries a) coherent, b) semi coherent, c) incoherent [9].

In the case of coherent phase boundaries the crystallographic planes and directions in the matrix continue into the precipitate with only a slight distortion, and therefore a dislocation is able to intersect the particle. This process requires several energy inputs. The dislocation has to overcome the coherency strains. Cutting through the precipitate by the magnitude of a burgers vector causes a shift of the top part above the slip plane with respect to the bottom part. Figure 2.7 schematically depicts this process. On the one hand the result is an increase of interface, on the other hand an anti phase boundary is generated in the case of ordered phases, consuming energy. Additionally, differences in shear modulus and in stacking fault energy of matrix and precipitate have an influence on the dislocation mobility.

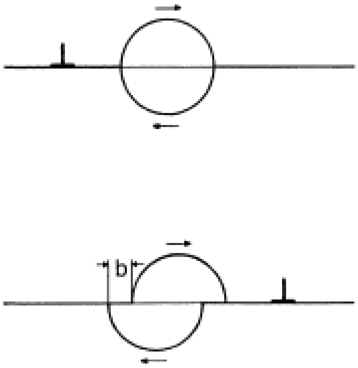

Figure 2.7: If a dislocation runs across a coherent particle, the particle is cut and shears off. Schematic [4].

The only possibility for a dislocation to pass a particle with an incoherent phase boundary at temperatures lower than 0.4 x $T_{m,}$ T_m representing the melting point, is to circumvent it. This process is known as the Orowan mechanism. Figure 2.8 shows a schematic of the Orowan mechanism. The incoming dislocation sticks to the particles causing a bulge forming of the dislocation until antiparallel segments meet behind the particle and annihilate. A dislocation loop around the particles and a free dislocation that can move on are produced. These dislocation loops cause a decrease of effective particle spacing l and according to equation 2-7 critical shear stress τ increases and the material strengthens [4]. The critical shear stress to allow for the dislocations circumventing the precipitated particles is given by

$$\tau = \frac{Gb}{l - 2r} . \qquad (2\text{-}7)$$

Shear modulus G and burgers vector b are material-specific, but particle spacing l and particle radius r and therefore the critical resolved shear stress, here the so-called Orowan stress, can be influenced by the precipitation reaction parameters.

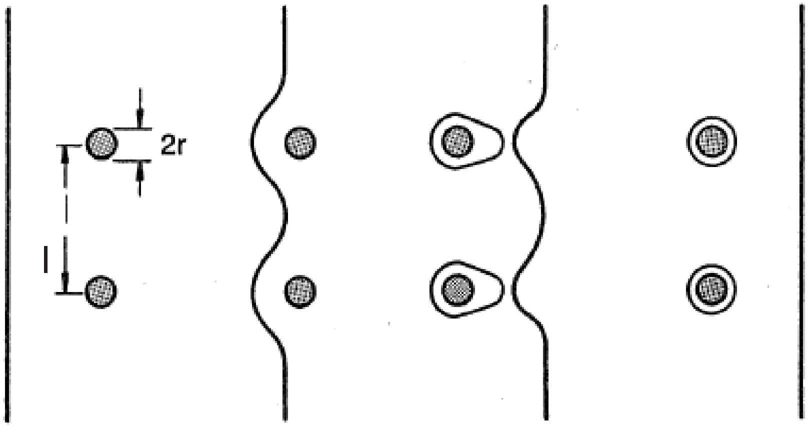

Figure 2.8: Orowan mechanism: A moving dislocation which is constrained by precipitates. Dislocation loops are built and the dislocation can move on [4].

The shear stress τ for circumventing precipitates has a $\frac{1}{r}$ dependence whereas intersection of particles shows a $\sqrt{r}$ behaviour. The combination of the two possible mechanisms leads to an optimum particle size that imparts the maximum strength of an alloy. The dependence of shear stress τ on the particle radius r is shown in Figure 2.9.

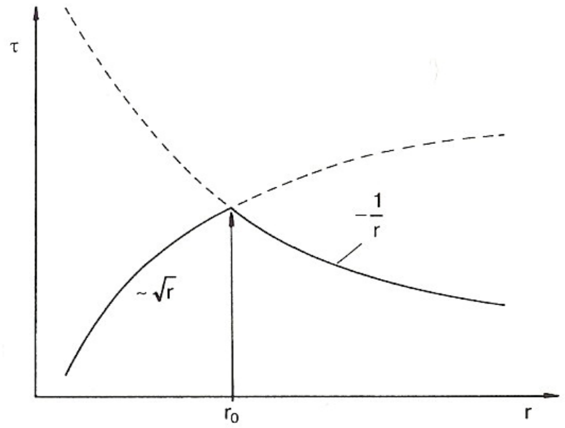

Figure 2.9: Schematic dependence of strengthening on particle size. The optimum particle size is found at the intersection of the two curves [4].

2.3 Intermetallics

Intermetallic phases and compounds result from the combination of two or more different metals. With respect to a large number of possible combinations, a tremendously manifold quantity of intermetallics exists. In general, their existence and the solubility are caused by the characteristics of their free enthalpy. Figure 2.10 shows the relative positions of free enthalpy curves and the resulting phases.

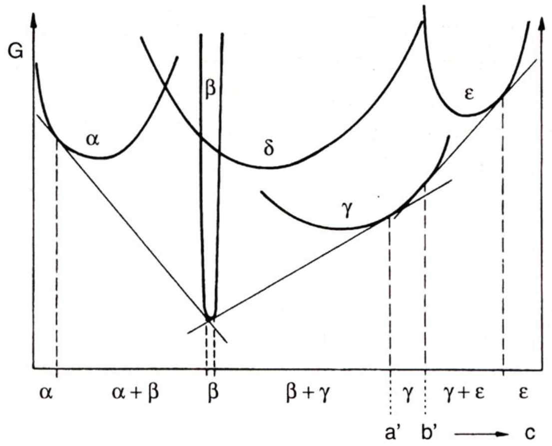

Figure 2.10: The diagram shows that the existence and solubility of the intermetallic phases are dependent on the relative positions of the free enthalpy curves. At this temperature the phases α, β, γ and ε occur [4].

Crystal structure, thermal and mechanical properties of intermetallic phases differ from that of pure metals and depend on the kind of bonding, which can be a mixture of different types, and the ratio of the atomic radii. A partially non-stoichiometric composition, a limited range of existence in the phase diagram as well as the new crystal structure and properties are special features of these phases. Traditionally, intermetallic phases and compounds have been grouped with respect to related characteristics according to various criteria [10].

Ordered phases

Three different types of interatomic bonds are present in the structure of a binary solid solution consisting of atoms A and B: A-A, B-B and A-B bonds. Each type has a certain negative energy (H_{AA}, H_{BB}, H_{AB}). As a characteristic energetic value of ordering H_0 is given as

$$H_0 = H_{AB}-(H_{AA}+H_{BB})/2. \tag{2-8}$$

In the case of a negative H_0, which means that H_{AB} is more negative than $(H_{AA}+H_{BB})/2$, and therefore A atoms prefer neighbouring B Atoms and vice versa, the atoms in the solid solution are not randomly distributed [4]. For the special case of compositions of types e.g. AB or A_3B the atoms become periodically arranged. Figure 2.11 shows the most common ordered crystal structures.

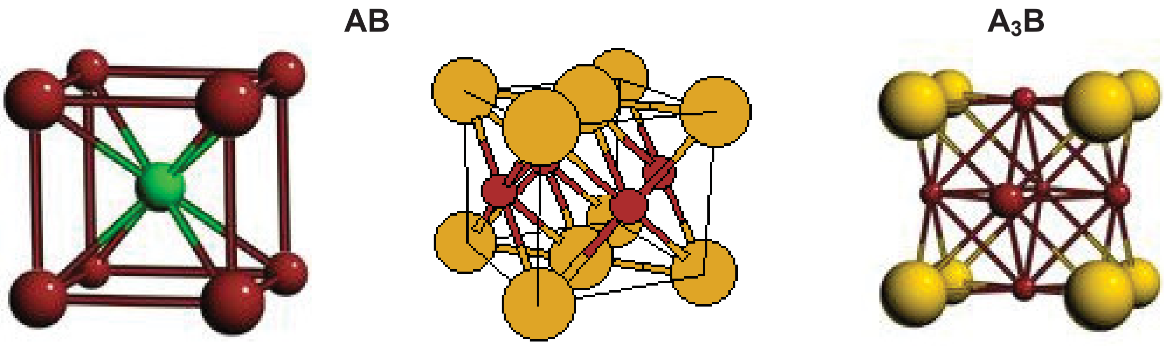

CsCl (B2)
e.g. NiAl, FeAl, CuZn

CuAu ($L1_0$)
TiAl

Cu_3Au ($L1_2$)
Ni_3Al

Figure 2.11: The most common and important ordered AB and A_3B crystal structures with examples [11].

The two cubic primitive sub lattices of the ordered B2 structure are arranged in a way that the edge atoms of the one lattice occupy the body centred sites of the other lattice. This formation guarantees that all atoms are surrounded by unlike atoms. The characteristic arrangement of the atoms of the Cu_3Au structure is achieved by occupying the face centred sites with the Cu atoms and the edge sites with the Au atoms, respectively. The $L1_0$ structure loses its cubic shape due to layer forming and different atomic radii. Four face centred sites of the AB type CuAu structure are occupied with Cu atoms like it is shown in Figure 2.11 [4].

The degree of ordering can be quantified by two parameters, SRO (short range order) and LRO (long range order). LRO parameter s is quoted as

$$s = (p-x)/(1-x), \qquad (2\text{-}9)$$

where p stands for the fraction of A-atoms on the A-lattice and x is the fraction of A-atoms in the alloy. In the case of a body centred cubic structure and a composition type AB, parameter s can be simplified to

$$s = 2p-1. \qquad (2\text{-}10)$$

As seen in equation 2-9 s is in a range between -1 and 1, whereas 1 and -1 mean perfect order and value 0 represents a random distribution of the atoms. The LRO parameter becomes absurd if the solid solution consists of domains which are bordered by so called anti-phase boundaries. An example of such an anti-phase boundary can be seen in Figure 2.12.

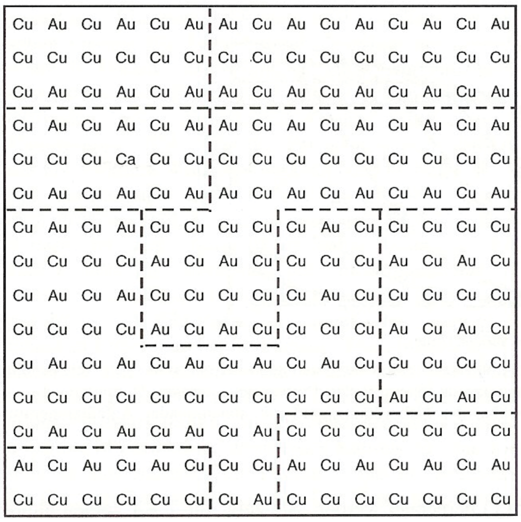

Cu	Au	Cu	Au	Cu	Au	Au	Cu	Au	Cu	Au	Cu	Au	Cu	Au
Cu	Cu	Cu	Cu	Cu	Cu	Cu	Cu	Cu	Cu	Cu	Cu	Cu	Cu	Cu
Cu	Au	Cu	Au	Cu	Au	Au	Cu	Au	Cu	Au	Cu	Au	Cu	Au
Cu	Au	Cu	Au	Cu	Au	Au	Cu	Au	Cu	Au	Cu	Au	Cu	Au
Cu	Cu	Cu	Ca	Cu	Cu	Cu	Cu	Cu	Cu	Cu	Cu	Cu	Cu	Cu
Cu	Au	Cu	Au	Cu	Au	Au	Cu	Au	Cu	Au	Cu	Au	Cu	Au
Cu	Au	Cu	Au	Cu	Cu	Cu	Cu	Cu	Au	Cu	Cu	Cu	Cu	Cu
Cu	Cu	Cu	Cu	Au	Cu	Au	Cu	Cu	Cu	Cu	Au	Cu	Au	Cu
Cu	Au	Cu	Au	Cu	Cu	Cu	Cu	Cu	Au	Cu	Cu	Cu	Cu	Cu
Cu	Cu	Cu	Cu	Au	Cu	Au	Cu	Cu	Cu	Cu	Au	Cu	Au	Cu
Cu	Au	Cu	Au	Cu	Au	Cu	Au	Cu	Au	Cu	Cu	Cu	Cu	Cu
Cu	Cu	Cu	Cu	Cu	Cu	Cu	Cu	Cu	Cu	Cu	Au	Cu	Au	Cu
Cu	Au	Cu	Au	Cu	Au	Cu	Au	Cu	Cu	Cu	Cu	Cu	Cu	Cu
Au	Cu	Au	Cu	Au	Cu	Cu	Cu	Au	Cu	Au	Cu	Au	Cu	Au
Cu	Cu	Cu	Cu	Cu	Cu	Cu	Au	Cu	Cu	Cu	Cu	Cu	Cu	Cu

Figure 2.12: A long range ordered A_3B crystal can be separated into domains which are long range ordered themselves by anti-phase boundaries [4].

These boundaries can be generated e.g. by a dislocation that runs through an ordered region by one burgers vector, or directly after nucleation and growth. The difference of two domains in a long range ordered crystal is that atoms A and B occupy different sub lattices, so that s changes between -1 and 1. Though the crystal is perfectly ordered, the mean LRO parameter becomes 0, due to the fact that the different domains occur with equal frequency [4].

The SRO parameter σ, which can vary between the values 0 and 1, has been defined to avoid these complications and can be quoted as

$$\sigma = (q-q_u)/(q_m-q_u), \qquad (2\text{-}11)$$

where q represents the fraction of B-atoms neighbouring A-atoms. Indices u and m stand for the random distributed state and for the perfectly ordered state, respectively [4].

Valence phases – Zintl phases

The Zintl phases are characterized by completely filled electronic orbitals, normally by a full octet shell, and satisfy the familiar chemical valency rules. Therefore, the range of existence in the phase diagram is extremely small. Thus, they can also be called line-phases. They are formed by metals and elements of the right side of the periodic table, especially of the groups IVA, VA and VIA. The dominating bonding type is heteropolar, fragments of especially the metallic and covalent types are also involved. The higher the difference in the electronegativity of the anion and the electropositivity of the cation the stronger is the stability of the phase. This can be seen in the value of the melting point. The Zintl phases crystallize in structures which are characteristic for typical salts, e.g. the NaCl, CaF_2 structures.

Size-factor phases

Close packing of the atoms becomes important in case of dominant metallic bond character. This is possible only if the composition and the ratio of atomic radii have adequate values. The size-factor compounds form the most numerous group of intermetallics and the best known representatives are the Laves phases. Very high packing densities are achieved for an atomic radii ratio of 1.225 (+/- 10%) and a composition of the type AB_2. The three possible crystal structures of the Laves phases are shown in Figure 2.13. Depending on the valence electron concentration of the compound either f.c.c. $MgCu_2$, hex. $MgNi_2$ or hex. $MgZn_2$ are incident. $MgCu_2$ achieves the highest packaging density of 71 %.

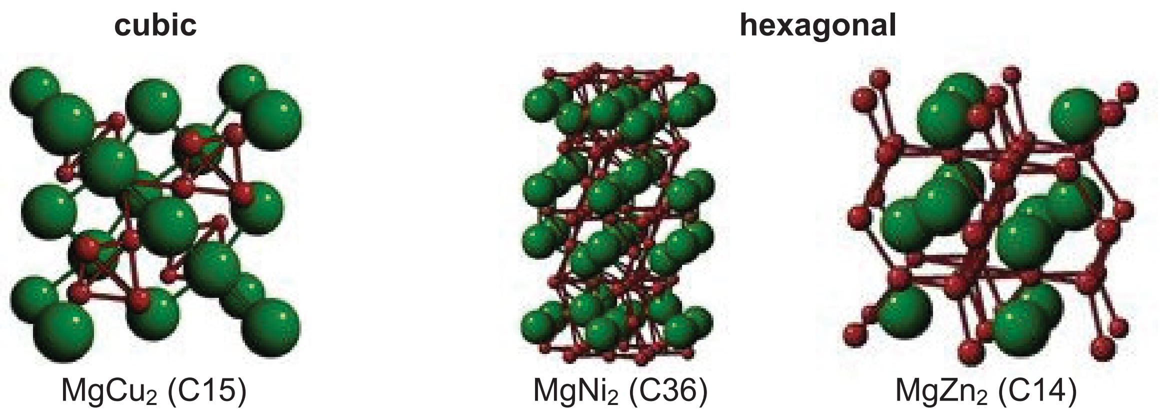

cubic **hexagonal**

$MgCu_2$ (C15) $MgNi_2$ (C36) $MgZn_2$ (C14)

Figure 2.13: The three different structures of Laves phases. Their incidence depends on the valence electron concentration [11].

A second kind of size-factor compounds are the Hägg phases, which are formed by filling the lattice vacancies of the metal with smaller-sized non-metal elements. This form of close packed phases can only be achieved by a ratio of atomic radii smaller than 0.59. A sharp solubility limit is a characteristic of these interstitial phases due to the fact that no more atoms can be solved after filling all capable vacancies. Hägg phases are generally of high stability, e.g. TaC has the highest melting point of all known solids with 3983°C.

Electron phases

Hume Rothery has correlated occurring intermetallic phases with the valence electron concentration (VEC):

$$VEC = c_A{*}NV_A + (1-c_A){*}NV_B\,, \qquad (2\text{-}12)$$

where c_A is the concentration of component A and NV_A and NV_B are the values of valence electrons of the components A and B, respectively. Assuming the convention that the alloying element is of higher valence, the same sequence of crystal structures occurs with increasing concentration in some binary alloys. The system Cu-Zn, shown in Figure 2.14, is a demonstrative example for visualizing such a sequence of intermetallic phases. Copper has a valency of 1 and zinc has a valency of 2, therefore, alloying copper with zinc increases the valence electron concentration of the compound. At a composition level of about 50% Zn a B2 ordered β_0 phase occurs, followed by a $D8_2$ ordered γ phase at a level of about 65% Zn and a A3 structured ε phase at a level of 80% [4].

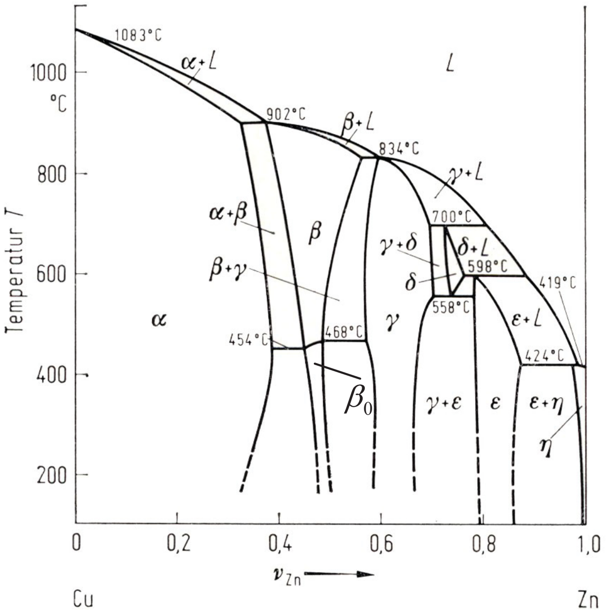

Figure 2.14: Phase diagram of the binary alloy Cu-Zn. With increasing fraction of Zn phases with different crystal structures become stable: β (B2) $\rightarrow \gamma$ ($D8_2$) $\rightarrow$ ε (A3) [4]

For certain values of the VEC corresponding crystal structures have been observed in different binary alloys: The cubic B2 structure for a VEC = 3/2, e.g. CuZn, Cu_3Al, NiAl; the complex cubic $D8_2$ structure for VEC = 21/13, e.g. Cu_5Zn_8, Fe_5Zn_{21}, Cu_9Al_4; and the hexagonal A3 structure for VEC = 7/4, e.g. $CuZn_3$, $AgCd_3$, and Ag_5Al_3 [10].

The stability and instability of different phases at special values of the valence electron concentration can be explained by Fermi statistics and the energy-band model. Alloying causes an increase in free valence electrons, which have to occupy remaining states of high energy. At a critical VEC or composition level it is energetically favourable to change the lattice structure offering more energy states to lower energy conditions.

The Hume Rothery phases principally have a metal bond character with ionic fragments [10] and the B2 structured NiAl phase traditionally is added to this group. On the basis of recent ab initio calculations NiAl is expected not to be a Hume Rothery electron compound [12]. It has also been found that the B2 structured NiAl phase has no ionic bond character. The bonding type is principally covalent with fragments of the metallic type [13].

2.4 System Fe-Ni-Al

2.4.1 NiAl

Figure 2.15 represents the binary Al-Ni phase diagram and a schematic of the B2 structured NiAl intermetallic compound.

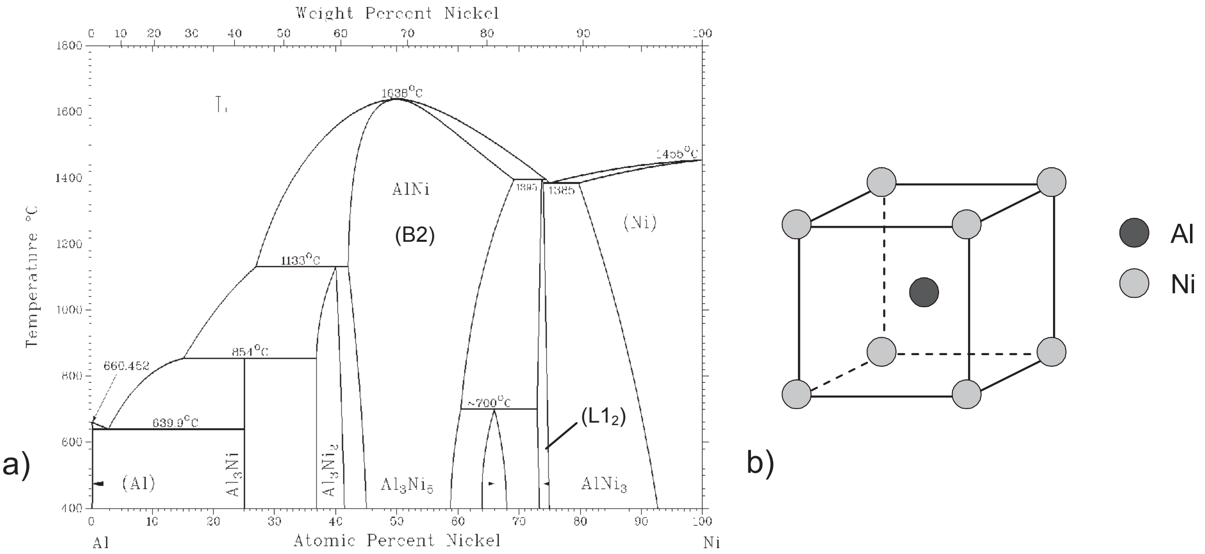

Figure 2.15: Binary Al-Ni phase diagram [4] (a), schematic illustration of the ordered B2 structured NiAl intermetallic compound (b).

As it is shown in the phase diagram the intermetallic phase NiAl has an extended range of existence with a congruent melting point of about 1640°C for the stoichiometric composition of 50 at% Al and Ni, respectively. The melting point is higher than those of the constituent elements which indicates that a strong bonding between Al and Ni atoms exists. This is associated with a high phase stability and a strong tendency to atomic ordering [10]. Figure 2.15(b) illustrates schematically the arrangement of the constituent elements of a B2 ordered crystal. The edge sites of the cubic cell are occupied with Ni atoms, whereas the Al atoms sit on the body centred positions. The structure can be brought to mind by a combination of a Ni and an Al primitive cubic sub lattice which are arranged in a way that the edge atoms of the one sub lattice occupy the body centred sites of the other sub lattice. Stoichiometric NiAl keeps its order even up to the melting point, whereas deviations of the stoichiometric composition cause constitutional point defects [10]. The physical and mechanical properties of the B2 structured NiAl intermetallic compound have been reviewed in a detailed way by Miracle [14]. The properties examined include electronic structure and bonding, crystal structure and phase stability, thermodynamic properties, elastic, electrical, magnetic and thermal properties, fracture toughness, cyclic and creep properties. Additionally, defects in NiAl and diffusion data are discussed.

2.4.2 Ternary system

In the middle of the 20th century Bradley [15, 16] has carried out microscopical studies and X-ray powder diffraction measurements on the Fe-Ni-Al system in order to generate a satisfactory equilibrium diagram. The main purpose was to characterize the miscibility gap between the body centred and the face centred cubic phase. Due to the fact that the knowledge of the phase diagram has been restricted to low aluminium contents (Al<50 wt %) the system Fe-Ni-Al was further discussed. The system has been reviewed in detail by Rivlin and Raynor [17] in 1980, Budberg and Prince [18] have updated the state of knowledge of the system in the early nineties.

Eleno et al. [19] have carried out the most recent critical assessment of the Fe-Ni-Al phase diagram. Raghavan [20-22] has given an overview of the latest work on the ternary Fe-Ni-Al system by providing isothermal sections at different temperatures and different compositions. Chumak et al. [23, 24] investigated the aluminium-rich corner as well as the region with lower aluminium contents. Several isothermal sections of the ternary system and phase compositions have been generated by means of a combination of powder X-ray diffraction, differential thermal analysis and electron probe micro analysis.

Though a large number of experiments and investigations on the system have been performed, the information on phase equilibrium is still not complete.

In Figure 2.16 an isothermal section at a temperature of 1200°C of the Fe-Ni-Al ternary system is presented. The ThermoCalc calculations show that two phases can occur in the iron rich corner at this temperature, the body centred α and the face centred cubic β phase. As it can be seen in the phase diagram, increasing Al content stabilizes the bcc phase, whereas addition of Ni makes the fcc phase stable.

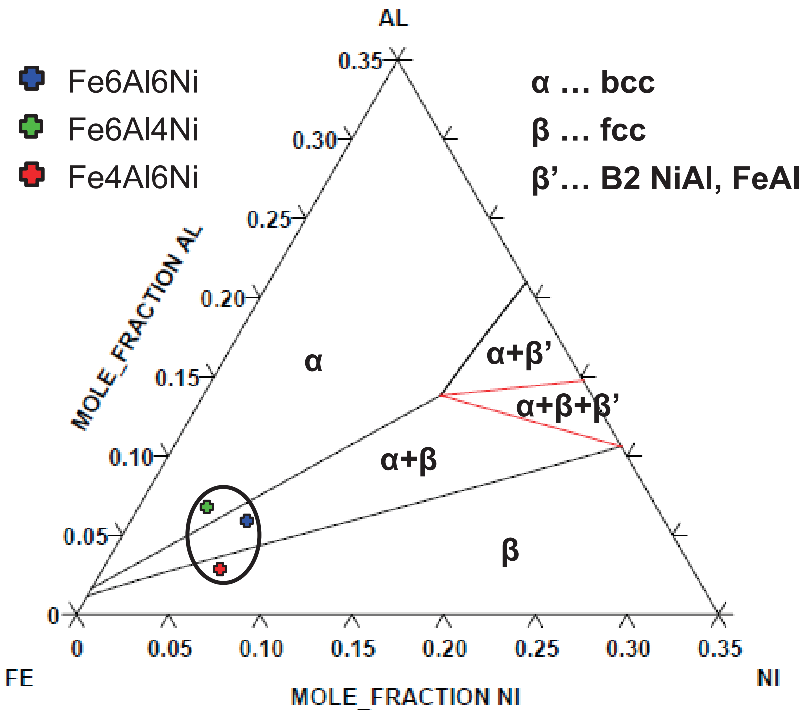

Figure 2.16: Ternary phase diagram of the Fe-Ni-Al system in the iron rich corner at a temperature of 1200°C. Calculated with ThermoCalc, Database: Kaufman Binary Alloys TDB v1. The marked area shows the alloys investigated in this thesis.

The black encircled region in the ternary system represents the approximate composition range of the alloys used in the present work. At the denoted temperature this area obviously spans three different phase regions, which are important for interpreting microstructure after solution heat treatment and quenching (see chapter 3.2.1).

2.5 NiAl precipitation strengthened steels

Fe based alloys with additions of Ni and Al are of great interest because of their wide range of applications and therefore many experimental investigations have been performed on these alloys.

A special status of interest is given to ferritic Fe-Ni-Al alloys due to their great potential associated with high-temperature applications. NiAl precipitates are embedded in a ferritic matrix to generate a tough material with good high-temperature properties. An overview of properties and application possibilities of NiAl in the form of precipitate as well as Ni and Al as base elements in metal alloys is given by Sauthoff [10]. A lot of work has been carried out on ferritic alloys, in the majority of cases measurements were performed on model alloys, due to the fact that in simpler systems it is easier to identify and characterize precipitation reactions as it is in technical materials.

Blavette et al. [25] have conducted atom probe measurements on a Fe-20Cr-2Ni-2Al at% alloy with the intention to observe the composition evolution of the precipitates. Therefore, the homogenized alloy has been isothermally aged at 550°C for three different times, 6, 17 and 117 h. They have found the intermetallic phase precipitates to reach a nearly stoichiometric composition NiAl with only a limited amount of dissolved iron atoms, which decreases with aging time.

A Fe-19 wt% Cr alloy containing stoichiometric additions of nickel and aluminium has been studied from the view point of precipitation kinetics and coarsening of the B2 ordered NiAl particles by Taillard et al. [26]. The nucleation is apparently homogenous and the coherent particles are randomly distributed in the matrix. During growth they first lose their initially spherical shape and adopt a cuboidal form followed by a loss in coherency which leads the particles to adopt a roughly spherical shape again. The loss of spherical shape occurs at a particle size of about 45 nm, the following cuboidal shape is preserved up to a size of about 150 to 300 nm, until the particles lose coherency. Based on the Johnson-Mehl law an exponent n=1 and an apparent activation energy of 80 kJ/mol has been calculated for the precipitation reaction. These values of exponent n and activation energy lead to the assumption that the precipitation is not controlled by a classical nucleation and growth process [26].

Precipitation of NiAl intermetallic compounds becomes very important in case of so-called maraging steels. These martensitic low carbon steels achieve high tensile strength and hardness due to the precipitation of finely distributed intermetallic compounds. Additionally, a satisfactory fracture toughness, which is caused by the soft matrix containing martensite and austenite, makes the maraging steels attractive for specific applications which require materials with ultrahigh strength, reasonable ductility and good fabricability [27].

Seetharaman et al. [1] have carried out optical microscopy, TEM and X-ray diffraction measurements on a PH 13-8 Mo stainless steel with the purpose to observe precipitation hardening. They have identified fine uniformly distributed spherical NiAl precipitates to be responsible for an increase in hardness and toughness. This increase is partially due to coherency strains, the state of order within the precipitates and the difference between the shear moduli of the matrix and the precipitates. The particles have been found to be highly resistant to overaging and even in the coarsening stage they remain fully coherent with the matrix, due to a very low lattice mismatch. With a simple geometrical criterion for coherency it has been predicted that the particles loose coherency at a mean radius of about 150 nm, which agrees with measurements of Taillard [26].

On a similar maraging steel Robino et al. [28] have performed an analysis of the hardening kinetics using the Avrami formalism. The results show low values for time exponent n and activation energy of the NiAl precipitation. These low values have been explained by nucleation along or near dislocations and subsequent growth aided by dislocation pipe diffusion.

Guo et al. [29] have also investigated a PH 13-8 stainless steel with respect to microstructural evolution during ageing. Because of the high resolution of the atom probe they have been able to observe characteristics like size, shape and distribution in the early stages of precipitation. Ni and Al enriched clusters have been found but the composition of these clusters is far from that of the stoichiometric NiAl phase. The amount of Ni and Al increases with respect to higher aging temperatures and longer aging times. In the early stages the NiAl precipitates have been found to be spherical but with proceeding aging they become platelike followed by a needle shape. After aging for 40 min at a temperature of 510°C the diameter of the spherical particles is about 1-2 nm. It has been observed that a coarsening stage has already started though the particles have not reached equilibrium composition. Similar experiments with agreeing results have been performed by Ping et al. [30].

Cloué et al. [31] have studied the influence of Al content on the mechanical properties of a PH 13-8 steel at different aging temperatures. Al content on the one hand affects the NiAl precipitation reaction and on the other hand the transformation temperature in the phase diagram, which is important for the formation of reverted austenite. The amount of precipitates is also related to the Al content [31].

Knowledge on the precipitation behaviour of the intermetallic NiAl phase has been achieved in association with investigations on several Ni and Al alloyed martensitic tool steels. These steels achieve their mechanical properties from combined precipitation of secondary hardening carbides and intermetallic phases. Garrison et al. [32] have studied the influence of separate and combined Al and Ni additions on the properties of a secondary hardening steel. They identified the B2 ordered NiAl phase to be responsible for an increase in hardness and toughness.

Erlach et al. [33] have studied the precipitation behaviour of a similar model alloy with the nominal composition Fe-0.32C-6.5Ni-2.5Al wt% after isothermal aging at 610°C for times up to 10000 min. The B2 ordered spherical NiAl precipitates were found to be homogenously distributed in the materials’ volume and to show coherency after aging for 10000 min. The average particle size found for the mentioned aging parameters was 35 nm. Atom probe measurements showed a particle diameter of 2 nm after 30 min of aging and 5-6 nm after 1000 min of aging. Number density decreases with aging time as well as the iron content of the precipitates. They approach a nearly stoichiometric NiAl composition with small fractions of iron [33].

Subsequently, the same model alloy has been investigated with respect to both the composition and morphology of the fine precipitates and the matrix present after short time aging at 610°C [34]. After aging for 60 sec the precipitates` size is about 1.5 nm and their composition shows a Ni to Al ratio of approximately 1, but additionally a remarkable amount of Fe and carbide forming elements. Ni and Al contents in the clusters and their radius increase as expected with aging time. The number density begins to decrease after 30 sec of aging, suggesting that these precipitates have already reached a coarsening stage. The simultaneous shift of composition towards the equilibrium stoichiometric NiAl composition indicates that the precipitation reaction is not controlled by a standard nucleation and growth process [34, 35] in accordance to [26].

To complement the previous investigations Erlach et al. [36] have tried to explain the aging kinetics of (Ni,Fe)Al by applying phase transformation theories. Hardness measurements have been analyzed by applying a modified Avrami formalism. A low value (59.9 kJ/mol) for the apparent activation energy of the precipitation reaction indicates that the formation of the intermetallic NiAl particles is controlled by nucleation along or in the vicinity of dislocations.

Hamano [37] has identified precipitates responsible for secondary hardening in a Fe-0.14C-5.07Ni-1.94Al wt% steel as M_2C alloy carbides and B2 NiAl intermetallic compounds. It has been shown that the highest plane strain fracture toughness values are achieved when the material contains coherent as well as incoherent precipitates.

Calderon et al. [38] have investigated the coarsening behaviour and the morphology of B2 ordered NiAl particles in Fe-Ni-Al-Mo ferritic alloys. It has been observed that the coarsening rate of the particles increases with increasing precipitate volume fraction and that the lattice parameter of the precipitated phase is a function of aging time. A change in the initially spherical shape of the NiAl particles has also been found, during coarsening they become cubic or even rectangular parallelepipeds. Additionally, coarsening kinetics of coherent B2 ordered NiAl precipitates in a Fe-10 at% Ni-15 at% Al have been investigated by Calderon et al. [39]. An alloy with a similar composition has been studied by Cayetano-Castro et al. [40] with the main focus on coarsening kinetics. The coarsening is controlled by diffusion and follows the Lifshitz-Slyozov-Wagner law. The development of the precipitates’ shape agrees with the results of the previous papers and additionally an orientation relation between precipitates and matrix has been found.

The correlation of precipitated NiAl particles with mechanical properties has been studied in several papers. Investigations on creep behaviour have been carried out on NiAl hardened austenitic steels [41] and on ferritic Fe-Al-Ni-Cr alloys [42].

According to precipitation kinetics of NiAl previous papers generally agree with respect to low values for activation energies and exponent n [26, 28, 36].

Summarily, many experimental investigations have been performed on the precipitation behaviour of Fe-Ni-Al based alloys. The results of the previous papers agree among each other with respect to size, shape and partially to composition development of the NiAl particles, but the precipitation mechanism in the early stages is not completely cleared yet.

3 Experimental

Three Fe-based model alloys with varying Ni and Al contents have been produced. Samples with suitable dimensions have been cut out from the cast ingots and solution heat treatment and aging have been conducted accordingly. After grinding and polishing microscopical studies and X-ray diffraction measurements on the as-quenched samples have been carried out. Hardness measurements on the as-quenched as well as on all aged samples lead to characteristic hardness-time curves, which allow for a determination of the beginning of precipitation and coarsening. Atom probe (3DAP) and small-angle neutron scattering (SANS) measurements have been conducted on selected samples to obtain information on precipitate development. Differential scanning calorimetry (DSC) completes experimental work by providing information on precipitation kinetics.

3.1 Alloying

For the present work three different alloys of the nominal compositions Fe-6Al-4Ni at%, Fe-6Al-6Ni at% and Fe-4Al-6Ni at% have been produced. In the following the alloys will be written as, e.g. Fe6Al4Ni. The pure starting metals have been balanced and melted in a furnace under argon atmosphere. After casting the 10 kg ingots have been water cooled. The compositions of the three alloys measured by emission spectral analysis (Spectromaxx by Spectro analytical instruments) and 3DAP are shown in Table 3-1.

Table 3-1. Composition of the three investigated model alloys measured by emission spectral analysis (ESA) and 3DAP for the solution annealed state.

		3DAP		**ESA**	
alloy	element	at%	wt%	at%	wt%
Fe6Al4Ni	Fe	89.26	92.50	89.40	92.33
	Al	6.60	3.30	6.55	3.27
	Ni	3.90	4.25	4.05	4.40
Fe6Al6Ni	Fe	88.40	90.70	87.69	90.12
	Al	5.32	2.64	5.86	2.91
	Ni	6.15	6.64	6.45	6.97
Fe4Al6Ni	Fe	90.73	92.00	90.71	91.90
	Al	2.92	1.43	3.11	1.52
	Ni	6.16	6.57	6.18	6.58

3.2 Heat treatment

3.2.1 Solution annealing

Specimens with a dimension of 10 x 10 x 20 mm^3 have been cut from the cast ingots and have been solution annealed in a Carbolite RHF 16/15 furnace at a temperature of 1200 °C for 5 h. The high temperature guarantees that the alloying elements are solved in the iron matrix after acceptable times. Stable phases at the mentioned conditions are shown in an isothermal section of the ternary phase diagram in Figure 2.16. Subsequent water quenching generates a supersaturated solid solution. Due to the small specimen dimensions the cooling rate is high enough to prevent an unmeant precipitation reaction also in the inner regions of the samples.

3.2.2 Aging

The specimens have been aged at a temperature of 500°C for times up to 96 h in a Carbolite HRF/45 circulating air oven followed by water quenching.

Aging for times below 10 min has been carried out in a type 805A/D dilatometer of the Bähr Thermoanalyse GmbH, which enables high heating and cooling rates. Specimens heat treated in the dilatometer have been solution treated in the furnace, turned to the required diameter of 5 mm, cut to a length of 15 mm and finally aged in the dilatometer. Thus, reactions in the material during heating and cooling, which can influence the results, have been avoided.

3.3 Microscopy and X-ray diffraction of the solution annealed samples

The light microscopic photographs of the as-quenched samples represented in Figure 3.1 show that the microstructure significantly differs between the three model alloys. Fe6Al6Ni has a classical ferritic structure whereas the grains of the Fe4Al6Ni alloy are somehow fringed. The grain size of the Fe6Al4Ni sample is a multiple higher than that of the others. In order to control the assumption of a ferritic structure in case of the three model alloys X-ray measurements have been conducted. Figure 3.2(a) represents the X-ray diffraction patterns of all solution annealed samples. The measured peaks depicted in Figure 3.2(a) belong to α–iron and no other peaks are present at all. As seen in Figure 3.2(b) the measured peaks are shifted to smaller angles with respect to the peak positions of pure α–iron. The lattice constant increase is 0.5% in case of Fe6Al6Ni and Fe6Al4Ni, and 0.4% in case of Fe4Al6Ni.

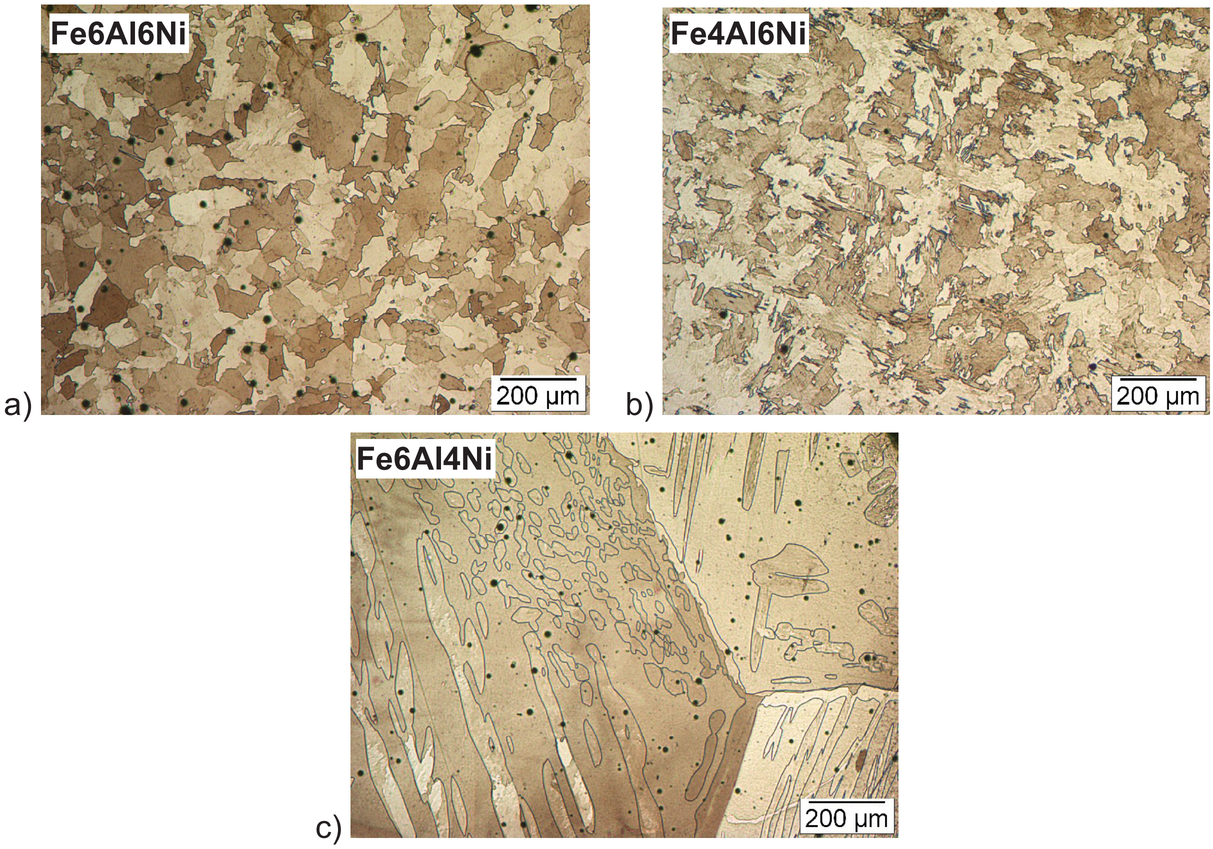

Figure 3.1: Light microscopic photographs of the as-quenched samples a) Fe6Al6Ni, b) Fe4Al6Ni, c) Fe6Al4Ni.

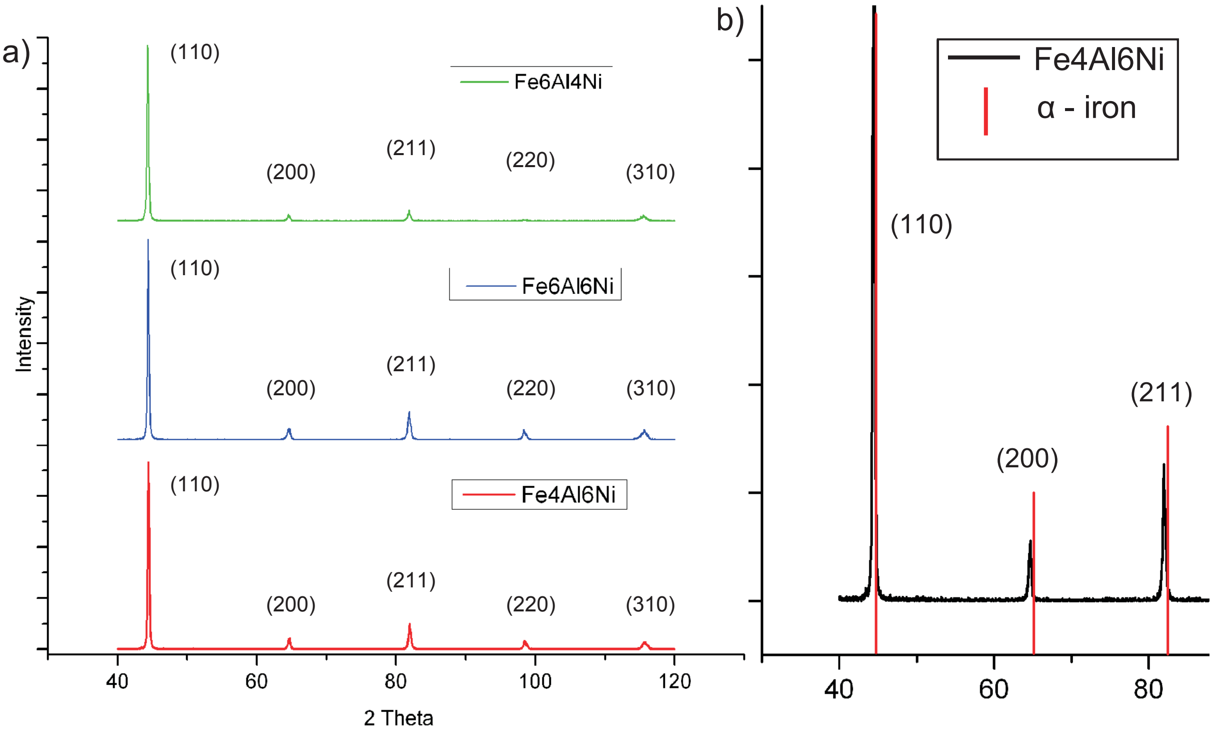

Figure 3.2: X-ray diffraction patterns of the solution annealed states (a); Detail of the Fe4Al6Ni diffraction pattern with the peak positions of pure α–iron (b).

3.4 Hardness measurements

For all aging states hardness measurements have been conducted with an EMCO-TEST type M4C instrument, using the Vickers method with a weight of 5 kg for a time of 15 sec. Each of the presented hardness values is the average of four independent measurements. Cylindrical dilatometer samples have been measured on the planar side and cuboidal shaped samples have been measured on a plane parallel and 3 mm away from the head side.

3.5 SANS

3.5.1 Principle

Attested by the wave-particle dualism a neutron has a wavelength, which allows implementing diffraction experiments with a neutron beam. The neutron interacts strongly on the one hand with atomic nuclei and on the other hand with magnetic moments in the solid due to its magnetic dipole moment. These two interactions lead to scattering e.g. by measuring a crystalline solid with lattice constants in the range of the neutrons' wavelength [43]. Basics of the scattering technique can be found in [44].

Measurements in the present work have been carried out on the beam line SANS-2 at the Geesthacht Neutron Facility (GeNF). As seen in Figure 3.3(a) the incoming neutron beam has to pass a velocity selector providing a monochromatic beam followed by a polarizer and a spin-flipper. The collimation depends on the detector distance to obtain scattering vectors q ($q = 4\pi\sin(\Theta)/\lambda$, where 2Θ is the scattering angle and λ is the wave) in the expected range.

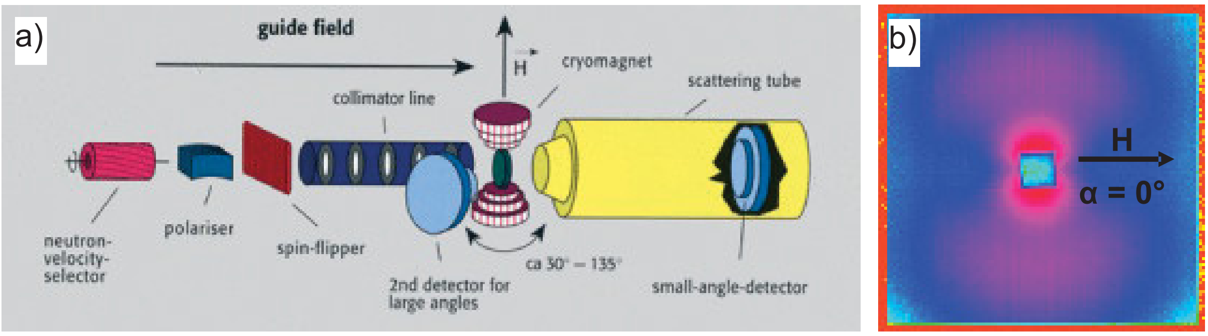

Figure 3.3: Schematic overview of the beam line SANS-2 at the Geesthacht Neutron Facility (GeNF) [45] (a); Example of a scattering image caught by the detector. H = magnetic field, α = angle between scattering vector and magnetic field (b).

After passing the collimators the beam reaches the sample environment consisting of an electro-magnet and the sample itself. Transmitting the magnetized sample is the last step before reaching the detector, giving a characteristic scattering image (Figure 3.3(b).

3.5.2 Sample preparation

For the small-angle neutron measurements disc shaped specimen with a thickness of 2 mm and a diameter of 22 mm have been produced (Figure 3.4).

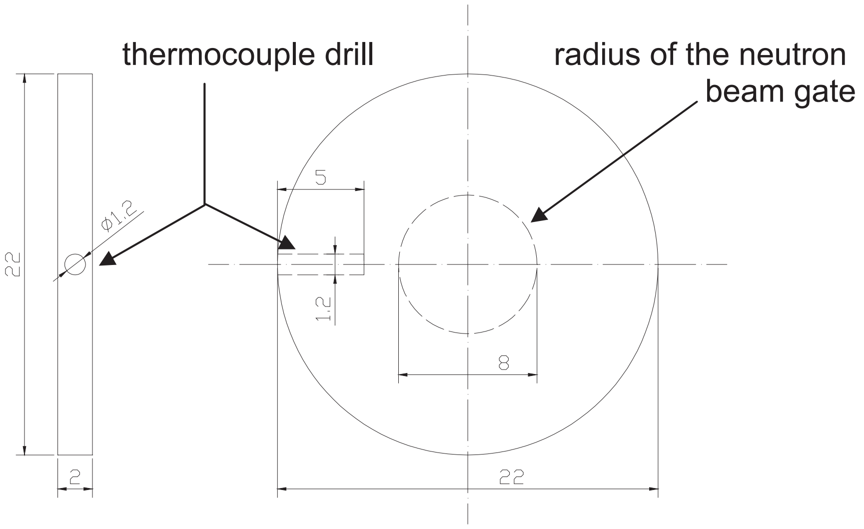

Figure 3.4: Geometry and characteristic dimensions of the specimen used for the small-angle neutron measurements of in-situ and static (without thermocouple drill) experiments. (Dimensions in mm)

Additionally, in case of in-situ experiments a hole on the front side of the sample has been drilled to position a thermocouple providing an accurate temperature regulation. Static samples have been heat treated before measuring whereas the in-situ samples have been measured from the initial solution treated state. The implementation of the different measuring methods will be described in 3.5.4.

3.5.3 Test setup

The sample holder (Figure 3.5(a)) which is at the same time the furnace for the in-situ experiments consists of a ceramic base and two metal plates which can be bolted together, thus, clamping the sample. The specimens’ centre is positioned into the centre of the round opening of the metal plates in a way, which positions the thermocouple drill hole like it is shown in Figure 3.5(a). For in-situ measurements the resistance heated metal plates transfer the heat to the sample by conduction. Figure 3.5(b) shows the sample table surrounded by the magnet, the instrumentation of the incoming beam and the detector pipe. After positioning the sample holder on the sample table and installing the thermocouple, a water cooled vacuum chamber is put over the sample apparatus.

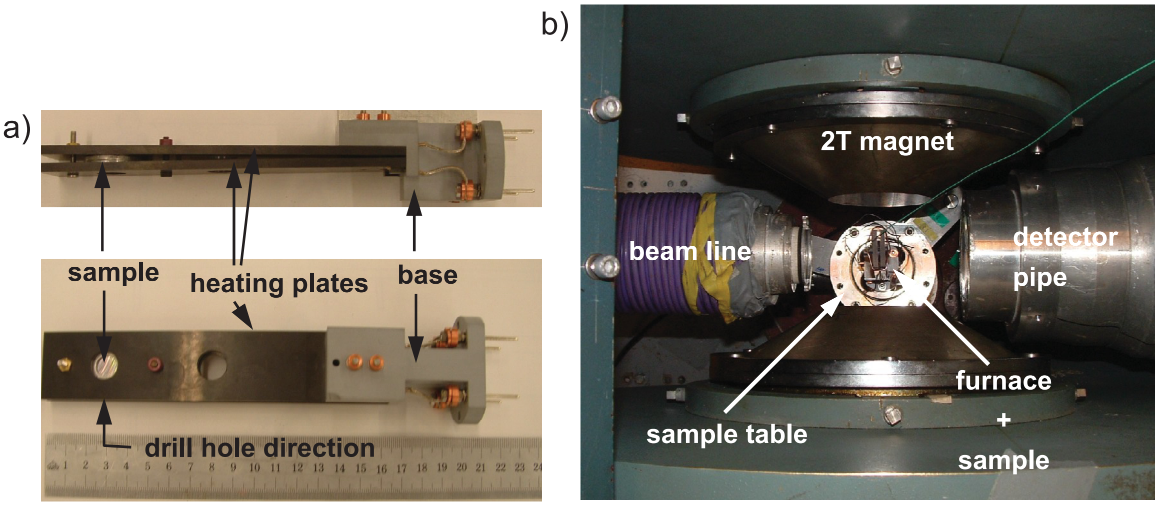

Figure 3.5: Furnace with a clamped sample (a); Top view of the sample environment (b).

3.5.4 Implementation

In Table 3-2 all conducted measurements are listed. Samples of all three model alloys have been solution annealed and aged for 5, 10 min and for 3, 24 h. After positioning the furnace with the clamped sample and fixing the vacuum chamber, the chamber has been evacuated to a vacuum of 5 x 10^{-2} mbar and then the chamber has been filled with helium, providing a small scattering background. The samples aged for 24 h have been measured statically, without activating the furnace, for 20 min at detector distances of 1 and 3 m, 25 min at 9 m and 30 min at 21 m. All other samples have been measured for 20 min at a detector distance of 1 meter. Before starting in-situ measurements a temperature calibration was necessary because of a temperature gradient towards the sample centre due to the missing heating plate contact (Figure 3.5(a)). For a singular calibration measurement two thermocouples have been installed, one in the centre of the dummy sample and one in the 5 mm deep drill hole. Knowing the temperature difference of the two thermocouples allowed for adapting the temperature regulation so that the sample volume in the beam line had an average of the expected temperature. In case of the in-situ experiments continuous as well as isothermal measurements have been carried out on the three model alloys. In case of the continuous experiments the solution treated samples have been heated up to 700°C with heating rates of 15, 23 and 36 °C/min. Intervals of recording a detector image contain an exposure time of 30 sec and additional 4 seconds according to saving processes, hence, all 34 seconds a data file is generated. In-situ samples for the isothermal experiments have been heated up with a heating rate of approximately 10°C/sec to the required aging temperature, exposing to the beam for 30 sec for the first hour of the experiment, 60 sec for the next four hours and 120 sec for the rest of the measurement time, providing reasonable statistics. Saving processes increase according measuring intervals as well.

Table 3-2: List of all sample states and according measuring conditions.

	Statically	In-situ	
	Aged at 500°C	**Isothermally [°C]**	**Continuously [°C/min]**
Fe6Al4Ni	5 min, 10 min, 3 h, 24 h	500	15, 23, 36
Fe6Al6Ni	5 min, 10 min, 3 h, 24 h	500, 600	15, 23, 36
Fe4Al6Ni	5 min, 10 min, 3 h, 24 h	500	15, 23, 36

Unpolarized neutrons with a mean wavelength of $\lambda = 0.57$ nm and a wavelength spread of $\Delta\lambda/\lambda = 10$ % have been used. The sample material has been magnetized to saturation by a 2 T magnetic field perpendicular to the beam. As depicted in Figure 3.4 the neutron beam impinging on the samples had a diameter of 8 mm. Corrections have been made for sample transmission, background intensity and detector efficiency to gain the accurate quality. Quantification of scattering cross sections has been obtained by calibration with a vanadium standard.

3.5.5 Evaluation

The measured scattering cross sections have been analyzed by means of the so-called two-phase model, according to [44],

$$\frac{d\Sigma}{d\Omega}(q) = (\Delta\eta)^2 \int_0^\infty n(R) V(R)^2 F(q,R)^2 \, dR \,. \tag{3-1}$$

In this equation $\frac{d\Sigma}{d\Omega}(q)$ is the macroscopic scattering cross section dependent on the scattering vector q, $\Delta\eta$ represents the scattering length density difference between matrix and precipitates, n(R)dR and V(R) are the number density and the volume of the precipitates and F(q, R) is a form factor. According to previous investigations the precipitates have been assumed to be of spherical shape in the early stages, which leads, according to [46], to a form factor of

$$F(q,R) = 3\frac{\sin(qR) - qR\cos(qR)}{(qR)^3} \,. \tag{3-2}$$

In case of a magnetic material the overall scattering contrast consists of a nuclear contribution $\Delta\eta_{nuc}$ and an additional magnetic contribution $\Delta\eta_{mag}$. According to the two-phase model, the homogeneity of a matrix which is magnetized to saturation is disturbed by particles, which represent magnetic inhomogeneities. The neutron beam is scattered due to the magnetic scattering contrast $\Delta\eta_{mag}$ between matrix and precipitates, which can be calculated theoretically (see 3.5.6). The magnetic scattering cross section depends on the angle α between the scattering vector and the magnetic field. When the chemical size of the precipitates is assumed to be the same as their magnetic size, Δη is defined by [47]:

$$(\Delta\eta)^2 = \Delta\eta_{nuc}{}^2 + \Delta\eta_{mag}{}^2 \sin^2(\alpha) \,. \tag{3-3}$$

Therefore, according to equation 3-3 and Figure 3.3(b), the nuclear scattering cross section has been measured at angles of α = 0° and α = 180°, the nuclear and superposed magnetic scattering cross section at α = 90° and α = 270°. Sectors with an opening angle of 20° have been used to average measured scattering cross sections, providing better statistics. The magnetic contribution can be obtained by subtracting nuclear cross section (sectors parallel to magnetic field) from the sum of nuclear and magnetic cross section (sectors perpendicular to magnetic field). Knowledge of magnetic scattering cross section, a chosen form factor and a calculated $\Delta\eta_{mag}$ allows calculating the particle size distribution by fitting appropriate scattering curves using the indirect method described by Glatter [48, 49]. Total number density n and total volume fraction f can be calculated by

$$n = \int_{R_{\min}}^{R_{\max}} n(R)\,dR \,, \tag{3-4}$$

$$f = \int_{R_{\min}}^{R_{\max}} n(R)V(R)\,dR \,, \tag{3-5}$$

respectively [50], where R_{max} and R_{min} are boundary conditions of the indirect method. Figure 3.6 shows a section of the evaluation software consisting of a fitted scattering curve and the according particle size distribution.

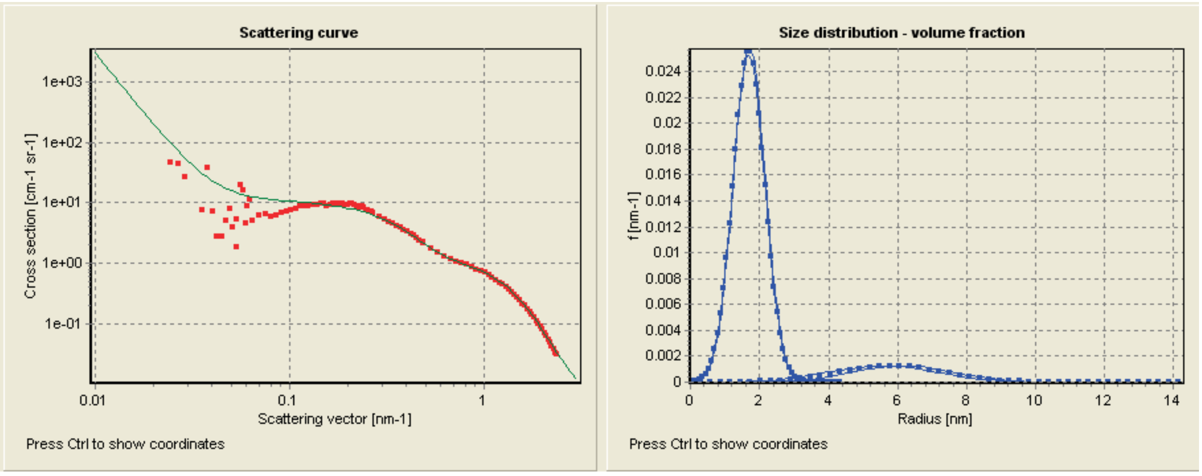

Figure 3.6: Fitting of the scattering curve of the Fe4Al6Ni sample aged for 24 h with the appropriate software (left); Associated particle size distribution (right).

3.5.6 Determination of the magnetic scattering length density difference (SLDD)

The calculation of the difference of the magnetic scattering length densities of the matrix $\eta_{mag,m}$ and precipitates $\eta_{mag,p}$ is necessary to obtain information on radii, number density and volume fraction from the scattering curves. Equation 3-6 represents the calculation of the magnetic scattering length density difference (SLDD) $\Delta\eta_{mag}$:

$$\Delta\eta_{mag} = \eta_{mag,m} - \eta_{mag,p} = \left(\frac{p}{V}\right)_m - \left(\frac{p}{V}\right)_p = \left(\frac{p_0 \cdot \mu_m}{V_m}\right) - \left(\frac{p_0 \cdot \mu_p}{V_p}\right) \tag{3-6}$$

where p is the magnetic scattering length, $p_0 = 2.70 \times 10^{-13}$ cm/μ_B is a constant [47], μ represents the magnetic moment and V is the mean atomic volume. Therefore, the mean magnetic moments $\mu_{m,p}$ per atom for matrix and precipitate, respectively, have been calculated from the Fe, Ni, Al moments according to the compositions determined by 3DAP. The values of the mean atomic volume were determined by 3DAP data as well. If the precipitates are assumed to be non-magnetic, $\Delta\eta_{mag}$ relates to $\eta_{mag,m}$. Therefore, it is possible to obtain information on the volume fraction and number density of the precipitates without knowing their composition. The SLDD changes with aging time due to the development of the compositions. Magnetic SLDD's for all aging states have been calculated for magnetic as well as for non-magnetic particles.

3.5.7 Determination of the nuclear scattering length density difference (SLDD)

A useful possibility for qualitatively observing the composition development of precipitated particles is the calculation of the so called R-value. Therefore, the nuclear scattering length density difference (SLDD) between matrix and precipitates has to be determined additionally to the magnetic SLDD. Equation 3-7 shows the calculation of the nuclear SLDD $\Delta\eta_{nuc}$:

$$\Delta\eta_{nuc} = \eta_{nuc,m} - \eta_{nuc,p} = \left(\frac{b_m}{V_m}\right) - \left(\frac{b_p}{V_p}\right) \tag{3-7}$$

The nuclear scattering length densities of the matrix $\eta_{nuc,m}$ and of the precipitates $\eta_{nuc,p}$ are obtained by dividing the atomic nuclear scattering lengths b_m and b_p by the mean atomic volumes V_m and V_p, respectively. The mean nuclear scattering lengths per atom of the matrix and precipitates have been calculated from the Fe, Al and Ni atomic scattering lengths according to the compositions obtained by 3DAP data. Correlating the measured compositions with the elemental atomic volumes leads to the mean atomic volumes.

3.5.8 R-Value

The ratio of the magnetic to the nuclear scattering intensity depends on the chemical compositions of the precipitates and of the matrix assuming that the matrix is magnetized to saturation and that the precipitates have the same magnetic size as their chemical size. Evaluating the measured scattering curves concerning the ratio of the sum of magnetic and nuclear to the nuclear scattering cross section leads to the A value

$$A(q) = \frac{\frac{d\Sigma}{d\Omega}\left(q, \frac{\pi}{2}\right)}{\frac{d\Sigma}{d\Omega}\left(q, 0\right)}. \tag{3-8}$$

If the precipitates of all occurring sizes have the same composition the q-dependence of A disappears, hence, A becomes a constant. Inserting equations 3-1 and 3-3 in equation 3-8 makes A only dependent on the nuclear and magnetic scattering contrast:

$$A = 1 + \frac{\left(\Delta\eta_{mag}\right)^2}{\left(\Delta\eta_{nuc}\right)^2} = 1 + R\,. \tag{3-9}$$

The so called R-value is on the one hand theoretically calculated by using the compositions of the matrix and precipitates obtained by the 3DAP data and on the other hand by evaluating static as well as in-situ SANS experiments. Therefore, the ratio of the nuclear and magnetic integral intensity of the scattering cross sections is calculated. The scattering cross sections have to be summed up over the complete q-range which complies with the area under the scattering curve to obtain the according integral intensity Q:

$$Q = 4\pi \int_0^\infty \frac{d\Sigma}{d\Omega}(q) q^2 dq = (2\pi)^3 f(1-f)(\Delta\eta)^2 \tag{3-10}$$

Equations 3-9 and 3-10 show that the ratio of the magnetic and the nuclear integral intensity leads to the R-value.

3.6 3DAP measurements

3.6.1 Principle

Imaging at the atomic scale with the 3DAP is based on field evaporation. Therefore, a sample with a tip radius in the range of 20 to 100 nm has to be produced (see section 3.6.2). The electric field F_0 appearing on the apex can be calculated by equation 3-11:

$$F_0 = \frac{V_0}{k_f r_0}\,. \tag{3-11}$$

V_0 represents the applied voltage, k_f is a form factor which considers the geometric deviation of a spherical shaped apex and r_0 is the tip radius [2]. To realize the required electric fields a high voltage and a radius in the nm-range are necessary. Additionally, to reduce thermally induced oscillations of the atoms, the sample is cooled down to a temperature of 20 to 80 K. A vacuum of < 10^{-10} mbar completes the main parameters of the sample environment. The applied high voltage consists of a direct contribution V_{DC} which lies slightly under the evaporation level and a superposed pulsed high voltage V_{Pulse}. Some of these pulses cause evaporation of the atoms which are accelerated to the position sensitive detector. Additionally, the time of flight of the evaporated atoms is measured. Information on time of flight t, flight distance d, total applied voltage and elementary charge e leads to the mass to charge ratio m/n, as expressed in equation 3-12 [2].

$$\frac{m}{n} = \frac{2e\left(V_{DC} + V_{Pulse}\right)t^2}{d^2} . \qquad (3\text{-}12)$$

Each element can be identified by its mass to charge ratio. Converting detector data and corresponding mass to charge ratios and implementing several corrections with convenient software lead to a three-dimensional image of the evaporated sample volume.

For the experiments in the present work a 3DAP^{TM} – X Oxford Nanoscience has been used. An energy compensation system provides a reasonable mass resolution. The 3DAP measurements have been carried out at a sample temperature of 80 K, vacuum of < 3 x 10^{-11} mbar and an applied direct voltage between 3.5 kV and 15 kV with a pulse fraction of 15 %.

3.6.2 Sample preparation

Samples with a dimension of 0.3 x 0.3 x 15 mm^3 have been sharpened by using a two-step electrochemical treatment. As seen in Figure 3.7(a) for step I the sample, which is the cathode, is dipped into an electrolyte (25% perchloric acid (70%) in glacial acetic acid), which is layered on an inert fluid (Galden).

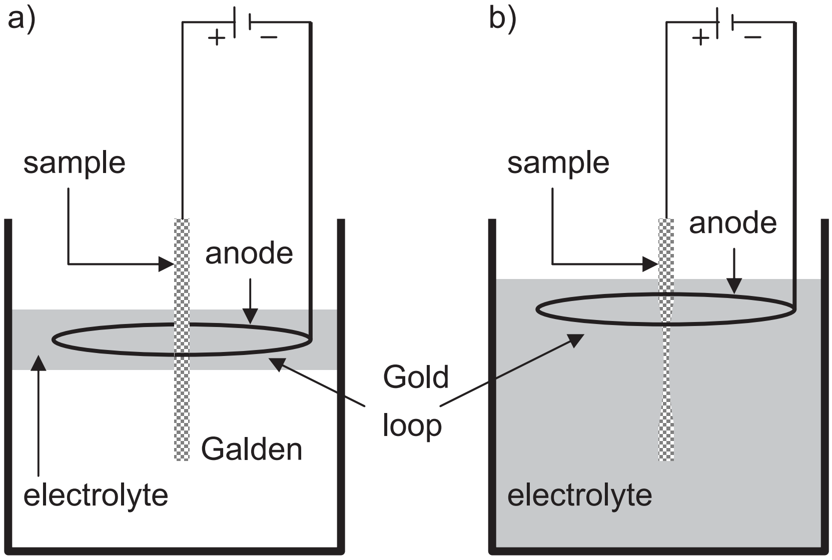

Figure 3.7: Schematic view of the 3DAP sample preparation aperture. Step I (a); Step II (b).

The gold loop in the electrolyte represents the anode. The highest etching effect occurs at the electrolyte-air interface. Therefore, while applying a voltage of approximately 15 volts, the sample has to be moved up and down to achieve a neck like geometry as it is seen in Figure 3.7(b). Step II uses a weaker electrolyte (2% perchloric acid in 2-butoxyethanol) and a voltage of approximately 10 volts is applied until the sample is etched into two pieces. The upper part is cleaned and installed into the 3DAP aperture [2].

3.6.3 Cluster algorithm

The distance between solute atoms in a solute enriched cluster or precipitate is assumed to be significantly smaller than that in the surrounding matrix. Therefore, clusters have been determined by the use of a method based on the maximum separation distance between solute atoms. The parameters d_{max} and N_{min} have to be defined which is difficult, furthermore, no universal approach exists. Parameter d_{max} represents the maximum separation distance between the according atoms and N_{min} is the minimum number of contained atoms to be defined as a cluster. Figure 3.8(a) shows the change in the number of defined clusters with variation of the two parameters. In Figure 3.8(b) the change in radius, number density and volume fraction with variation of d_{max} at a fixed N_{min} is represented. If the chosen value for d_{max} is too small the clustering algorithm can not find atoms which belong together and the number of determined clusters as well as the average radius decrease rapidly. A too high d_{max} risks coalescence of the clusters which leads to a decrease in number density and an increase in radius. Additionally, influencing radii and number density leads to a change in volume fraction. Decreasing N_{min} certainly causes an increase of number density and a decrease of radius, but N_{min} has to be high enough to exclude random fluctuations of the solute atoms.

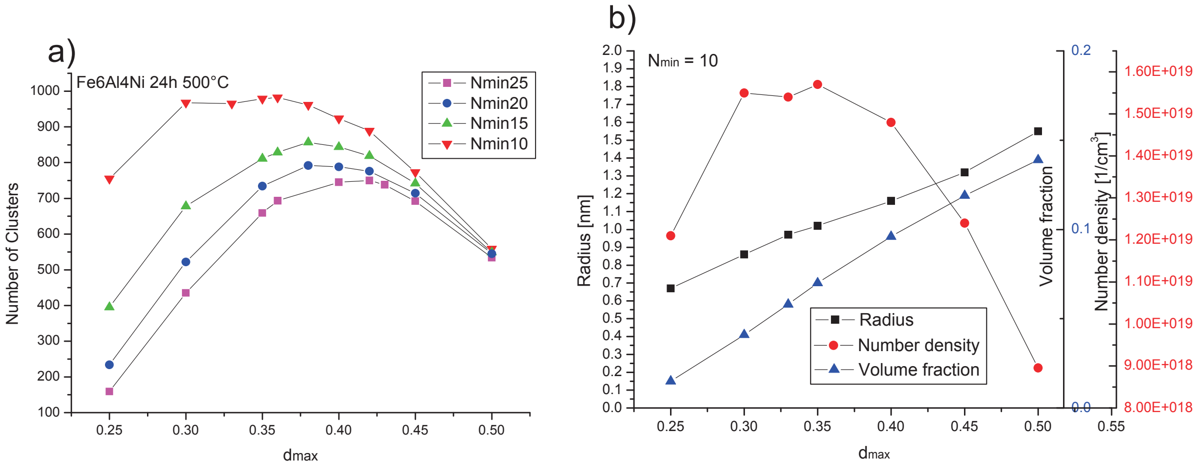

Figure 3.8: Dependence of the number of clusters with variation of parameters d_{max} and N_{min} (a); Dependence of precipitate characteristics with variation of d_{max} (b).

In the present work d_{max} has been determined based on Vamousse et al. [51]. As a demonstration of decreasing atomic distance with ongoing precipitation Figure 3.9 shows the distance distribution of solute Al atoms in the observed volume of the as-quenched sample and of the 24 h aged sample. The values on the abscissa represent the distances of an Al atom to its next nearest Al neighbour. This nearest neighbour distance is calculated for each Al atom and leads to the seen distribution.

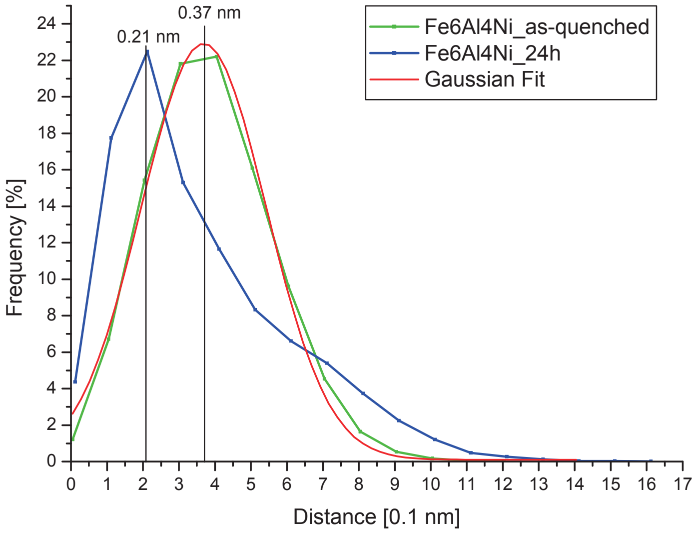

Figure 3.9: Distance distribution of Al atoms in the as-quenched and the 24 h aged state. The parameter d_{max} is determined close to the mean distance of the distribution of the as-quenched state.

The source for determining d_{max} is the combined distance distribution of Ni and Al from the as-quenched state which simulates a matrix with randomly distributed solute atoms. The idea is to determine the maximum separation distance d_{max} on the left side close to the mean distance of the Gaussian distribution of the as-quenched state. Hence, for N_{min} a value is chosen so that the cluster algorithm using this d_{max} only identifies an insignificant number of clusters for the as-quenched state. The used software allows calculating the distance distribution for one single element only. Determining combined mean distance of both elements has been carried out according to equation 3-13 which has been postulated in the present work. The value ρ_i x d_i^3 has been approximated to be a constant, where ρ_i is the atomic density and d_i represents the mean distance of the solute element according to its distance distribution assuming a uniform distribution. The solute atoms in the as-quenched samples have been proved to be uniformely distributed in the matrix (see section 4.3). Combined mean distance d_{Ni+Al} has been calculated by averaging the results for Ni and Al:

$$d_{Ni+Al} = \sqrt[3]{\frac{\left(\frac{\rho_{Al} \cdot d_{Al}^{\ 3} + \rho_{Ni} \cdot d_{Ni}^{\ 3}}{2}\right)}{\rho_{Ni+Al}}} \tag{3-13}$$

Table 3-3 shows the elemental densities $\rho_{Al,\ Ni}$ and the mean nearest neighbour distances $d_{Al,\ Ni}$ from the 3DAP data of the as-quenched state and the calculated values for Ni+Al.

Table 3-3: Determination of search parameter d_{max}, according to the as-quenched state

As-quenched	ρ_{Al} [nm^{-3}]	ρ_{Ni} [nm^{-3}]	d_{Al} [nm]	d_{Ni} [nm]	ρ_{Ni+Al} [nm^{-3}]	d_{Ni+Al} [nm]	$\mathbf{d_{max}}$ **[nm]**
Fe6Al4Ni	2.15	1.16	0.367	0.474	3.31	0.326	0.32
Fe6Al6Ni	1.59	1.67	0.408	0.402	3.26	0.321	0.32
Fe4Al6Ni	0.78	1.70	0.531	0.406	2.48	0.360	0.36

Differences in the atomic number density according to different atom probe datasets lead to the necessity of a density related adaptation of d_{max} [52]. Therefore, a density dependent d_{max} for the datasets of the aged states is calculated with this relation as well:

$$d_{\max} = \sqrt[3]{\frac{\rho_0 \cdot d_{\max,0}^3}{\rho}} \tag{3-14}$$

In this equation ρ_0 and ρ represent the atomic number densities of all atoms in the data set. Index 0 means the values of the reference, hence, the as-quenched state. Density variations within a single dataset have been disregarded.

Two additional parameters, surround- and erosion distance have been found to be suitable when they have the same value as d_{max}. After defining solute atoms which belong to a particle, all the atoms within the surround distance L are taken as being part of the same particle. This procedure leads to a shell of matrix atoms being included to the particle which can be removed by an erosion process (erosion distance E). Details can be found in [51].

3DAP measurements have been carried out on similarly heat treated samples as in the SANS experiments, providing the opportunity to compare the results. A complete list of investigated samples is given in Table 3-4.

Table 3-4: List of all 3DAP measurements of the three model alloys.

	Aged at 500°C
Fe6Al4Ni	As-quenched, 10 min, 3 h, 24 h
Fe6Al6Ni	As-quenched, 10 min, 3 h, 24 h
Fe4Al6Ni	As-quenched, 10 min, 3 h, 24 h

3.7 DSC

Differential scanning calorimetry (DSC) is an effective tool to observe precipitation kinetics. While isothermal aging is generally very time-consuming, experiments performed at constant heating rates are a rapid possibility to study transformation reactions. Transformed volume fractions according to a precipitation reaction can be correlated to the area under the peak of the heatflow-time curve according to the reaction [53]. Measuring at different heating rates enables to calculate activation energies by applying the Kissinger method. Borrego and González [54] have implemented a model to fit DSC curves based on the Avrami law. Minimizing the deviation of the fit allows calculating kinetic parameters.

In the present work differential scanning calorimetry is principally used to obtain information on the starting point and the activation energy of the NiAl precipitation reaction. The measurements have been carried out on a DSC instrument LABSYS EVO provided by the company SETARAM.

3.7.1 Principle

Figure 3.10 shows the used differential scanning calorimeter representing the DSC rod with two platinum crucibles and the furnace. The installed thermocouples at the crucible tray and a heat shield surrounding the rod are also depicted.

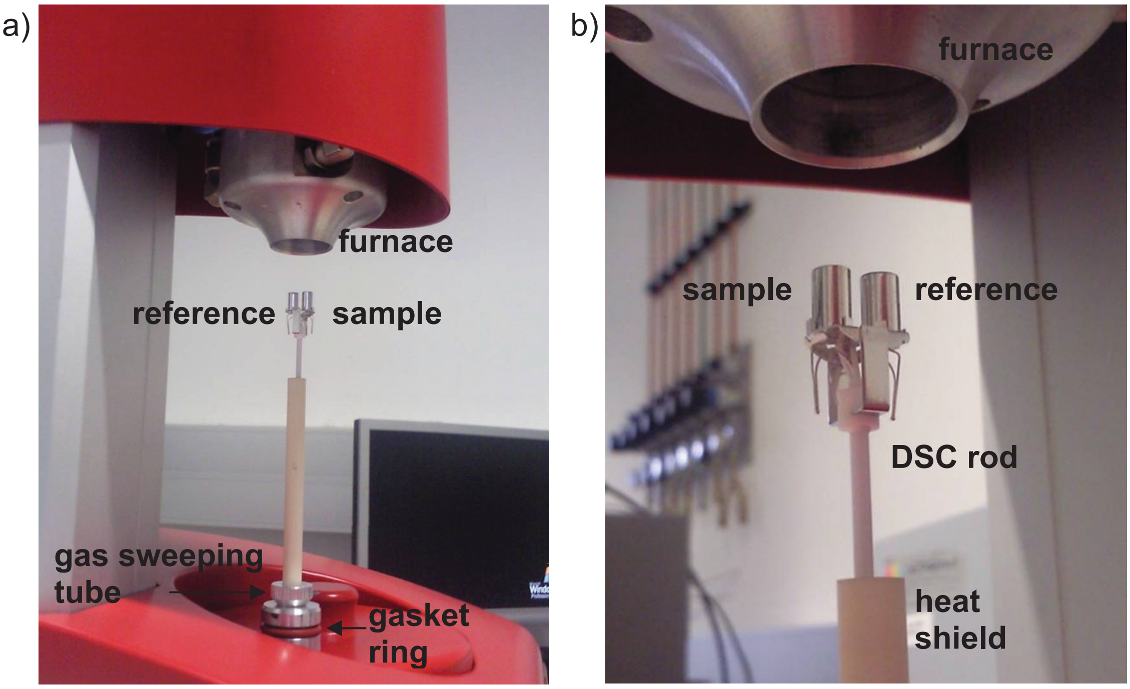

Figure 3.10: Differential scanning calorimeter Labsys Evo of the company SETARAM. Overall view of the aperture (a); Detailed image of the DSC holder tray rod and the crucibles (b).

The two crucibles containing the sample and the reference, respectively, are sited on the designated device on the top of the rod. The furnace is moved down until the gasket ring separates the DSC rod from the atmospheric environment. Subsequently, a vacuum of approximately 15 mbar is applied to the measuring chamber. Activating the sweeping gas leads to a gas circulation from the bottom to the top, entering by the sweeping tube and exiting at the top of the furnace. Afterwards the measurement with its appropriate temperature program is started. Different heat capacities between the sample and the reference and reactions in the sample during heating lead to a temperature difference between the two crucibles. The measuring signal is the temperature difference and the signal output by the DSC accessible to the user is the measured heat flow Φ_m in µV which is proportional to the temperature difference ΔT [55]:

$$\phi_m \sim \Delta T \tag{3-15}$$

3.7.2 Calibration

The electrical output signal Φ_m in µV is transformed into thermal energy Q in Joule by determining a calibration factor K, which significantly depends on several measurement conditions as temperature, crucible material, kind and flow rate of the sweeping gas. The sample form and weight influence K as well, therefore, samples with similar dimension and weight have been produced. Measuring pure metallic standards with a defined melting enthalpy under experimental conditions allows for determining the calibration factor K. Figure 3.11 shows schematically the characteristic peak of a melting reaction in the heat flow – temperature curve.

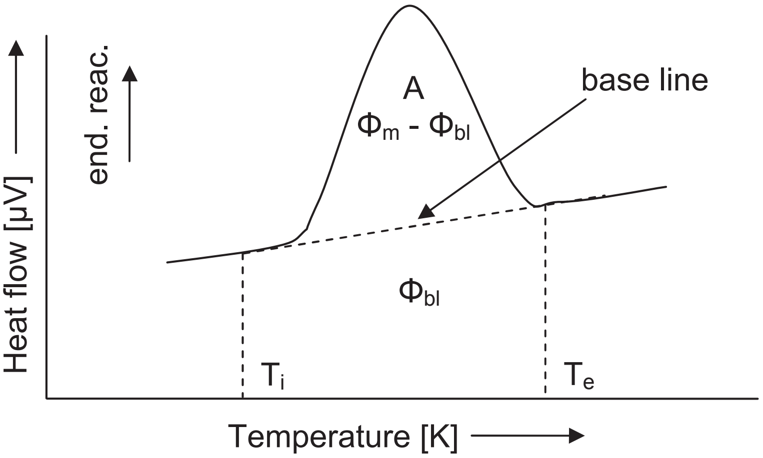

Figure 3.11: Schematic view of a characteristic peak according to an endothermic reaction. Determining the peak area A requires the subtraction of the area below the base line from the whole measured area between T_i and T_e.

A “zero measurement” using two empty crucibles which is subtracted from the proper curve is conducted to eliminate aperture asymmetries. Setting a base line and determining the initial and end temperatures T_i and T_e of the reaction allow for defining the peak area A. The experiments have been conducted with a constant heating rate β (in K/min). Hence, the temperature characteristic is given by

$$T = T_0 + \beta \cdot t \tag{3-16}$$

with T_0 representing the starting temperature and t representing time [55]. According to Figure 3.11 and equation 3-16 evaluating the heat flow rate – temperature curves leads to the peak area A (in µV s):

$$A = \frac{1}{\beta} \cdot \int_{T_i}^{T_e} (\phi_m - \phi_{bl}) dT\ . \tag{3-17}$$

$\Phi_{m,\ bl}$ represent the total measured heat flow rate and the according value under the base line.

With H being the melting enthalpy of the metallic standard (in mJ/g) and m being the weight (in g) the according calibration factor K is calculated by

$$K = \frac{A}{H \cdot m} \quad . \tag{3-18}$$

K is preferably expressed in µV/mW [56]. Implementing this procedure with standards at different melting points leads to the calibration factors K_i at different temperatures which are plotted as polynomial K-temperature curves by fitting with the software Calisto by Setaram. For any peak area A associated with a reaction the corresponding thermal energy Q (in mJ) equals:

$$Q = \frac{A}{K(T)} = \frac{1}{\beta} \cdot \int_{T_i}^{T_e} \frac{(\phi_m - \phi_{bl})}{K(T)} dT \quad . \tag{3-19}$$

At the same time the measurement of the metallic standards is used for a temperature calibration. Since the thermocouples offer the temperatures at the holder tray a temperature difference with respect to the sample exists. With the well known temperatures according to the melting points of the standard materials it is possible to realize a temperature correction. The used software considers this temperature differences and provides the true sample temperature.

3.7.3 Implementation

Samples with a dimension of 3 x 3 x 1 mm^3 and a mass of approximately 70 mg have been produced. Experiments with the heating rates of 6, 10, 15 and 23 K/min have been implemented for the Fe6Al4Ni model alloy. Each heating rate required the determination of the calibration coefficient K and its temperature dependence. On the reference side an empty platinum crucible has been used and argon has been chosen as inert gas.

The apparent activation energy of the transformation reaction can be determined by implementing the Kissinger analysis. The peak temperature T_p, heating rate β and the apparent activation energy E are related as described in equation 3-20

$$\ln\left(\frac{T_p^2}{\beta}\right) = \frac{E}{RT_p} + \ln\left(\frac{E}{RK_0}\right), \tag{3-20}$$

where K_0 is a pre-exponential factor and R represents the gas constant. Plotting $\ln\left(\frac{T_p^2}{\beta}\right)$ against $\frac{1}{T_p}$ allows for the determination of the apparent activation energy E and K_0. In order to determine the effective activation energy Q_{eff} the JMA exponent n has to be calculated. The relation of the exponent n, apparent activation energy E obtained by the Kissinger method and Q_{eff} is given by [54]

$$nE \approx \frac{3}{2} Q_{eff} \, . \tag{3-21}$$

According to Borrego et al. [54] the DSC peaks have been fitted by applying equation 3-22 to the heat flow vs. temperature curves:

$$\Phi = AnK_0^n \left(\frac{T^2 R}{\beta E} \right)^{n-1} \exp\left(-\frac{nE}{RT} \right) \exp\left\{ -\left[\left(\frac{T^2 R}{\beta E} \right)^n K_0^n \exp\left(-\frac{nE}{RT} \right) \right] \right\} . \tag{3-22}$$

The previous correlation (equation 3-22) between the heat flow Φ and the temperature is based on the Johnson Mehl Avrami theory. A computerized method optimizes the variables peak area A, exponent n and the pre-exponential factor K_0 by a minimization of least squares error.

Since the performed reruns of the measured samples provide no reasonable results linear base lines have been chosen to be used to define the transformation peaks as a first approximation in the present work. The curves have been modified to bring them into a form which allows for a reasonable fitting. After subtracting the according zero measurement and setting the linear base line the DSC curve has been arranged in a way that the base line becomes horizontal. Figure 3.12 depicts this procedure. Therefore, a slope correction has been implemented which leads to a rotation of the curve centring the starting point of the transformation reaction (Figure 3.12(a)). Exporting and analyzing the peak with the fitting software enables the transformation parameters (Figure 3.12(b)).

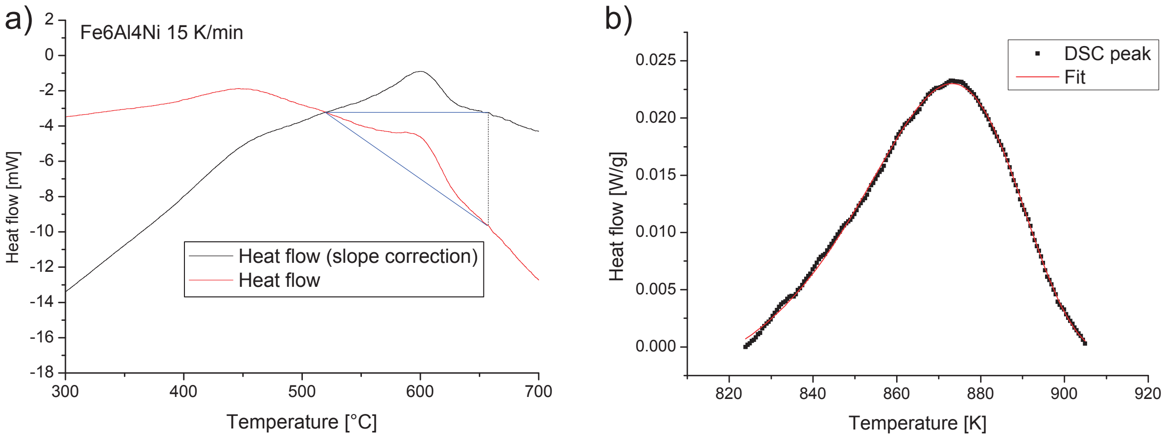

Figure 3.12: Measured heat flow of the Fe6Al4Ni sample at a heating rate of 15 K/min and the according slope correction (a); Exported transformation peak (b).

4 Results

4.1 Hardness

The change of hardness with respect to ongoing aging provides an illustration of the development of particles according to the NiAl precipitation reaction. Figure 4.1 shows the hardness vs. aging time of the three model alloys for aging at 500°C. The marked aging times depict the sample states which have been investigated furthermore by 3DAP and SANS. It can be seen that all three curves show similar characteristics and that the alloy Fe6Al6Ni generally shows higher hardness values with respect to the two other alloys. The data points at 1 sec represent the hardness values of the solution annealed samples.

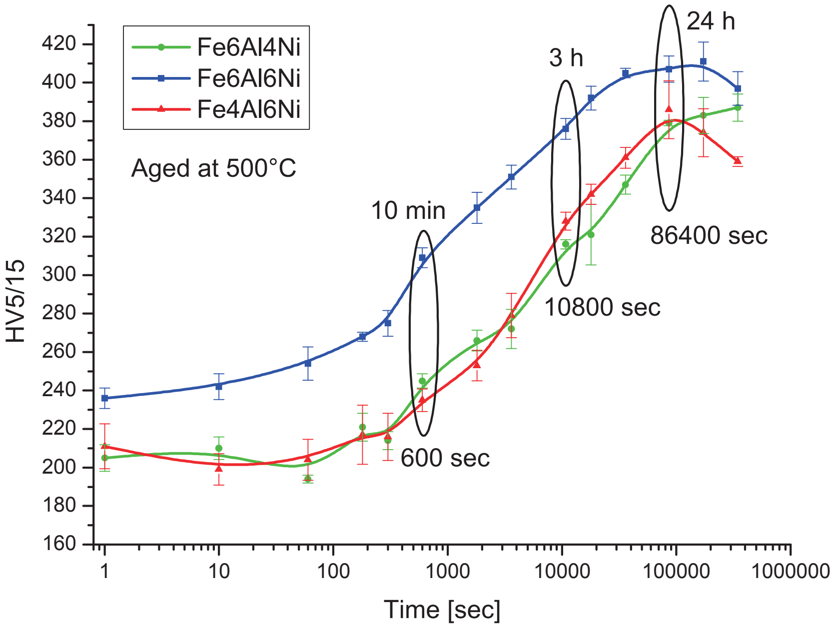

Figure 4.1: Dependence of hardness on aging time obtained for the three model alloys after aging at 500°C. The vertical bars represent the standard deviation of each hardness value.

Alloys Fe6Al4Ni and Fe4Al6Ni do not show significant changes in hardness up to 300 sec of aging. The hardness curves of both alloys are identical up to times of about 100000 sec. A constant increase of hardness with respect to the aging time occurs with similar slope for both alloys. The hardness of Fe4Al6Ni decreases after 24 h (86400 sec) of aging, whereas Fe6Al4Ni does not show any decrease up to times of 96 h (345600 sec). In case of the Fe6Al6Ni alloy the hardness increases continuously with a small slope after beginning of aging. After 300 sec of aging the hardness evolution is similar to the two other alloys. The peak hardness is reached at approximately 48 h (172800 sec) and afterwards a drop in hardness occurs.

4.2 DSC

In order to obtain information on the transformation kinetics and on the starting point of the NiAl precipitation reaction DSC measurements have been conducted. The extremely low heat of reaction makes it impossible to evaluate the NiAl precipitation reaction in case of the alloys Fe6Al6Ni and Fe4Al6Ni. Therefore, DSC measurements have only been performed on the Fe6Al4Ni model alloy. Figure 4.2 shows the heat flow over temperature curves of the Fe6Al4Ni alloy. Measuring the heat flow at different heating rates leads to a change of the maximum peak temperature T_p which represents the point of the maximum transformation rate of the according precipitation reaction.

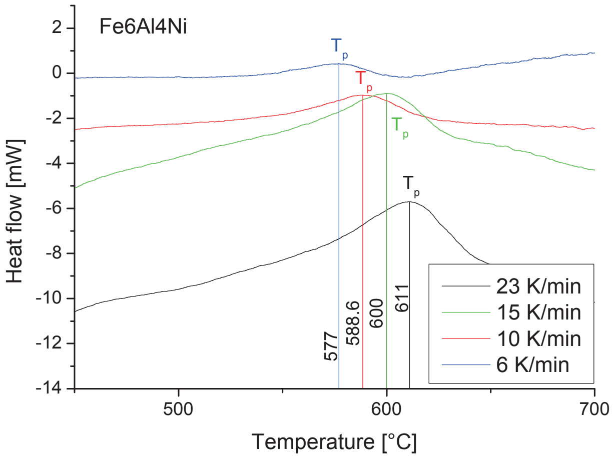

Figure 4.2: Development of the peak temperature T_p with increasing heating rate for the Fe6Al4Ni model alloy.

T_p shifts to higher temperatures with increasing heating rates. According to equation 3-20 (section 3.7.3) the Kissinger analysis has been performed. Figure 4.3 shows the Kissinger plot yielding the transformation parameters which are given in Table 4-1.

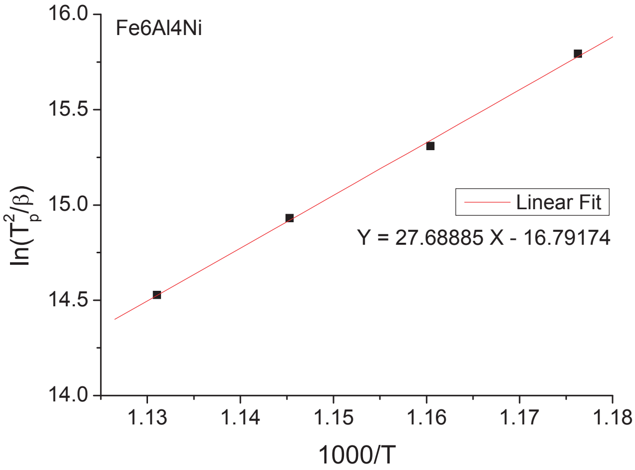

Figure 4.3: Kissinger plot of the exothermal DSC peak according to the NiAl precipitation reaction of the Fe6Al4Ni alloy.

Table 4-1: Results of the Kissinger analysis of the Fe6Al4Ni alloy.

	$\frac{E}{R \cdot 1000}$	$\ln\left(\frac{E}{RK_0}\right)$	E [kJ/mol]	K_0
Fe6Al4Ni	27.68885	-16.79174	230.218	5.430×10^{11}

Applying the Kissinger analysis yields the apparent activation energy E of 230 kJ/mol and a constant factor K_0 of 5.43×10^{11} for the NiAl precipitation reaction. The obtained apparent activation energy is used to fit the DSC curves as described in chapter 3.7.3. Figure 4.4 shows the DSC peaks of all heating rates and the fits.

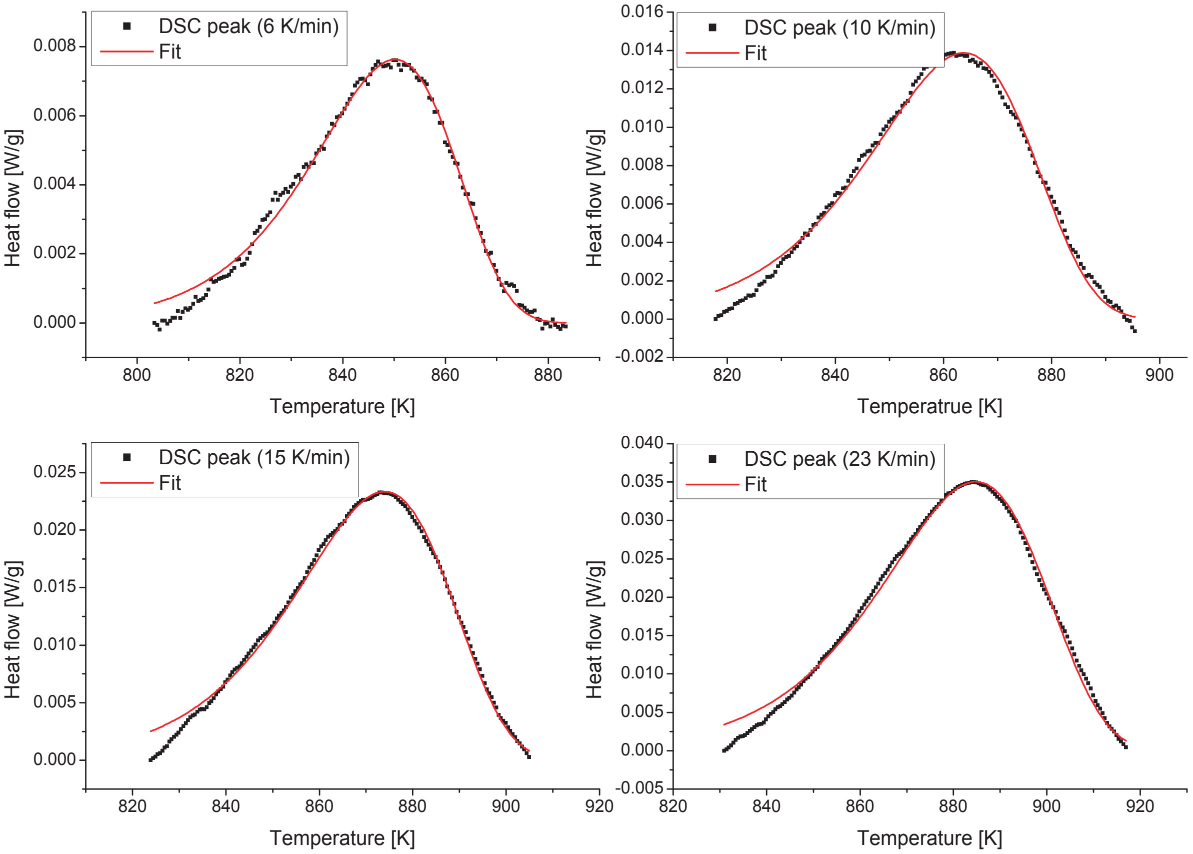

Figure 4.4: Measured transformation peaks according to the NiAl precipitation reaction in the Fe6Al4Ni alloy of the four heating rates. The red line belongs to the Avrami based fit.

The function applied to the measured DSC data satisfactorily fits the peaks caused by the NiAl precipitation reaction. Table 4-2 presents the results of fitting the DSC curves according to equation 3-22 (section 3.7.3). The effective activation energy Q_{eff} can be calculated according to equation 3-21 (section 3.7.3).

Table 4-2: Determined kinetic parameters according to the different heating rates.

β [K/min]	A [J/g]	n	K_0	Q_{eff} [kJ/mol]
6	2.73	1.8	5.03×10^{11}	276.262
10	3.53	1.74	5.00×10^{11}	267.053
15	4.38	1.61	5.09×10^{11}	247.101
23	4.48	1.58	5.20×10^{11}	242.496

Averaging the results of the four heating rates leads to a mean exponent n of 1.68 and a mean effective activation energy Q_{eff} of 258 kJ/mol. Additionally, the evaluated peaks can be observed with respect to the onset of the precipitation reaction. For the purpose of clearness Figure 4.5 shows the dependence of the start temperature of the heating rate by comparing the peaks.

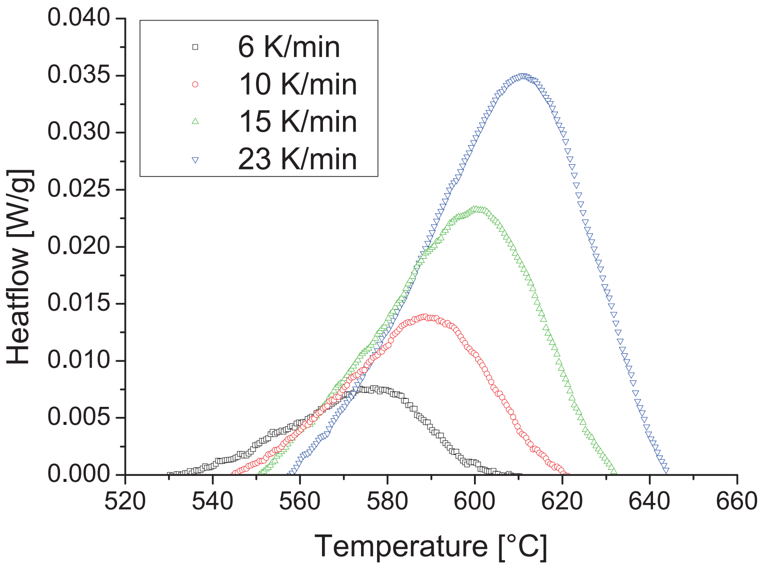

Figure 4.5: Dependence of the start temperature of the NiAl precipitation reaction in Fe6Al4Ni of heating rate.

The DSC measurements offer an onset temperature of 530°C at heating rate 6 K/min, 545°C at 10 K/min, 551°C at 15 K/min and 558°C at 23 K/min.

4.3 3DAP

Before investigating the aged samples with respect to particle development the as-quenched samples have to be proved to their homogeneity. Figure 4.6 shows the nearest neighbour distance distributions for Al and Ni of the three model alloys.

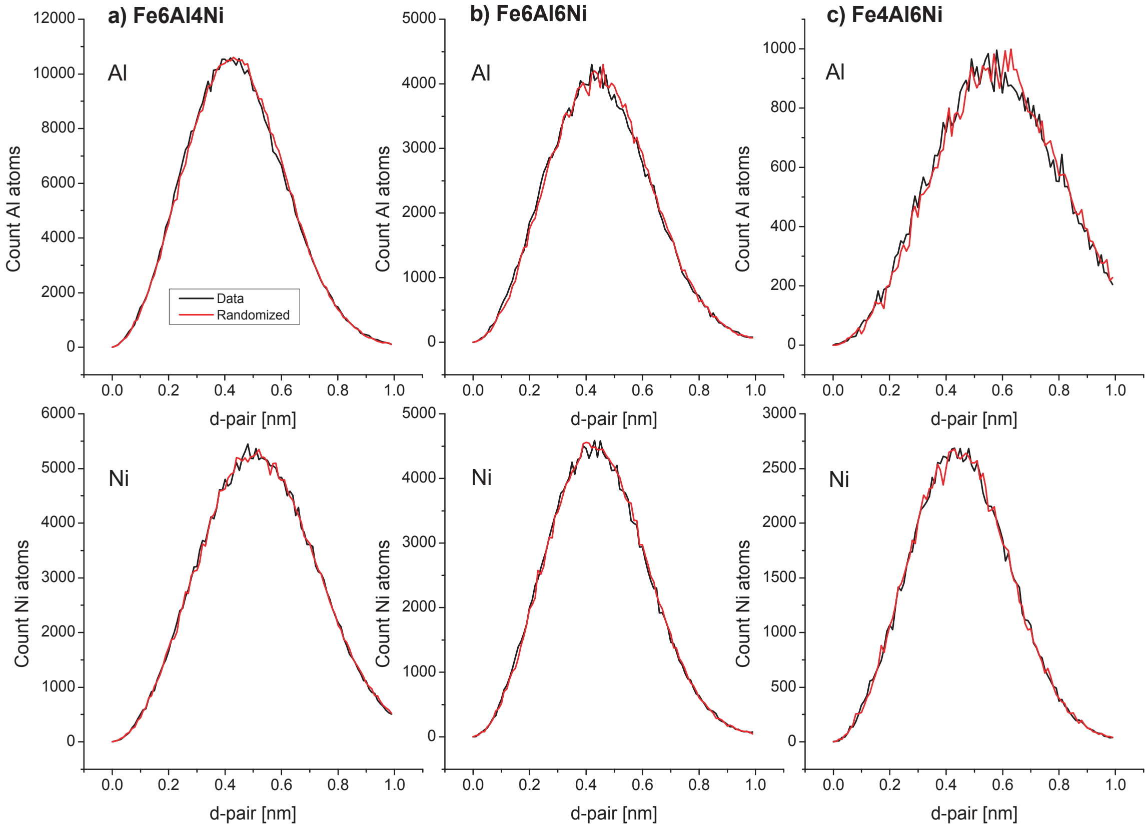

Figure 4.6: Nearest neighbour distance distributions of solute Al and Ni atoms in the solution annealed samples of a) Fe6Al4Ni, b) Fe6Al6Ni, c) Fe4Al6Ni.

The next nearest neighbour distance distribution of Al atoms in the as-quenched Fe6Al4Ni sample (Figure 4.6(a)) shows that the mean distance between the Al atoms and their next nearest Al neighbour is 0.5 nm. The diagrams contain to different curves. The black curve describes the distribution of solute atoms according to the 3DAP reconstruction and the red curve depicts the randomized distribution of solute atoms in the observed volume. The two curves are identical regarding the solute Al as well as the solute Ni atoms in case of all three model alloys.

The samples for the 3DAP measurements have been aged for 10 min, 3 h and 24 h at 500°C for all three model alloys as depicted in Figure 4.1. Figure 4.8 to Figure 4.15 show extracts of the 3DAP reconstructions of all investigated samples, including a visualization of the clusters detected by the applied search algorithm. Additionally, Al and Ni atoms are depicted separately.

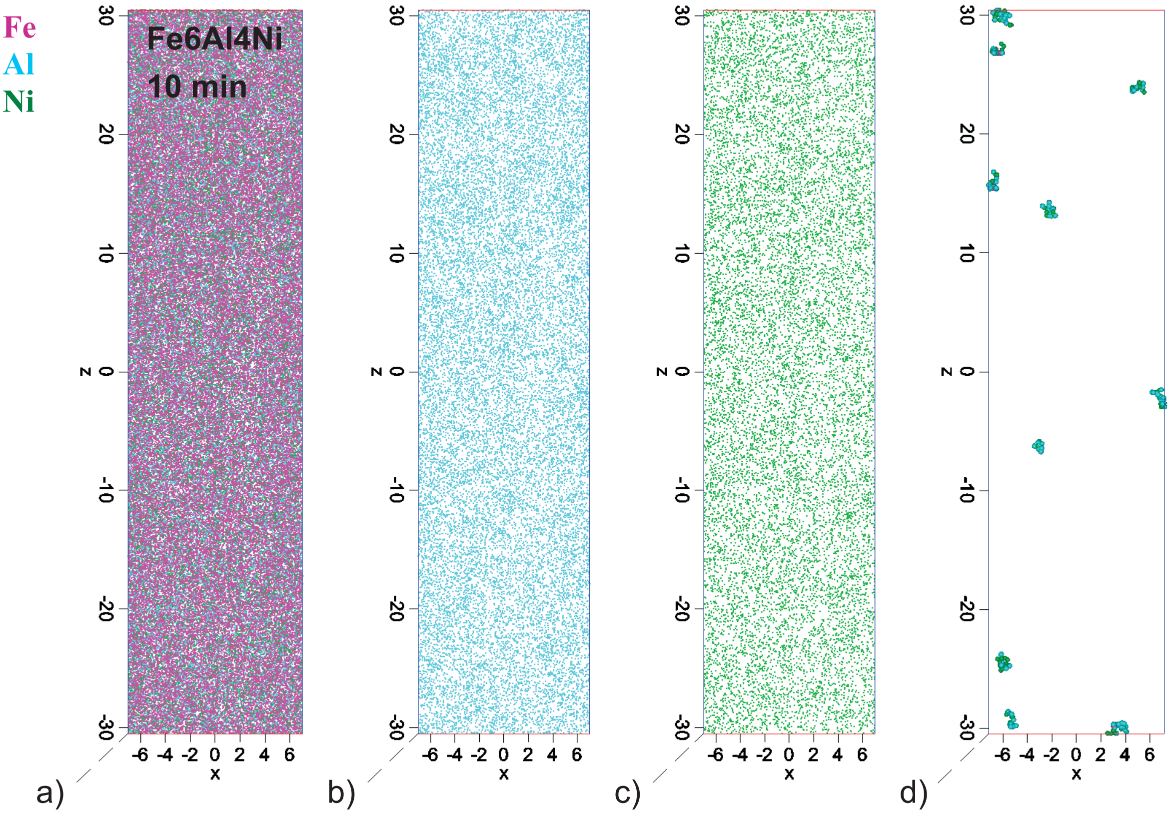

Figure 4.7: 3DAP reconstruction of the Fe6Al4Ni sample aged for 10 min at 500°C. a) all atoms, b) Al atoms, c) Ni atoms, d) detected clusters. Dimensions in nm, box size 14x17x61 nm^3.

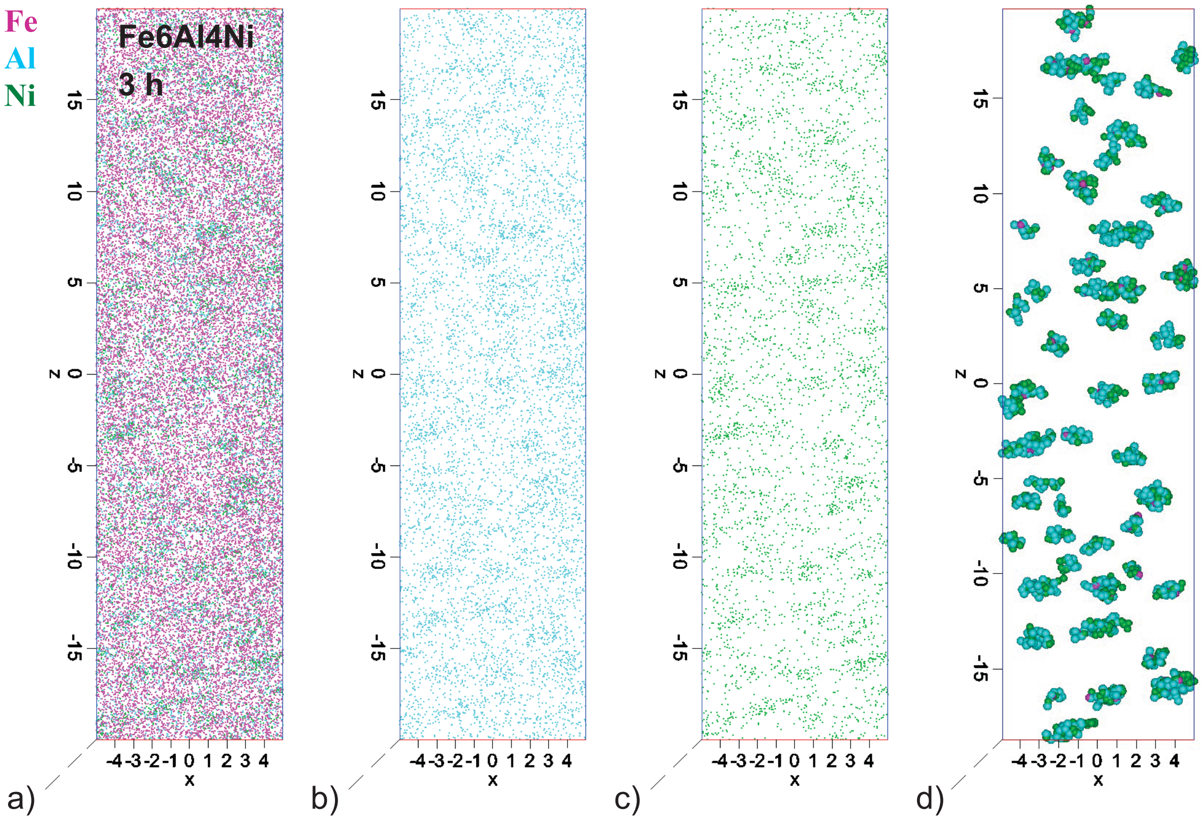

Figure 4.8: 3DAP reconstruction of the Fe6Al4Ni sample aged for 3 h at 500°C. a) all atoms, b) Al atoms, c) Ni atoms, d) detected clusters. Dimensions in nm, box size 10x10x40 nm³.

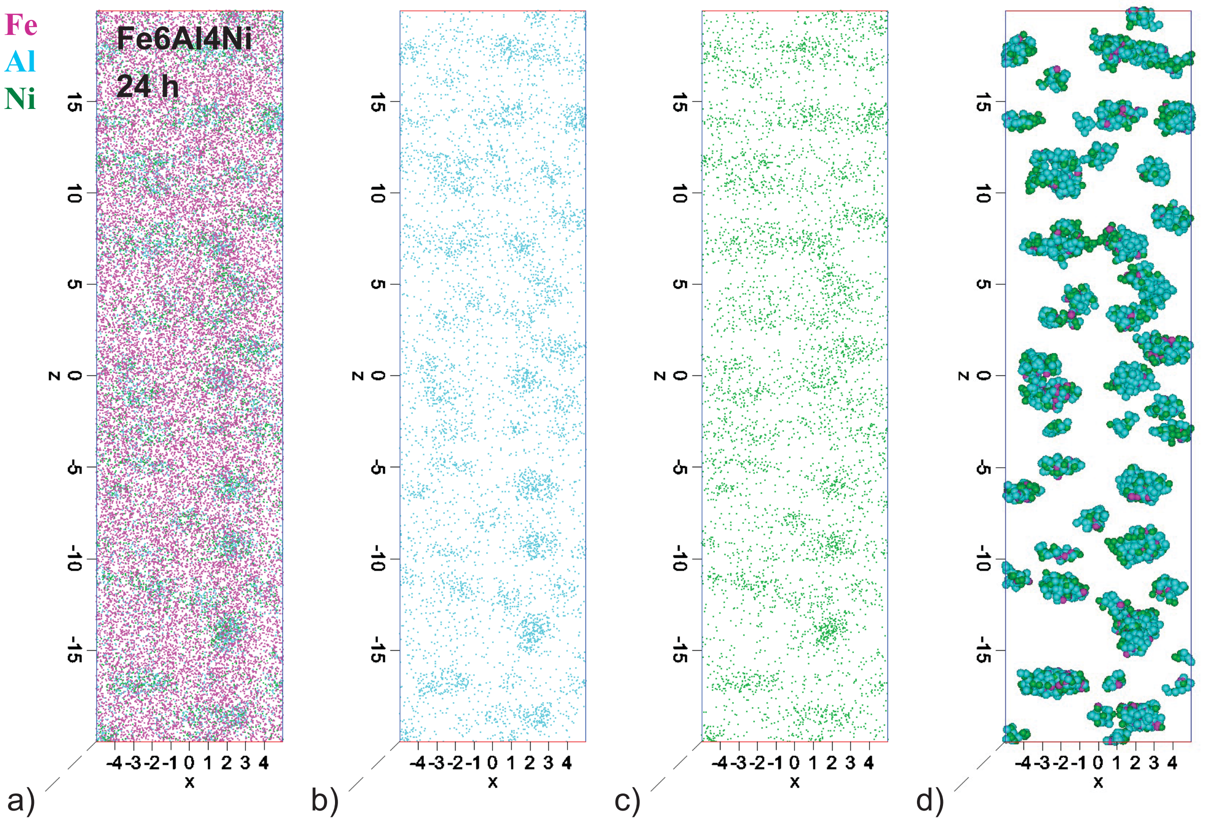

Figure 4.9: 3DAP reconstruction of the Fe6Al4Ni sample aged for 24 h at 500°C. a) all atoms, b) Al atoms, c) Ni atoms, d) detected clusters. Dimensions in nm, box size 10x10x40 nm³.

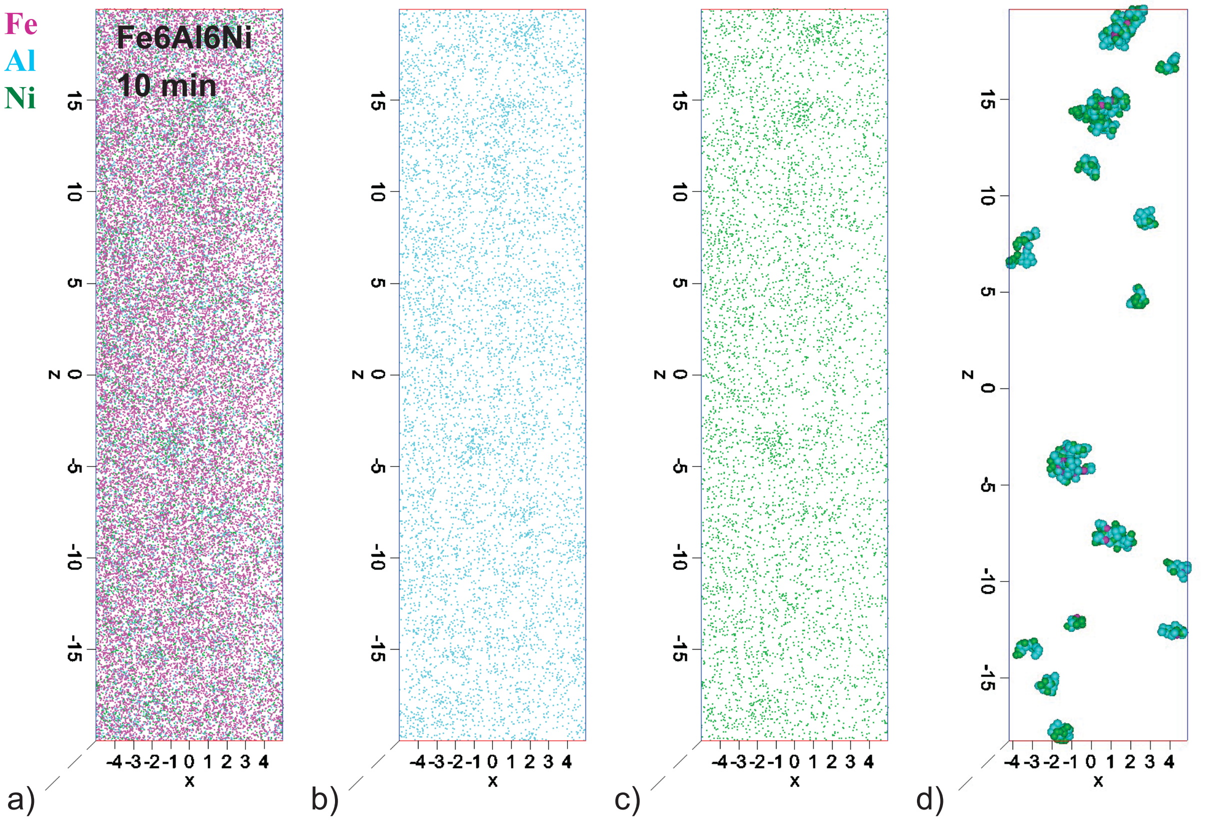

Figure 4.10: 3DAP reconstruction of the Fe6Al6Ni sample aged for 10 min at 500°C. a) all atoms, b) Al atoms, c) Ni atoms, d) detected clusters. Dimensions in nm, box size 10x10x40 nm³.

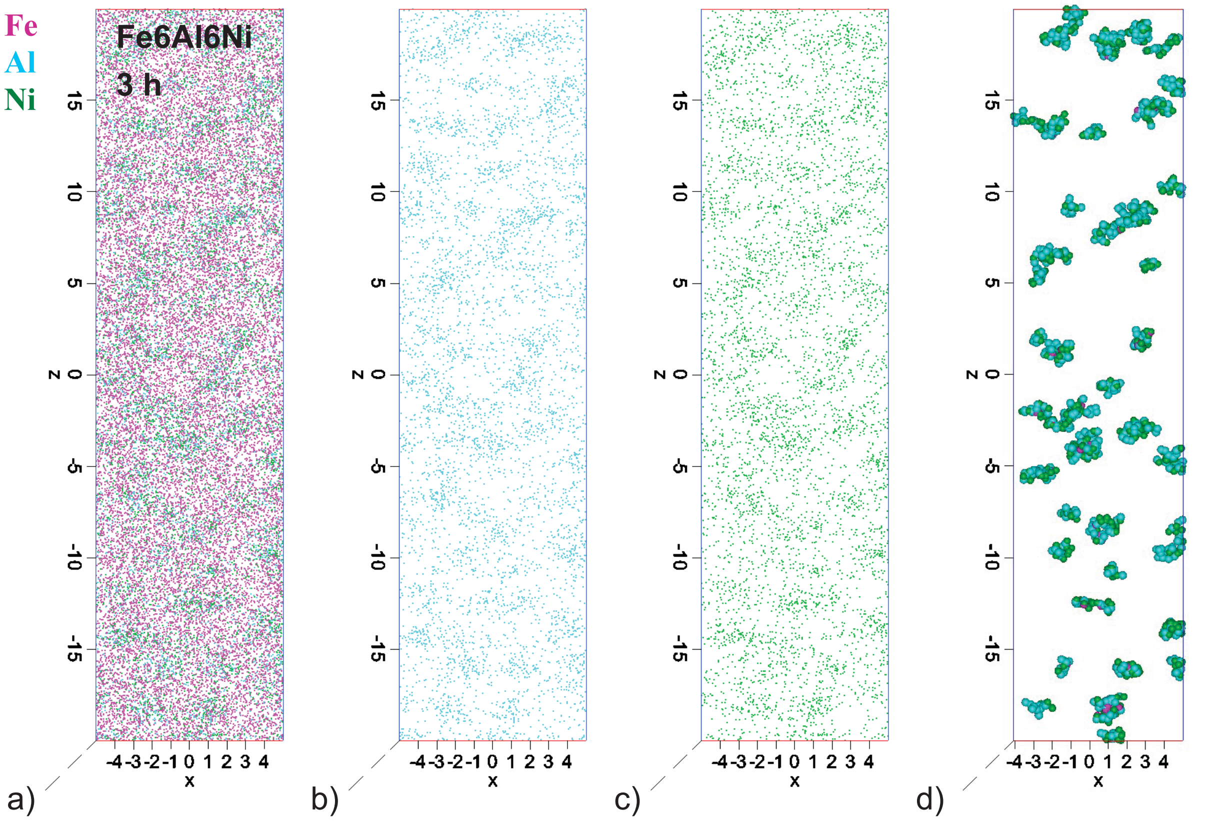

Figure 4.11: 3DAP reconstruction of the Fe6Al6Ni sample aged for 3 h at 500°C. a) all atoms, b) Al atoms, c) Ni atoms, d) detected clusters. Dimensions in nm, box size 10x10x40 nm³.

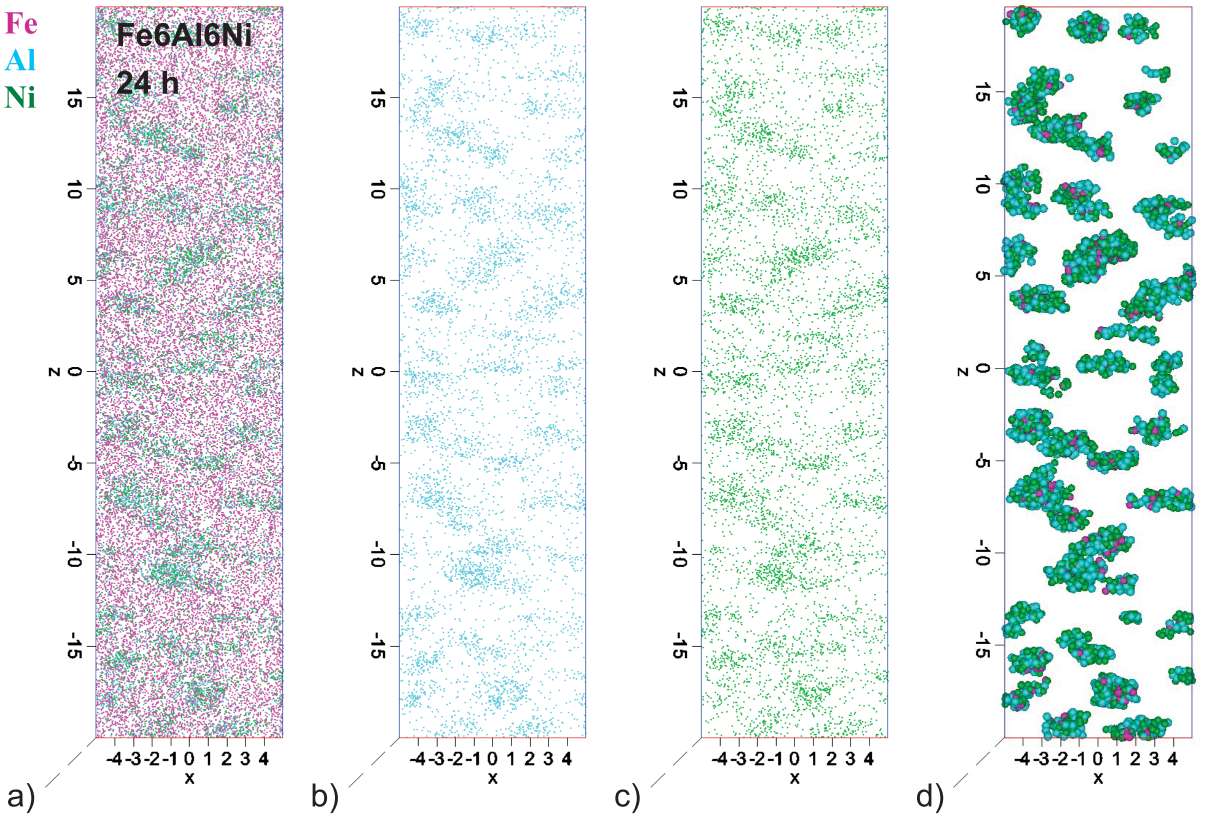

Figure 4.12: 3DAP reconstruction of the Fe6Al6Ni sample aged for 24h at 500°C. a) all atoms, b) Al atoms, c) Ni atoms, d) detected clusters. Dimensions in nm, box size 10x10x40 nm³.

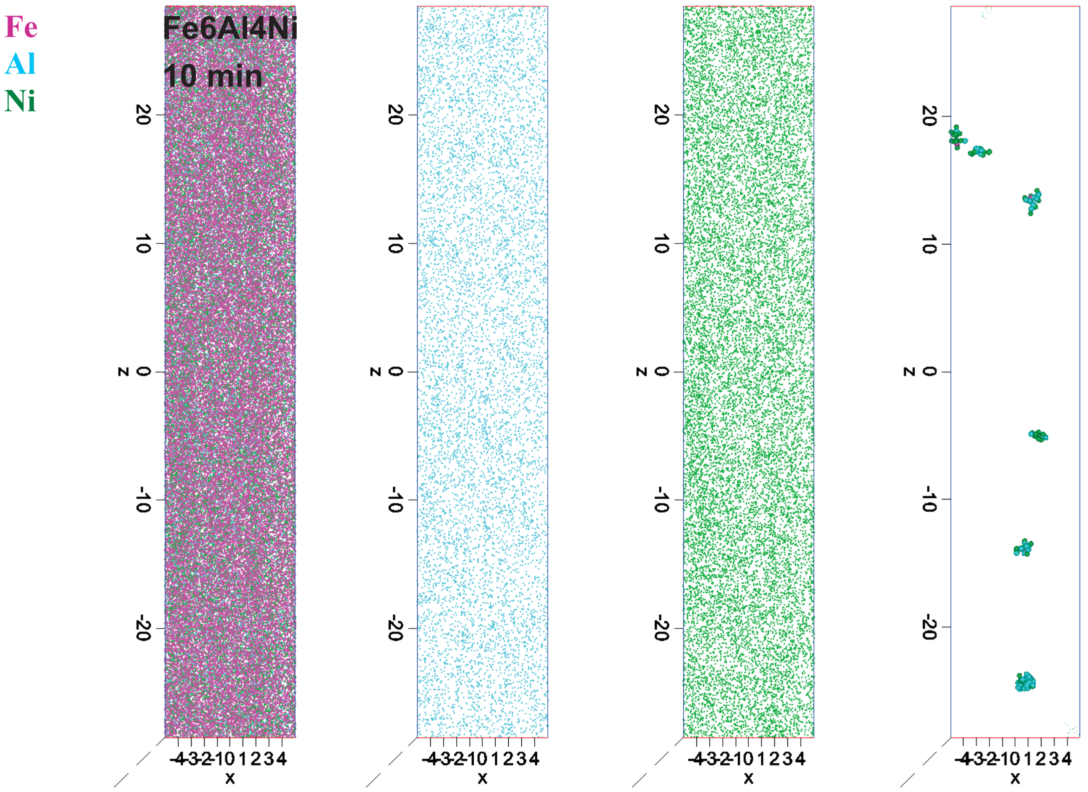

Figure 4.13: 3DAP reconstruction of the Fe4Al6Ni sample aged for 3 h at 500°C. a) all atoms, b) Al atoms, c) Ni atoms, d) detected clusters. Dimensions in nm, box size 10x19x57 nm³.

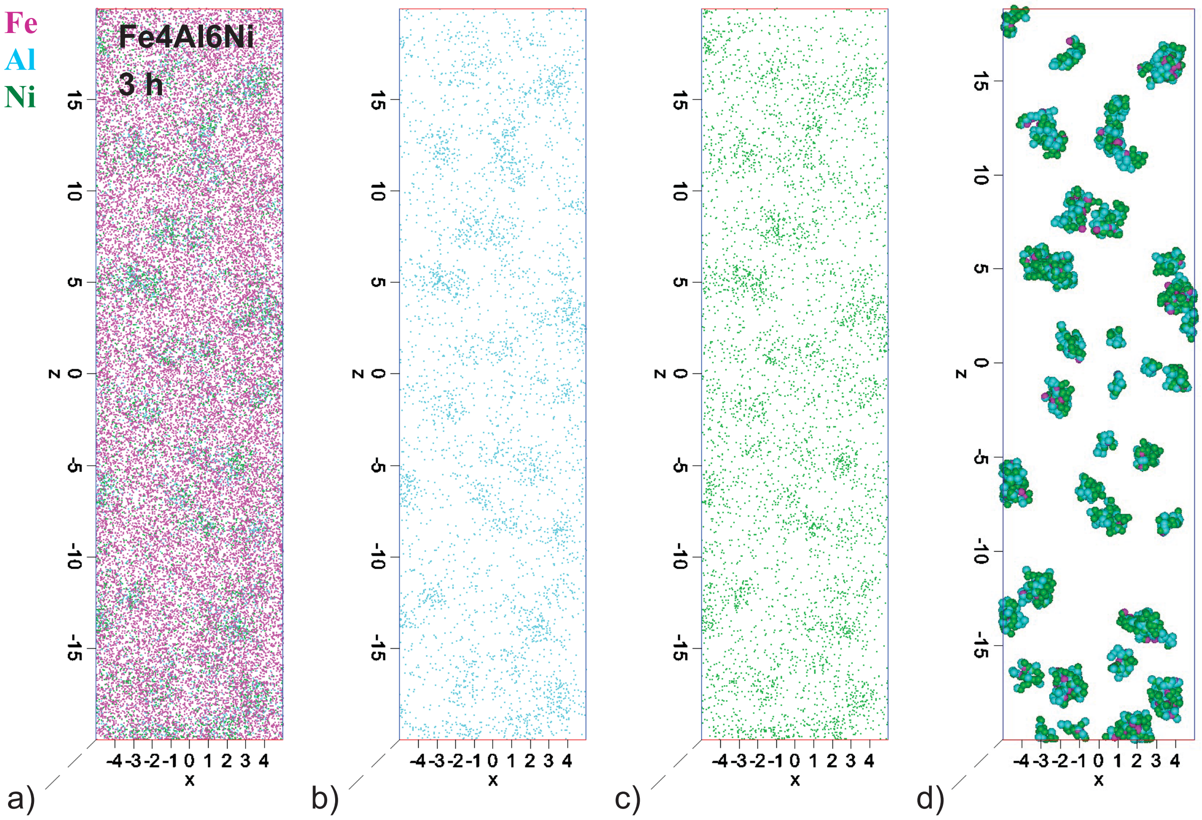

Figure 4.14: 3DAP reconstruction of the Fe4Al6Ni sample aged for 3 h at 500°C. a) all atoms, b) Al atoms, c) Ni atoms, d) detected clusters. Dimensions in nm, box size 10x10x40 nm³.

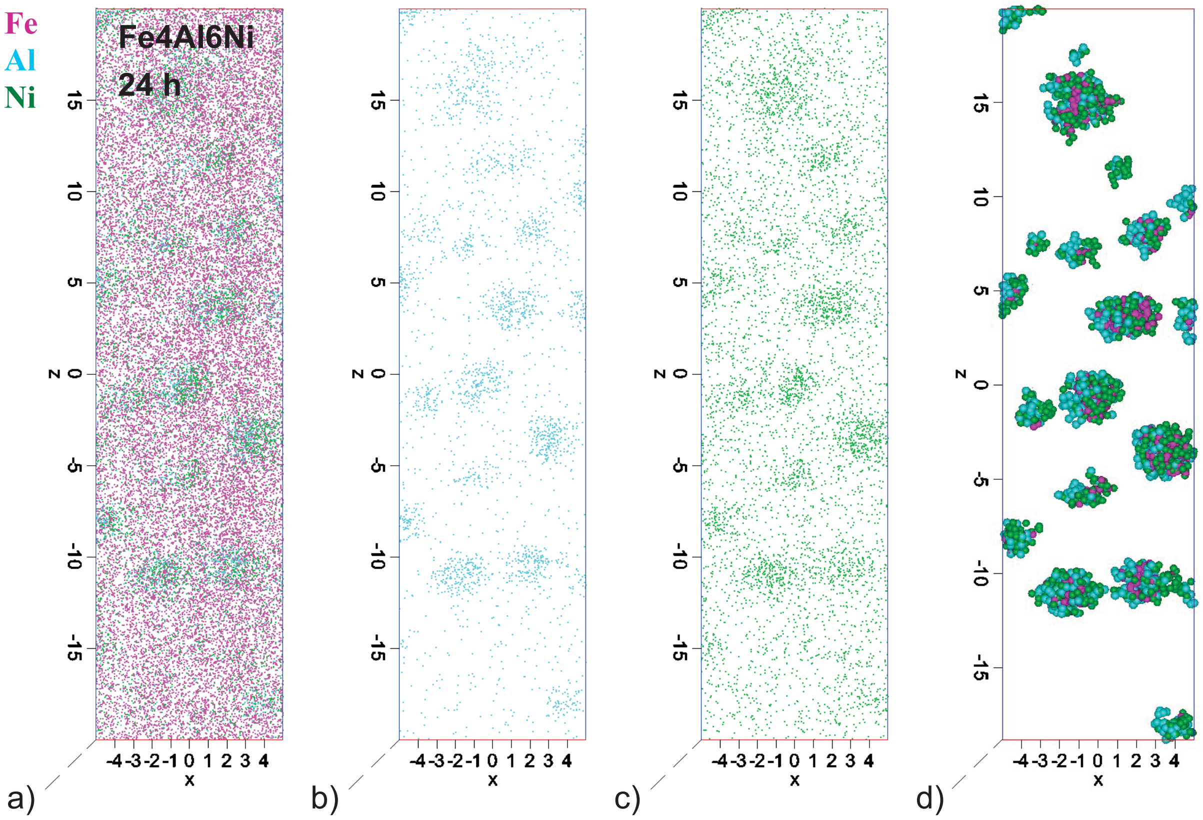

Figure 4.15: 3DAP reconstruction of the Fe4Al6Ni sample aged for 24h at 500°C. a) all atoms, b) Al atoms, c) Ni atoms, d) detected clusters. Dimensions in nm, box size 10x10x40 nm³.

Generally, the cluster development of the three model alloys is similar. For comparing the samples aged for 10 min of Fe6Al4Ni and Fe4Al6Ni with the other samples it is important to consider the different observed box sizes. In case of the samples aged for 10 min alloys Fe6Al4Ni (Figure 4.7(d)) and Fe4Al6Ni (Figure 4.13(d)) show only a small number of clusters whereas in the Fe6Al6Ni alloy (Figure 4.10(d)) more particles are present. Aging for 3 h leads to a strong increase of the number density in case of all three alloys. The size of the particles changes only a little during this aging sequence. Comparing the 3 h with the 24 h aged samples indicates a strong increase of the particle size. The number density does not fulfil a noticeable change in case of Fe6Al4Ni (Figure 4.8(d)), Figure 4.9(d)), Fe6Al6Ni (Figure 4.11(d)), Figure 4.12(d)) and seems to decrease in case of Fe4Al6Ni (Figure 4.14(d)), Figure 4.15(d)). The particles detected by the cluster algorithm are visible regarding the local arrangement of Al and Ni atoms in the observed volumes especially in case of the 3 h and the 24 h aged states.

The 3DAP investigations provide information on the particle development of the NiAl precipitates with respect to the size, number density, volume fraction and the composition. The results according to the precipitates determined by the cluster search algorithm are presented in Table 4-3.

Table 4-3: Radius, number density, volume fraction and composition of the NiAl precipitates and the surrounding matrix, calculated from the 3DAP data.

	Aged at 500°C	Radius [nm]	Number density [1/cm^3]	Volume [%]	Composition precipitates [at%]			Composition matrix [at%]		
					Fe	Al	Ni	Fe	Al	Ni
Fe6Al4Ni	10min	0.65	2.43×10^{17}	0.03	38.9±1.9	38.2±1.9	22.7±2.1	89.2	6.6	3.9
	3h	0.81	9.35×10^{18}	2.11	39.3±0.3	37.3±0.3	23.3±0.4	90.3	6.1	3.4
	24h	1.09	1.30×10^{19}	6.94	37.4±0.2	34.3±0.2	28.1±0.3	92.9	3.7	3.1
Fe6Al6Ni	10min	0.77	3.71×10^{18}	0.70	36.6±0.5	34.4±0.6	28.9±0.5	88.8	5.6	5.4
	3h	0.80	1.59×10^{19}	3.40	36.5±0.2	35.2±0.2	28.2±0.2	90.2	4.7	4.9
	24h	1.05	1.53×10^{19}	7.37	34.5±0.2	34.7±0.2	30.5±0.2	92.2	3.5	4.1
Fe4Al6Ni	10min	0.65	1.34×10^{17}	0.02	43.0±2.3	23.4±2.7	33.5±2.5	90.7	3.1	6.1
	3h	1.00	8.36×10^{18}	3.43	42.1±0.2	28.5±0.2	29.2±0.2	93.1	2.4	4.4
	24h	1.37	5.41×10^{18}	5.90	41.3±0.1	27.3±0.1	31.2±0.1	94.0	1.6	4.3

The increase of the mean particle size and the precipitated volume with increasing aging time is obvious for all three alloys. A strong increase in number density occurs for all three alloys between 10 min and 3 h of aging. The number density does not show a strong change between 3 h and 24 h aging in case of Fe6Al4Ni and Fe6Al6Ni. In contrast for Fe4Al6Ni the number density of the 24 h aged state decreases with respect to the 3 h aged state. After aging for 10 min only alloy Fe6Al6Ni shows a noticeable precipitated volume of 0.7 percent. Furthermore, the number density is a magnitude higher than that of the other two alloys. The Fe4Al6Ni alloy achieves the highest value for the mean radius of the precipitates with 1.37 nm after aging for 24 h whereas the precipitates of the two other alloys exhibit mean radii of approximately 1 nm at this aging time. All three alloys show a distinctive content of iron in the developing precipitates. The particles of the Fe6Al4Ni alloy show high Al and a low Ni content after aging for 10 min whereas for Fe4Al6Ni the contributions are contrary. Hence, the initial contribution of solute elements in the precipitates is correlated with the overall composition of the alloy. The more Al, Ni atoms are present in the matrix, the more Al, Ni atoms are found in the precipitates at the beginning of aging, respectively. Hence, the Al to Ni ratio of the alloy affects the Al to Ni ratio of the precipitates. While the iron content seems to decrease with aging time, the Ni and Al contents approach a Ni to Al ratio of 1. The depletion of solute atoms in the matrix with increasing aging time is also observable in Table 4-3.

Figure 4.16 shows the size distributions of the precipitated particles of all three investigated alloys.

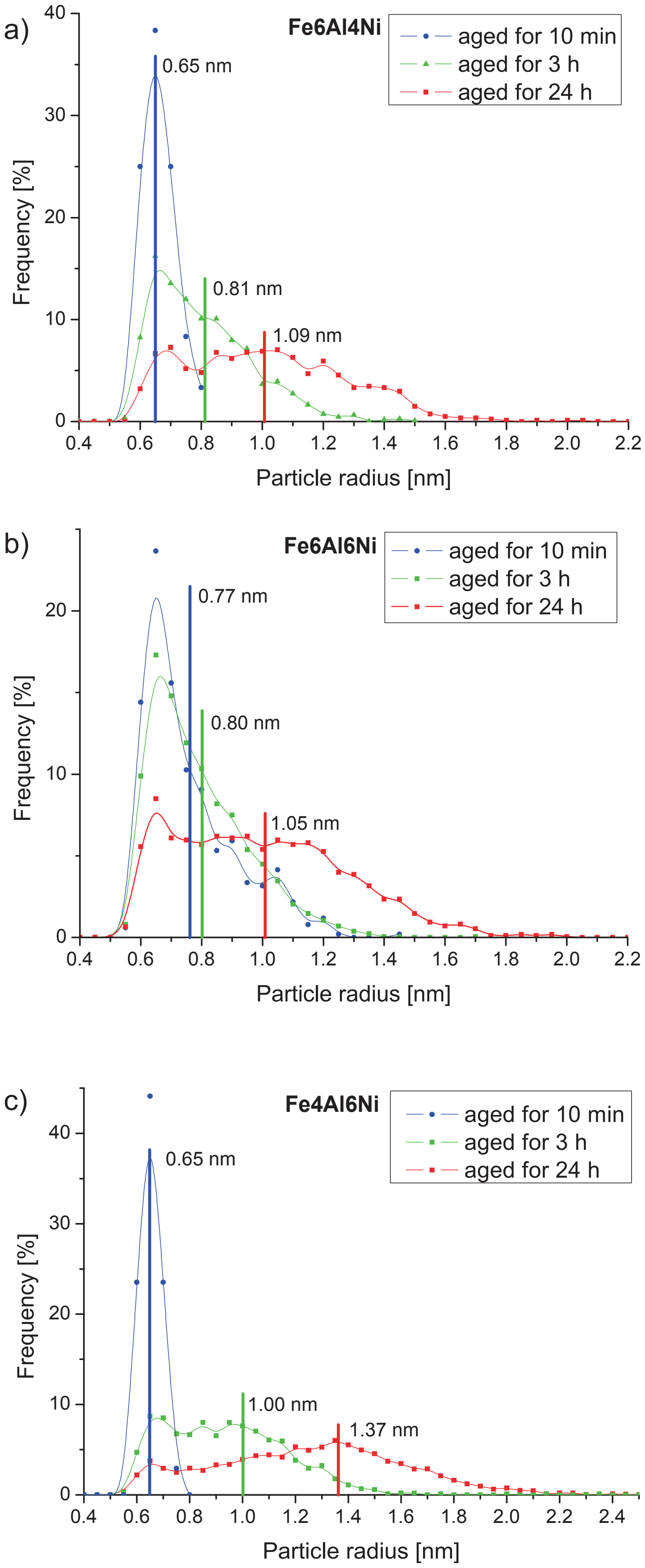

Figure 4.16: Particle size distributions of the 10 min, 3 h, and the 24 h aged state of a) Fe6Al4Ni, b) Fe6Al6Ni, c) Fe4Al6Ni. The vertical lines represent the mean radii of the according distribution.

The occurrence of particles in a selected radius range normalized to the overall number of particles in the observed volume is plotted in the diagram. The vertical lines depict the mean radii of the according distributions. The particle size covers a narrow range in the distributions of Fe6Al4Ni (Figure 4.16(a)) and of Fe4Al6Ni (Figure 4.16(c)) with a mean particle size of 0.65 nm after aging for 10 min. Alloy Fe6Al6Ni (Figure 4.16(b)) shows larger particles in addition to the fine sized majority after an aging time of 10 min. The fine particles are of the same size as calculated for the other two alloys mentioned before. Aging for 3 h leads to a broadening of the radius distribution to higher particle sizes. A decrease in the number of fine sized particles and the occurrence of larger particles is obvious for all three alloys. After aging for 24 h the particle sizes cover a large range. A noticeable peak in the size distributions according to particles with a size of approximately 0.65 nm can be seen in case of all aging states of the three alloys.

The composition of the precipitates listed in Table 4-3 are mean values covering the whole particles. Figure 4.17 represents the mean composition profiles of the particles found in the Fe6Al4Ni samples aged for 3 h (a) and 24 h (b). On the ordinate the atomic composition is plotted and the abscissa shows the normalized particle extent. The concentration profile of the precipitates ranges from the centre to the edge. Each cluster's maximum extent is normalized to value 1.0.

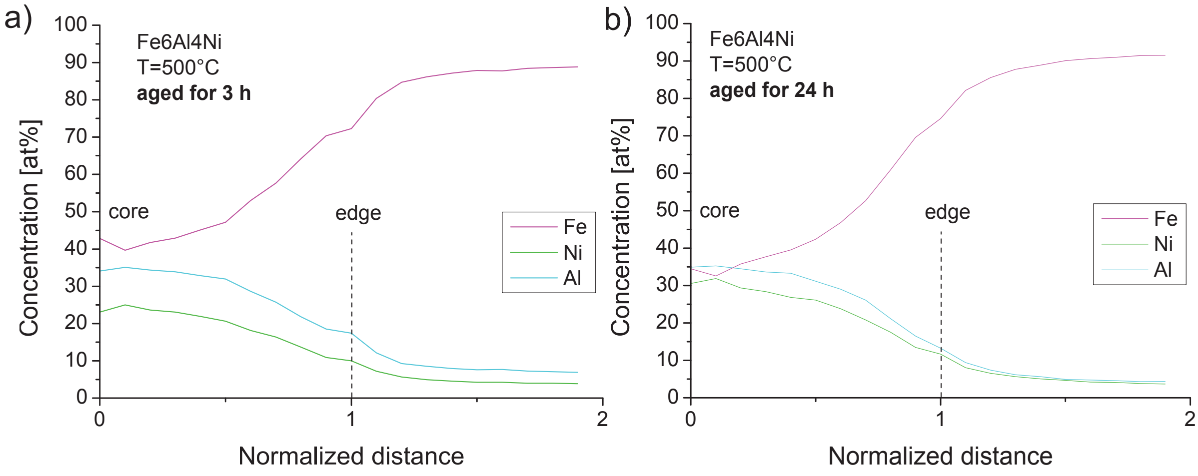

Figure 4.17: Cluster concentration profile of the Fe6Al4Ni alloy aged at 500°C for a) 3h, b) 24 h.

The core of the precipitates contains approximately 45 % Fe and shows an Al content of approximately 35 % and a Ni content of approximately 30 % after aging for 3 h. Regarding the composition profile of the particles in the 24 h aged sample indicates a decrease of the Fe content, an increase of the Ni content and the Al content is nearly the same as mentioned for the 3 h aged state. Figure 4.18 shows the cluster concentration profiles of the Fe6Al6Ni alloy.

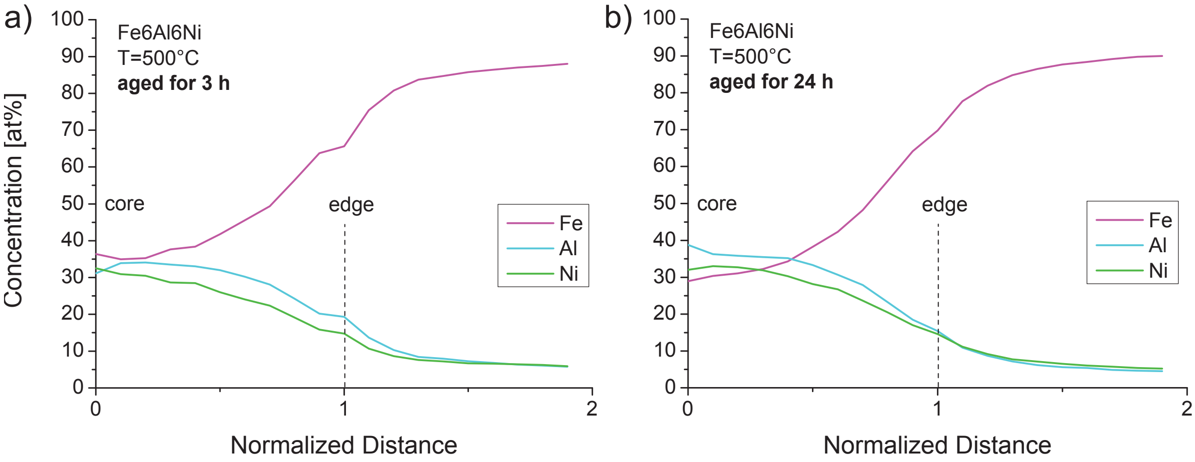

Figure 4.18: Cluster concentration profile of the Fe6Al6Ni alloy aged at 500°C for a) 3h, b) 24 h.

The Ni content does not fulfil a remarkable change during aging from 3 h (a) to 24 h (b). The 24 h aged sample contains more Al in the core of the precipitates and a decrease of the Fe content is obvious with respect to the precipitates of the 3 h aged sample. A noticeable aspect is that the precipitates contain more Al than Ni atoms though the alloy contains nearly the same amount of Ni and Al atoms. For the sake of completeness the cluster concentration profiles of the Fe4Al6Ni alloy aged at 500°C for 3h (Figure 4.19(a)) and for 24 h (Figure 4.19(b)) are shown.

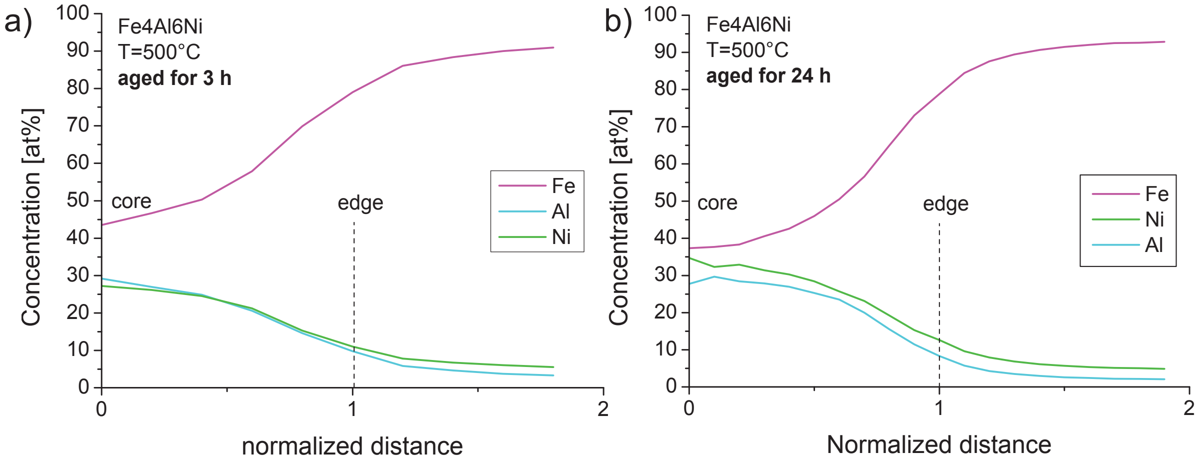

Figure 4.19: Cluster concentration profile of the Fe4Al6Ni alloy aged at 500°C for a) 3 h, b) 24 h.

The core contains 44 at% Fe, 28 at% Ni and 30 at% Al after 3 h of aging. The Fe content decreases, Ni increases and Al does not significantly change during further aging for 24 h.

All presented composition profiles show similar tendencies regarding the composition development from the core to the edge of the particles: The content of solute atoms decreases and the Fe content increases towards the particle edge. At a normalized particle distance of approximately 1.7 the overall matrix composition is existent.

4.4 SANS

4.4.1 Static experiments

The scattering curves of the static samples are shown in Figure 4.20. For all three model alloys the shift of the magnetic scattering cross sections to higher values with increasing aging time is obvious.

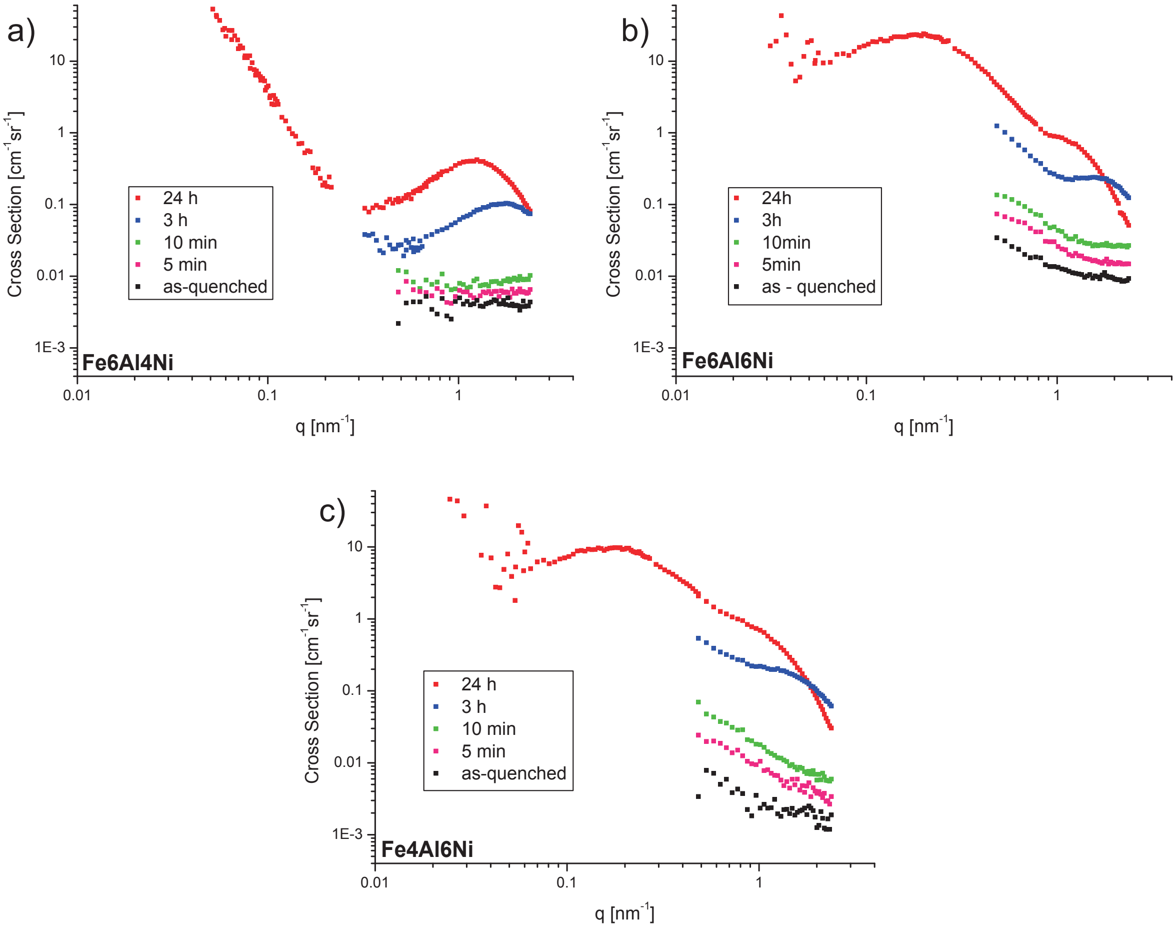

Figure 4.20: Scattering cross sections vs. scattering vector q for different aging states of a) Fe6Al4Ni, b) Fe6Al6Ni, c) Fe4Al6Ni.

The samples aged for 3 h and 24 h, which show sufficiently distinctive peaks, can be used to fit the scattering curves to obtain information on the developing precipitates. The 24 h aged samples have been measured at detector distances up to 21 m, therefore, the datasets range to lower scattering vectors q (see chapter 3.5.4). However, alloy Fe6Al4Ni (Figure 4.20(a)) shows a strong distinctive peak in case of the samples aged for 3 h and 24 h. The peak moves to lower scattering vectors with increasing aging time. At lower scattering vectors the curvature of the 24 h aged sample shows a linear dependence. The statistic is insufficient for low scattering vectors in case of Fe6Al6Ni (Figure 4.20(b)) and Fe4Al6Ni (Figure 4.20(c)). Alloys Fe6Al6Ni and Fe4Al6Ni show different scattering characteristics compared to the Fe6Al4Ni alloy. The curvatures of the 24 h aged samples present two peaks. One peak is in the q-range like in the curvature of the Fe6Al4Ni alloy and a considerable second peak with a maximum at approximately 0.2 nm^{-1} is existent. This peak seems also to be present at shorter aging times but these samples have only been measured at 1 m detector distance which restricts the q-range.

In order to provide quantitative values for the radius, number density and volume fraction of the precipitated NiAl particles, the magnetic SLDD’s have to be calculated. Therefore, the compositions obtained by 3DAP are used as input. Details concerning assumptions and the calculation of the magnetic SLDD’s according to the magnetic as well as to the non-magnetic assumption are given in section 3.5.6. The results obtained by fitting static magnetic scattering curves are shown in Table 4-4. The magnetic SLDD’s calculated according to each sample state have been used.

Table 4-4: Determined values for radius, number density and precipitated volume from the fitted static magnetic scattering curves. Calculations have been done for the assumption of magnetic as well as of non-magnetic precipitates.

	Aged at 500°C	Magnetic assumption	Radius [nm]	Number density [$1/cm^3$]	Volume [%]
Fe6Al4Ni	3h	mag.	0.86	$9.36 \times 10^{19} \pm 2.47 \times 10^{18}$	20.5
		non-mag.	0.69	$3.25 \times 10^{19} \pm 1.50 \times 10^{18}$	4.0
	24h	mag.	1.25	$2.07 \times 10^{19} \pm 7.69 \times 10^{16}$	14.6
		non-mag.	1.07	$9.59 \times 10^{18} \pm 2.97 \times 10^{16}$	4.4
Fe6Al6Ni	3h	mag.	1.14	$2.94 \times 10^{19} \pm 1.77 \times 10^{18}$	17.3
		non-mag.	0.86	$2.08 \times 10^{19} \pm 1.50 \times 10^{18}$	5.3
	24h	mag.	1.68	$1.40 \times 10^{19} \pm 5.12 \times 10^{16}$	14.4
		non-mag.	1.51	$2.54 \times 10^{18} \pm 3.43 \times 10^{16}$	3.6
Fe4Al6Ni	3h	mag.	1.03	$5.85 \times 10^{20} \pm 7.69 \times 10^{18}$	15.0
		non-mag.	1.08	$7.38 \times 10^{18} \pm 2.21 \times 10^{17}$	2.6
	24h	mag.	1.78	$2.81 \times 10^{19} \pm 6.11 \times 10^{16}$	11.9
		non-mag.	1.69	$4.89 \times 10^{18} \pm 3.30 \times 10^{16}$	3.0

The SANS experiments indicate an increase of the particle radius with increasing aging time whereas the number density shows a decrease from the 3 h to the 24 h aged state. Assessing results for magnetic and non-magnetic particles indicates noticeable differences for the two assumptions, especially for the volume fraction and the number density. The calculated radii are influenced as well. The volume fraction covers values from 14 to 20.5 % and decreases with aging time in case of magnetic calculations. Assuming non-magnetic precipitates, mean particle radii of 1.07 nm for Fe6Al4Ni, 1.51 nm for Fe6Al6Ni and 1.69 nm for Fe4Al6Ni after 24 h of aging are obtained. The volume fraction after aging for 24 h ranges from 3 to 5.3 % with the highest value for the Fe6Al6Ni and the lowest value for the Fe4Al6Ni alloy.

4.4.2 Isothermal in-situ experiments

Measurements during isothermal aging at 500°C have been performed on all three model alloys. As a visualization of the development of the scattering cross section with increasing aging time Figure 4.21 presents a series of scattering curves measured on the Fe6Al4Ni alloy.

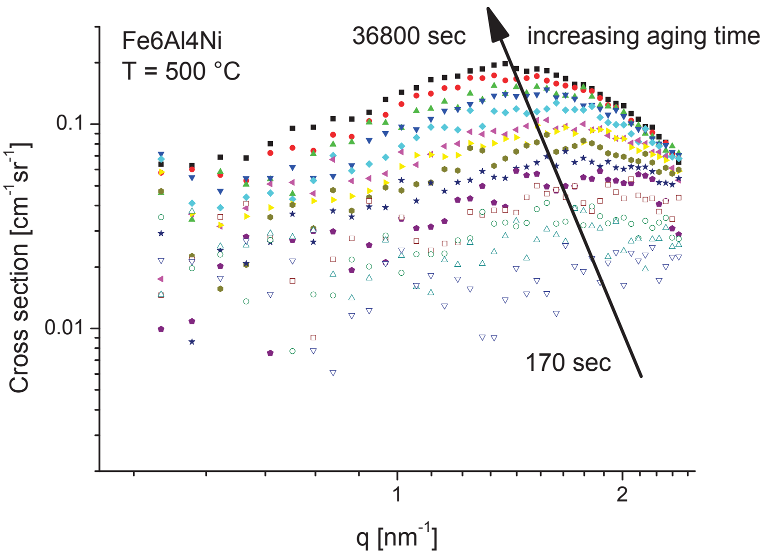

Figure 4.21: Development of the magnetic scattering curve with respect to increasing aging time yielded by the in-situ experiment. Alloy Fe6Al4Ni, aged at 500°C.

The bottom curve belongs to an aging time of 170 sec and is characterized by poor statistics. With increasing aging time a general increase of the scattering cross section and the development of a peak which moves towards lower scattering vectors q are obvious. The similarity to the shape of the curves of the static experiments (Figure 4.20(a)) can bee seen. The evaluation of the magnetic scattering curves is carried out in the same way like it is mentioned for the static experiments. Here only non-magnetic precipitates have been assumed. In Figure 4.22 the development of radius, volume fraction and number density with aging time according to the magnetic scattering curves in Figure 4.21 is presented. Due to poor statistics at early aging times, the evaluation for this sample begins at an aging time of 3600 sec.

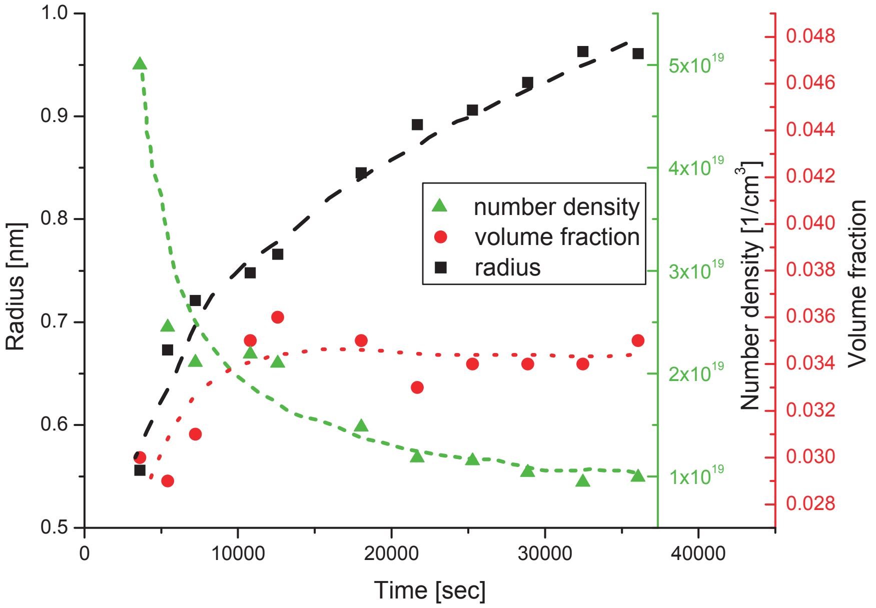

Figure 4.22: Development of the radius, volume fraction and the number density of the Fe6Al4Ni alloy with increasing aging time. The dashed and dotted lines represent the schematic characteristics.

The particle radius grows continuously with increasing aging time until the end of the experiment. The volume fraction increases up to an aging time of approximately 4 h (14400 sec) and becomes constant. The number density shows a high value after 1 h (3600 sec) of aging. The subsequent decrease runs out into a constant number density after an aging time of approximately 9 h (32400 sec).

4.4.3 R-Value

Figure 4.23 represents the development of the nuclear (Q_{nuc}) and the magnetic (Q_{mag}) integral intensities and the according R-value with aging time of the three investigated alloys. Before plotting, the curves have been modified in a way, that the values of the magnetic and the nuclear integral intensity of the first 5 data points have been averaged and subtracted from all values. With this correction the scattering contributions of the initial solution annealed state and the temperature influence on the nuclear scattering are eliminated. Since the static samples have been measured at room temperature no temperature correction was necessary but the scattering signal of the as-quenched state has been subtracted as well.

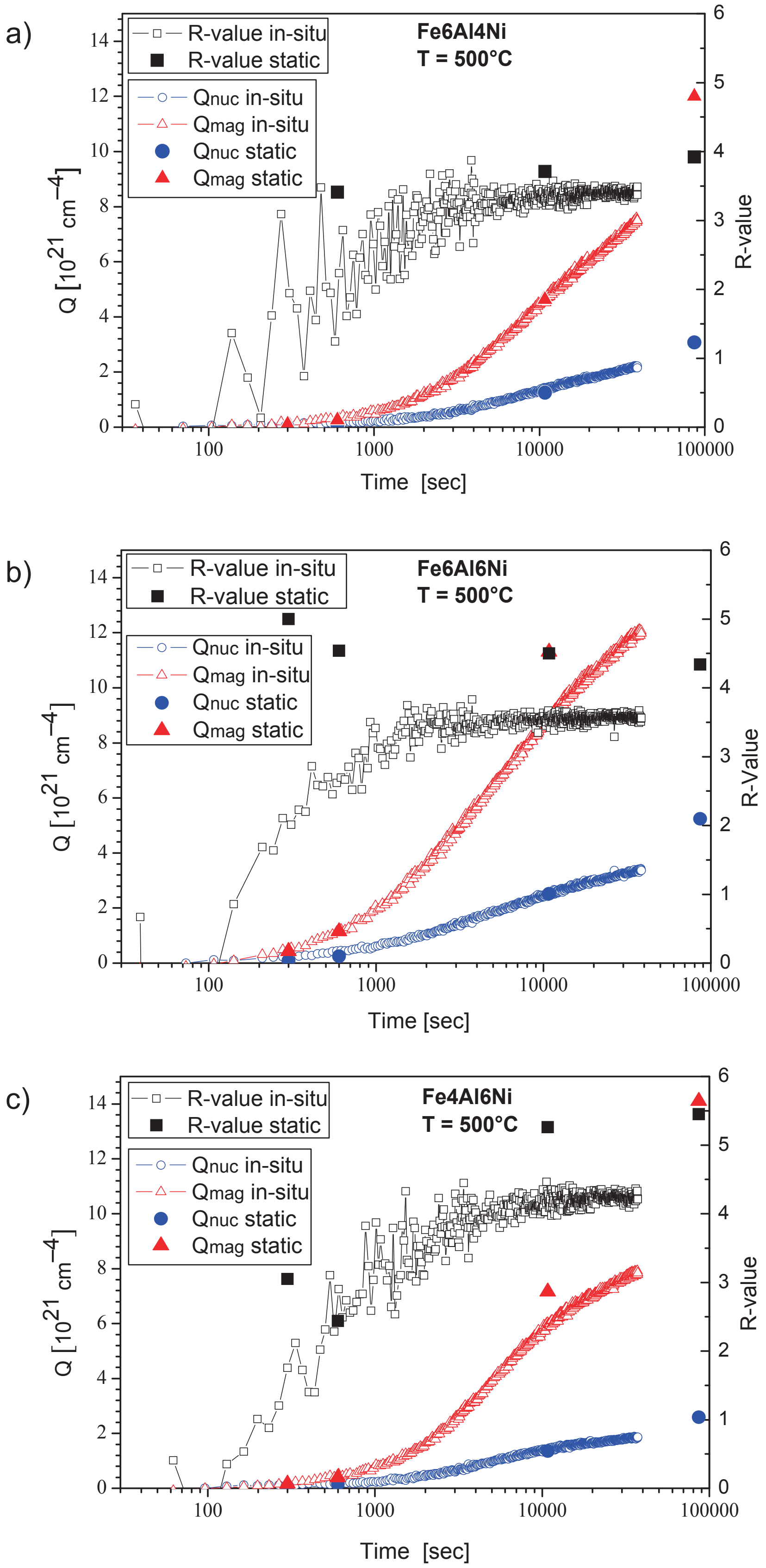

Figure 4.23: Development of the magnetic and the nuclear integral intensities and the R-value with running aging time of a) Fe6Al4Ni, b) Fe6Al6Ni, c) Fe4Al6Ni.

For all three alloys the R-value increases rapidly after an aging time of approximately 100 sec. With ongoing aging the curvatures open out into a nearly horizontal plateau. Table 4-5 presents the theoretically calculated R-values assuming non-magnetic as well as magnetic particles and the R-values calculated from the experimental SANS data.

Table 4-5: R-values determined by theoretical calculation and by evaluating scattering experiments.

		Theoretical		Evaluated curves	
		non-mag / mag		Static	in-situ
Fe6Al4Ni	10min	4.7	1.4	3.41	2.5
	3h	4.9	1.5	3.71	3.5
	24h	5.6	1.8	3.92	
Fe6Al6Ni	10min	5.9	1.8	4.54	2.8
	3h	5.3	1.7	4.50	3.6
	24h	5.4	1.8	4.34	
Fe4Al6Ni	10min	13.8	3.0	2.44	2.4
	3h	7.8	2.0	5.26	4.2
	24h	8.4	2.2	5.45	

The theoretically estimated values differ from the experimental data but they show a general tendency: The experimental R-values are situated between the magnetic and the non-magnetic assumption. The curvatures as depicted in Figure 4.23 indicate that the R-values of the alloys Fe6Al4Ni and Fe6Al6Ni are similar after aging for approximately 10 h (36000 sec) at 500°C. Alloy Fe4Al6Ni shows a higher R-value which is confirmed by the theoretical R-values.

4.4.4 Continuous in-situ experiments

The integral intensity of the magnetic and the nuclear scattering curves of the continuous experiments are an indicator for the start temperature of the precipitation reaction. Figure 4.24 presents the development of the integral intensities according to the Fe6Al4Ni sample heated with a rate of 15 K/min.

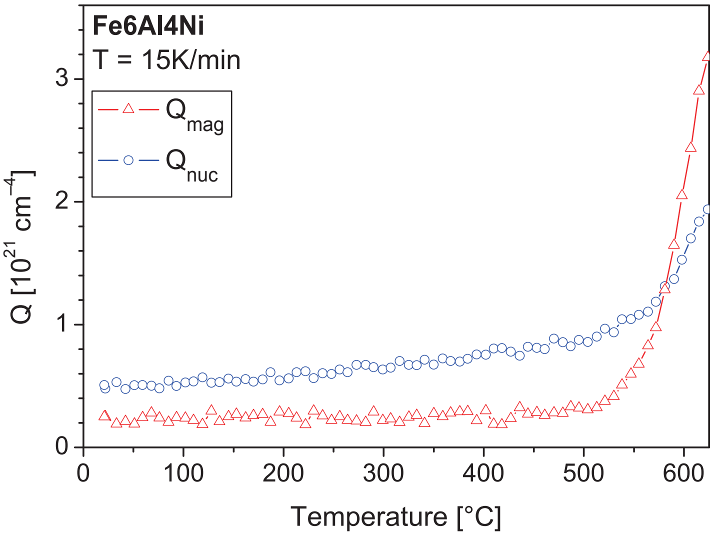

Figure 4.24: Magnetic and nuclear integral intensity according as a function of time. Heating rate 15 K/min performed on the Fe6Al4Ni alloy.

The nuclear integral intensity shows a continuous increase during the heating process whereas the magnetic integral intensity is constant. At a temperature of approximately 500°C the magnetic integral intensity strongly increases. The nuclear integral intensity shows the increase at approximately 560 °C. Figure 4.25 shows the development of the magnetic integral intensity during heating with 15, 23 and 36 K/min of the Fe6Al4Ni sample.

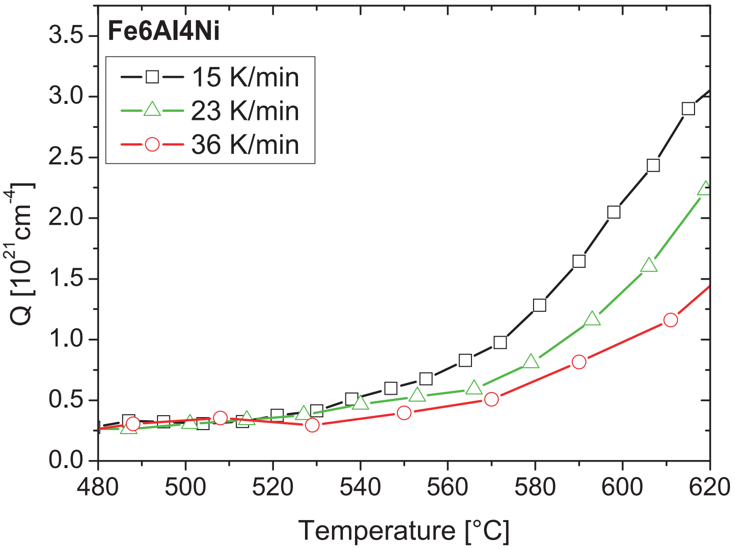

Figure 4.25: Magnetic integral intensity according to the continuous in-situ SANS experiments performed at heating rates 15, 23, 36 K/min on the Fe6Al4Ni alloy.

The increase of the magnetic integral intensity indicates the onset of the precipitation reaction. A shift of the start temperature of the precipitation reaction with increasing heating rates to higher temperatures is visible.

5 Discussion

A quantitative comparison of mechanical properties like hardness is not reasonable for the three model alloys since the microstructure differs significantly. According to the phase diagram in Figure 2.16 the Fe6Al4Ni alloy is solution treated in the α – region. Therefore, no grain refining during the $\gamma - \alpha$ transformation occurs. This explains the large grain size of this alloy as seen in Figure 3.1(a). The lattice parameter misfit with respect to pure α-Fe (Figure 3.2(b)) is caused by the lattice widening due to the substitution of solute nickel and aluminium atoms. Iron and nickel have similar atomic radii whereas the radius of aluminium is significantly higher. The measured lattice widening with respect to the aluminium contents of the alloys agrees with this fact. The substitution of Ni and Al causes a solid solution strengthening which influences the vertical position of the hardness over aging time curves in Figure 4.1. Generally, the curves show three characteristic regions. For Fe6Al4Ni and Fe4Al6Ni the first 300 sec of aging can be seen as an incubation period where the nucleation process is unstable. The higher super-saturation of the Fe6Al6Ni alloy causes a higher driving force for the precipitation reaction. Therefore, hardness continuously increases from the beginning of aging. The generally higher super saturation of the Fe6Al6Ni alloy causes the comparatively high precipitated volume of 0.7% (Table 4-3, Figure 5.2(b)) after 10 min of aging. The time range from 300 sec to approximately 24 h is dominated by particle growth and hardness reaches a maximum which indicates the beginning of a coarsening stage.

The as-quenched sample is the initial state. Solute Al and Ni atoms are homogeneously distributed in the matrix since the nearest neighbour distance distributions of the 3DAP reconstructions are identical with that of a randomized arrangement of the atoms (Figure 4.6). The 10 min (600 sec) aged sample approximately marks the point where the hardness curve begins to follow a constant ascending slope which is assumed to be the initiation of stable nucleation and growth. Aging for 24 (86400 sec) hours represents a sample state in the range of the hardness maximum which stands for the starting of coarsening. The state aged for 3 h (10800 sec) is situated between these two characteristic states. Defining strictly separated stages during the transformation is only a theoretical approach. In reality the mechanisms of nucleation, growth and coarsening overlap. This can be seen in the developing particle size distributions in Figure 4.16. Aging does not only lead to a strict shift of the initial distribution to higher radii, the distribution becomes also broadened. The noticeable peak at a radius of approximately 0.65 nm can be seen in all aging states which leads to the assumption that the creation of new clusters is still going on. Hence, nucleation, dissolution and growth happen simultaneously. Furthermore, the classical nucleation and growth theory is not applicable since the composition of the precipitates also changes while the particle size increases which agrees with the results of [29, 30, 34]. The smallest particles in the size distributions must not necessarily be the smallest particles occurring in the sample. The minimum value for the radius is restricted by the cluster search algorithm. The alloys investigated in the present work contain high amounts of solute Ni and Al atoms and therefore, parameter N_{min} has to be chosen in a range which guarantees that no random fluctuations in the alloy are interpreted as a cluster. Value 15 has been found to be suitable for the parameter N_{min}. Considering the Fe content of about 40 at% in the precipitates and the detector efficiency (33 %) of the 3DAP leads to minimally detectable real particle sizes of approximately 0.6 nm radius. A detected cluster containing 15 Ni+Al atoms consists of approximately 60 atoms in reality, which leads to the mentioned minimally detectable real size. No extraordinary large particles have been detected in the 3DAP data and therefore, the source of the peak at scattering vector $q \approx 0.2\ nm^{-1}$ in the scattering curves of Fe6Al6Ni (Figure 4.20(b)) and Fe4Al6Ni (Figure 4.20(c)) could not be identified. Fitting of the SANS curves concerns only the peak at scattering vector $q \approx 1.5\ nm^{-1}$ (Figure 4.20(a,b,c)). Fitting is not reasonable for curvatures with bad statistics, therefore, the 5 min aged and 10 min aged states in Figure 4.20 can only be seen as an illustration of particle development with respect to the as-quenched state in case of all three model alloys. The definitive shape of the peak and its maximum of the Fe6Al4Ni alloy (Figure 4.20(a)) are a result of scattering interferences of the occurring precipitates [57]. Due to high number densities the distance between the particles is small and therefore, scattering interferences occur. Table 4-4 provides the calculated characteristics of the precipitates for all aging states of the three model alloys. The results differ significantly in case of the magnetic and the non-magnetic assumption, especially in the volume fraction and the number density. Generally, more particles are determined in case of magnetic calculations due to the lower scattering contrast which is generated by magnetic particles. The radius is independent of the chosen SLDD since the radius is related with the scattering vector according to the peak maximum of the scattering curve. The radius differences between the two assumptions can be explained by a marginal shift of the fitting function using different SLDD’s.

The composition development of the precipitates, as listed in Table 4-3, shows that the precipitates contain a remarkable amount of Fe atoms ranging from 34 to 43 at% after 24 h of aging at 500°C. Previous investigations performed at different aging temperatures and aging times show a noticeable amount of remaining Fe as well [25, 34] and reveal Ni to Al ratio of nearly 1 [25, 29, 33, 34]. Although the amounts of Al and Ni atoms in the as-quenched Fe6Al6Ni sample are approximately identical, more Al is found in the precipitates after aging. The Fe4Al6Ni alloy, the alloy with the lowest Al content, shows the highest amount of Fe in the precipitates. Additionally, this alloy remarks the smallest fraction of precipitated volume. Generally, the Al content of the alloy seems to primarily affect the volume fraction, which agrees with [31], and the remaining Fe content of the precipitates.

The R-value development as shown in Figure 4.23 is a qualitative indicator for the composition development in the precipitates. Comparing the results for the static and the in-situ experiments as listed in Table 4-5 illustrates that the determined R-values differ. Due to the rapid increase of the R-value in the range of 5 (300 sec) to 10 min (600 sec) of aging, small differences of the experimental parameters like the furnace temperature influence the results significantly. The differences in case of the longer aged samples are not clear. One possibility could be a difference in the saturation magnetization at the two measuring conditions (RT, 500°C). The R-value is influenced by the compositions of matrix and precipitates as described in sections 3.5.6, 3.5.7, 3.5.8. Since the alloys contain two elements which cause magnetic moments (Fe, Ni) there are two concurring processes in the matrix and in the precipitates which lead to a change in the magnetic scattering contrast. On the one hand the increase of Fe content in the matrix and the according decrease of remaining Fe in the precipitates and on the other hand the decrease of solved Ni in the matrix and the change of Ni content in the precipitates. Additionally, the development of all three elements influences the nuclear scattering contrast. As depicted in Figure 4.23(b) alloy Fe6Al6Ni reaches the plateau after an aging time of approximately 2000 sec, Fe6Al4Ni (Figure 4.23(a)) after approximately 6000 sec, whereas the R-value of alloy Fe4Al6Ni (Figure 4.23(c)) reaches the plateau after approximately 20000 sec of aging. This order of reaching a nearly constant composition agrees with the results given by the atom probe experiments (Table 4-3). Since the change of Fe content with aging time in the matrix and in the precipitates is similar for the three alloys, the development of the Ni, Al contents explains the R-value characteristics. The ratio of the Al to the Ni content in the precipitates after aging for 10 min is 1.19 for alloy Fe6Al6Ni, 0.70 for Fe4Al6Ni and 1.68 for Fe6Al4Ni. As mentioned above the composition of the precipitates approaches an Al to Ni ratio of 1 during aging. Therefore, it is assumed that the higher the deviation of the Al to Ni ratio of the precipitates' composition, the longer is the time to reach the R-value plateau. Alloy Fe6Al6Ni reaches the plateau at shortest aging time, agreeing with the lowest deviation of the Al to Ni ratio from value 1. Although alloy Fe6Al4Ni shows the higher deviation than the Fe4Al6Ni alloy and the diffusivity of Al and Ni in α-Fe is nearly the same, Fe6Al4Ni reaches the R-value plateau at a shorter aging time. Table 4-3 illustrates that the content of remaining Ni in the Fe6Al4Ni matrix is higher than the content of remaining Al in the Fe4Al6Ni matrix. In case of Fe6Al4Ni the matrix offers more required solute atoms, therefore, the diffusion paths to the precipitates are shorter and the aspired composition is achieved earlier.

5.1 Linkage of 3DAP and SANS

SANS curves are evaluated by numerical approaches and by the utilization of additional analytical methods. In the present work, 3DAP data have been used to support the SANS evaluations. Figure 5.1 represents the linkage of the different examination methods with respect to the input parameters and the results.

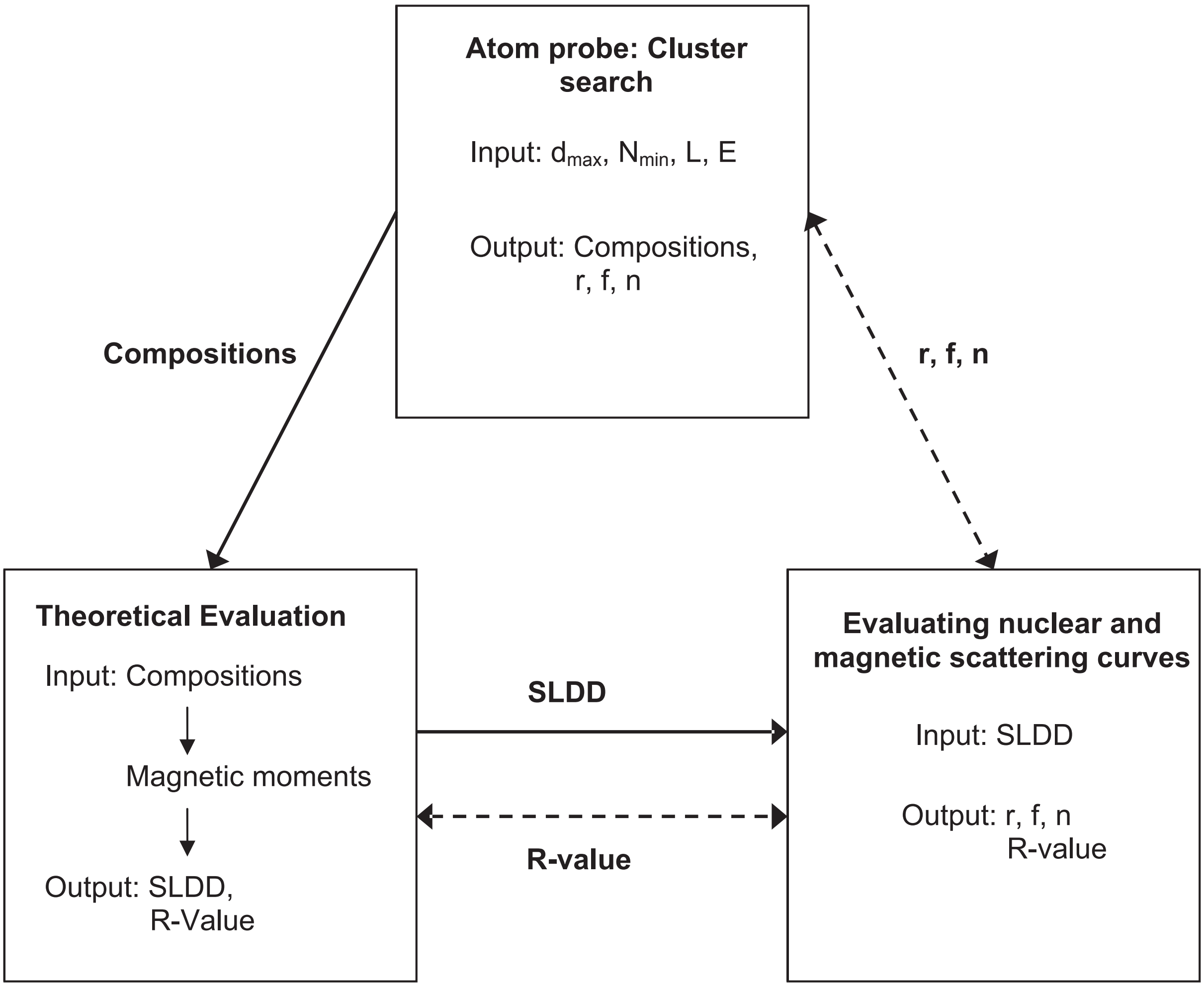

Figure 5.1: Flow chart of the connections of the determined 3DAP data and SANS data.

3DAP data were evaluated via a cluster search algorithm as described in chapter 3.6.3. Information on the compositions, the mean particle radius r, the precipitated volume fraction f and the number density n is the result. The obtained compositions of the precipitates as well as of the matrix are used to calculate the magnetic and nuclear scattering contrasts for the assumption of magnetic as well as of non-magnetic particles (see chapters 3.5.6 and 3.5.7). Hence, the theoretical R-values can be calculated and the magnetic scattering length density difference is used to quantitatively evaluate the magnetic SANS curves with respect to the radius, volume fraction and number density. The determined R-values can be compared with the R-values obtained by evaluating the magnetic and nuclear integral intensities of the measured SANS curves. This procedure allows for a critical assessment regarding the assumptions of the magnetic properties of the particles. In the following, the information on the mean radius, volume fraction and number density of the precipitates is critically compared with that obtained by the atom probe investigations.

5.2 Particle development investigated by 3DAP and SANS

Figure 5.2 presents the results obtained by 3DAP as well as by SANS for all three model alloys. The data of the evaluated SANS experiments assume the particles to be non-magnetic. It has been came to this decision since the obtained 3DAP (Table 4-3) and SANS (Table 4-4) data satisfactorily agree among each other, especially considering the precipitated volume, in case of the non-magnetic assumption. The results of the particle development according to the Fe6Al4Ni alloy are shown in Figure 5.2(a). Regarding the obtained radii of the precipitates provides a satisfactory correlation between the SANS data and the atom probe data, both techniques indicate a continuous increase. The development of the volume fraction shows a good agreement of the in-situ and the static SANS experiments but a discrepancy to the 3DAP data exists. The 3DAP offers a continuous increase of the volume fraction with running aging showing a lower value for the state aged for 3 h (10800 sec) and a higher value for the state aged for 24 h (86400 sec) as determined by SANS. The SANS data show an increase of the volume fraction up to 3 h of aging followed by a nearly constant volume fraction from the state aged for 3 h to that aged for 24 h. The number density obtained by SANS shows a decrease which opens out into a plateau. The 24 h aged static SANS sample lies on the elongation of the in-situ data and also the atom probe measurement agrees satisfactorily in case of the state aged for 24 h. Alloys Fe6Al6Ni (Figure 5.2(b)) and Fe4Al6Ni (Figure 5.2(c)) show similar radius characteristics indicating a continuous increase with ongoing aging. For both alloys the mean radius of the particles in the 24 h aged sample obtained by SANS is significantly higher than that obtained by 3DAP. The development of the number density of Fe4Al6Ni shows the same tendency as mentioned before for the Fe6Al4Ni alloy and the SANS and atom probe data agree among each other. In case of the Fe6Al6Ni alloy the number density obtained by the 3DAP is constant from the state aged for 3 h to that for 24 h whereas the SANS data provide a continuous decrease of the number density in this stage.

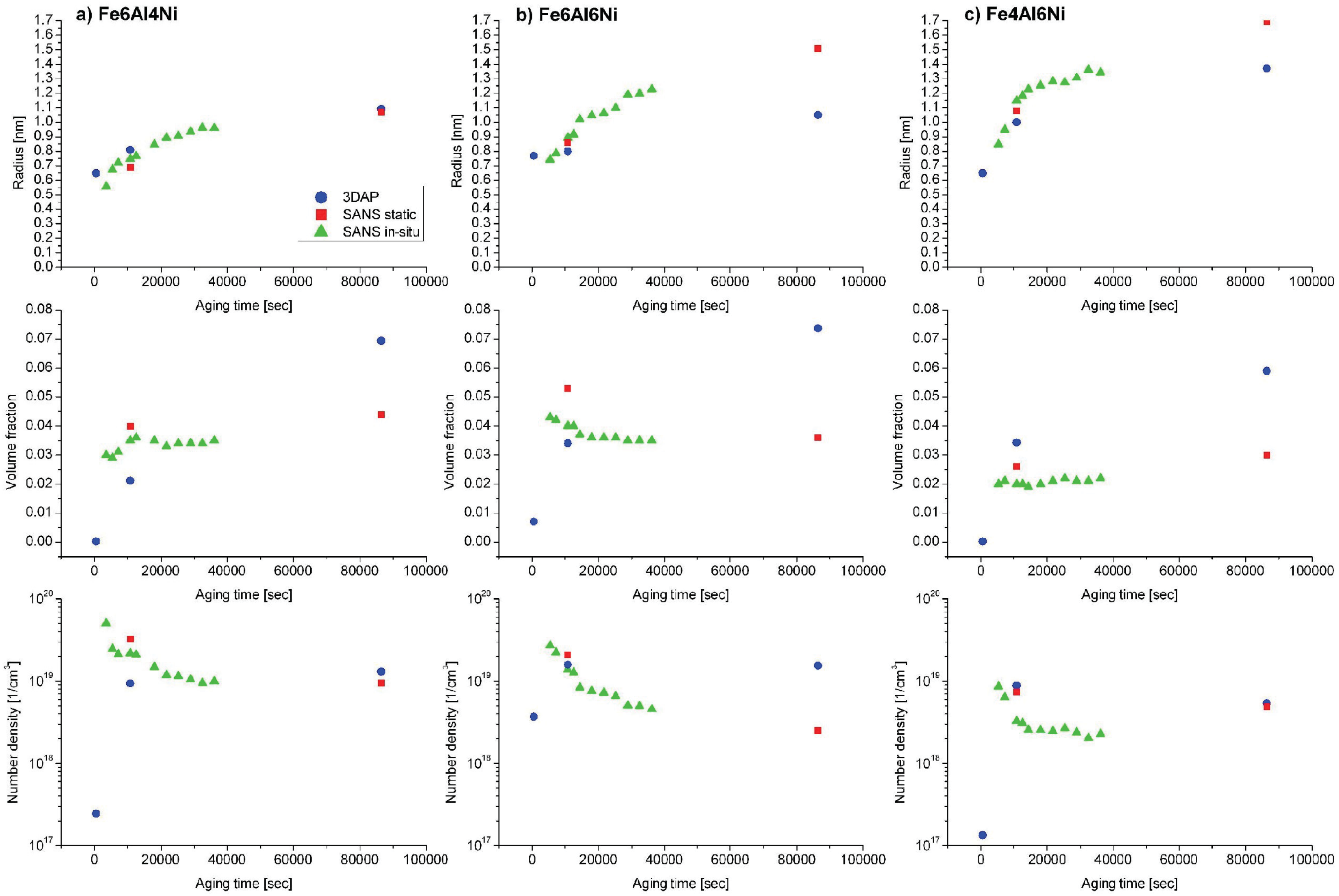

Figure 5.2: Development of radius, volume fraction and number density with increasing aging time of the three model alloys. Data obtained by 3DAP, in-situ and static SANS experiments

The developing volume fraction of the Fe4Al6Ni alloy indicates a continuously slow increase. The precipitated volume of the Fe6Al6Ni alloy shows higher values after approximately 5000 sec of aging followed by a small decrease until the volume fraction keeps constant.

In sum the 3DAP data and the SANS data agree among each other qualitatively in case of the radius and number density development as seen in Figure 5.2. The high values in number density at the beginning of aging (3600 sec) are not realized by the atom probe investigations due to the fact that this increase occurs somewhere between 10 min and 3 h of aging. After 10 min of aging the number density has not already achieved the maximum and after 3 h of aging the number density measured by the atom probe probably belongs to the region of number density decrease. The tendency of the volume fraction differs when the 3DAP data offer a much stronger continuous increase with aging time than the SANS data. For Fe4Al6Ni and Fe6Al6Ni the 3DAP data provide higher volume fractions as well. Although the data according to the radius, number density and volume fraction obtained by SANS show discrepancies to those obtained by 3DAP, tendencies of particle development are obvious. Figure 5.3 schematically illustrates the development of the number density with ongoing aging which consists of three characteristic regions.

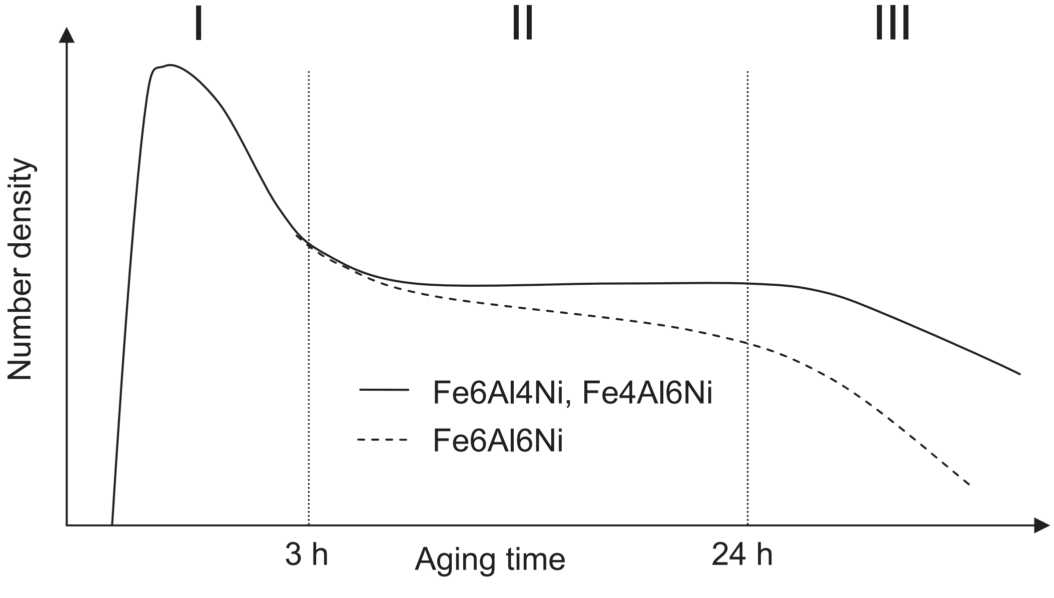

Figure 5.3: Schematic development of the number density with ongoing aging.

The solid line shows the behaviour of Fe6Al4Ni, Fe4Al6Ni and the dashed line describes the characteristic of the Fe6Al6Ni alloy. Similarities to Staron [8] are present who described the precipitation behaviour of a Ni-Al alloy by applying a cluster dynamic model. This model considers the variation of the matrix supersaturation and of the critical nucleation radius. Region I shows a rapid increase of clusters after a short time of aging which occurs due to the high super-saturation of the matrix at the beginning of the precipitation reaction. The high super-saturation leads to an extremely low nucleation barrier correlating with a small critical radius and therefore, the number density rises within a short time. This formation of a large number of small sized particles causes a decrease of the super-saturation of the matrix and the critical radius increases. When the critical radius achieves a value which is situated within the present particle distribution the clusters below the critical size are dissolved, hence, the number density decreases. The dissolution of the clusters causes a flow of Ni and Al atoms to the matrix which slows down the increase of the critical radius. The combination of creation, dissolution and growth of the clusters leads to the characteristics mentioned above and leads to a constant number density in the case of Fe6Al4Ni and Fe4Al6Ni after approximately 30000 sec. This can be seen in Figure 5.2(a, c) and is schematically illustrated in region II in Figure 5.3. Because the described processes occur simultaneously the according volume fraction shows slight fluctuations as well. According to the hardness measurements (Figure 4.1) coarsening is expected after an aging time of approximately 100 h (360000 sec) in case of Fe6Al4Ni and 24 h in case of Fe4Al6Ni. Since the theory predicts a constant volume fraction during the coarsening process the number density is expected to decrease at this stage. This is schematically depicted in region III in Figure 5.3. In case of Fe6Al6Ni the combination of creation, dissolution and growth leads to a permanent slowly decrease in number density (Figure 5.3).

The data obtained by SANS offer higher values for the radius than that obtained by 3DAP especially in the case of the 24 h aged state. Regarding the composition profiles of the precipitates depicted in Figure 4.19 shows that the interface between the matrix and the precipitate is not sharp. At a normalized particle distance of approximately 1.7 the overall matrix composition is existent which means that the range between value 1 and 1.7 can be seen as part of the interface. The precipitates' extent provided by the 3DAP evaluation is restricted to the normalized particle distance of 1. The radii obtained by the SANS data are generated by evaluating the magnetic scattering curves. Since the interface provides a magnetic scattering contrast with respect to the matrix as well the particles seem to be larger. Quantitative interpretation of the number density and volume fraction obtained by the SANS data is difficult since the magnetic moments of the particles are not known. According to the R-value investigations and considering Table 4-5 the precipitates are expected to be magnetic which is assumed to be caused by the remarkable content of remaining Fe in the precipitates. This causes a shift of the presented data for the volume fraction and number density in Figure 5.2 to higher values, hence, they approach the data obtained by the 3DAP.

5.3 Precipitation kinetics

The DSC measurements and the continuous in-situ SANS experiments provide the onset temperatures of the NiAl precipitation reaction. The nuclear and the magnetic integral intensities Q_{nuc} and Q_{mag} show different characteristics during heating as depicted in Figure 4.24. The linear increase of Q_{nuc} from the beginning of the experiment up to the transformation reaction is caused by the temperature dependence of the nuclear scattering contrast. Q_{mag} keeps obviously constant until the precipitation reaction starts due to the fact that no magnetic inhomogeneities disturb the saturation-magnetized matrix. The onset temperature obtained by SANS (Figure 4.25), which is at approximately 520 °C, shows only a weak dependence on the heating rate. In contrast the DSC measurements provide onsets in the range of 530°C (6 K/min) to 568°C (23 K/min) as illustrated in Figure 4.5. The onset difference between the curves according to heating rates of 15 and 23 K/min is approximately 5°C in case of the DSC measurements (Figure 4.5). An accurate determination of the onset in Figure 4.25 is difficult since each data point is generated by a 34 sec taking measurement and, therefore, statistic is insufficient.

Figure 4.4 shows that the DSC peaks according to the NiAl precipitation reaction are satisfactorily fitted by equation 3-22. Since the function according to Borrego et al. [54] is based on the JMA model, the transformation of NiAl precipitates in a ferritic matrix is well described by this theory. The obtained effective activation energy of 258 kJ/mol leads to the conclusion that the investigated transformation reaction is diffusion controlled since the diffusion activation energies for Ni and Al in α-iron are 245 kJ/mol [58] and 242.5 kJ/mol [59], respectively. Erlach et al. [36] provide 59.9 kJ/mol and Taillard et al. [26] approximately 80 kJ/mol for the apparent activation energy of the NiAl precipitation reaction, which is not in agreement with the apparent activation energy of 230 kJ/mol obtained in this work. In literature the transformed volume fraction data which have been achieved by the correlation either with dilatometric [26] or with hardness [28, 36] measurements have been the input to calculate kinetic parameters with respect to the Avrami law. The time exponent $n = 1$ offered by Taillard et al. [26] is smaller than that obtained in the present work ($n = 1.68$). According to Christian [5] time exponent $n = 1.5$ stands for zero nucleation rate and $1.5 < n < 2.5$ stands for decreasing nucleation rate during particle growth.

5.4 Résumé

Materials

The three model alloys Fe6Al4Ni, Fe6Al6Ni and Fe4Al6Ni have been investigated with respect to the precipitation characteristics after aging at 500°C. A remarkable amount of Fe is still in the precipitates even after aging for 24 h. The initial composition of the precipitates is correlated with the composition of the alloy. More Al or Ni in the alloy leads to higher amounts of Al or Ni in the precipitates, respectively. The Al to Ni ratio in the precipitates at early aging states is nearly the same than that in the initial alloy. During aging the Al to Ni ratio approaches a ratio of 1 and simultaneously the Fe content slowly decreases. Alloy Fe4Al6Ni, the alloy with the lowest Al content, shows the smallest precipitated volume but the largest particles after aging for 24 h. Regarding the analysis of the measured R-value of all three alloys reveals that the occurring precipitates have a magnetic moment.

Techniques

The combination of the complementary characterization methods SANS and 3DAP provides satisfactory results concerning the investigation of the NiAl precipitation process in the present work. The great advantage of the indirect method SANS is the rather large volume which is observed, providing satisfactory statistics. Particles with radii of 0.7 nm have been detected. Fitting of the scattering curves becomes difficult for smaller particles. The cluster algorithm applied to the 3DAP data restricts the detectable size of particles in the sub-nm range as well. The in-situ SANS experiments require a compromise between time resolution and statistics. For sufficient statistics the sample has to be exposed to the beam for adequate times, which restricts the frequency of measurements. An improvement in time resolution for further investigations can be a beam line with a higher flux compared to the beam line used in the present work. With the gained information on the composition of the precipitates from 3DAP data the SANS peaks can be identified. Knowledge of the compositions is also necessary to quantitatively evaluate the SANS curves. Combining the information on the compositions obtained by 3DAP and magnetic and nuclear scattering cross sections obtained by SANS allow for an assessment of the magnetic behaviour of the particles.

Generally, results obtained by SANS and 3DAP satisfactorily agree among each other. The combination of the two methods offers effective possibilities in order to investigate the early stages of a precipitation reaction.

6 Summary

The aim of the present work was the characterization of the precipitation behaviour of Ni and Al containing ferritic alloys of the nominal compositions Fe6Al4Ni, Fe6Al6Ni and Fe4Al6Ni (in at%). The alloys have been produced by balancing and melting the pure metals in a furnace under argon atmosphere. Solution annealing has been carried out at 1200°C for 5 h with subsequent water quenching, providing a super-saturated solid solution. Isothermal aging at a temperature of 500°C has been performed in order to enforce the precipitation reaction of B2 structured NiAl. Measuring the hardness after subsequent aging for different times offers three characteristic regions. A range of no or low increase in hardness, a second range of a continuous increase and a third range of a short plateau followed by a decrease in hardness. Alloys Fe6Al4Ni and Fe4Al6Ni show nearly equal hardness whereas the hardness of the Fe6Al6Ni alloy is generally higher. The different grain sizes of the alloys make the interpretation of hardness difficult. Alloys Fe6Al6Ni and Fe4Al6Ni reach the peak hardness at approximately 24 h of aging whereas alloy Fe6Al4Ni has not reached the maximum after aging for 96 h. Analogous to these measurements selected samples have been chosen to be investigated by atom probe (3DAP) and small angle neutron scattering (SANS) to obtain information on the composition of the precipitates as well as on the size, number density and volume fraction. In-situ SANS experiments have been conducted as well. Therefore, measurements have been conducted during isothermal aging at 500°C. Additionally, in order to obtain information on the precipitation kinetics DSC measurements have been performed on the alloy Fe6Al4Ni.

The precipitates have been found to be homogenously distributed in the matrix. The spherical shape is kept up to aging times of at least 24 hours. Alloys Fe6Al4Ni and Fe4Al6Ni show only a very small precipitated volume after aging for 10 min. In contrast, alloy Fe6Al6Ni presents a remarkable volume and a number density which is a magnitude higher than that of the other two alloys. Regarding the 24 h aged samples shows that the precipitates detected in Fe4Al6Ni are larger than in the other alloys but the volume fraction and the number density are smaller. The characteristics of the number density and volume fraction and the development of the particle size distribution with aging time lead to the assumption that the mechanisms of nucleation, dissolution, growth and coarsening occur simultaneously. The classical nucleation and growth theory is not applicable since the composition of the precipitates is developing while the particles are growing. The 3DAP investigations show that the initial composition of the particles depends on the overall composition of the alloy, i. g. the particles of the Fe6Al4Ni alloy contain more Al than Ni at the beginning of the precipitation reaction and contrary for the Fe4Al6Ni alloy. With subsequent aging the Ni to Al ratio approaches 1 as proposed in literature but is not reached after 24 h of aging. Even after 24 h of aging a remarkable amount of Fe atoms is present in the precipitates containing approximately 40 at%. Observing the R-value indicates that the main composition development occurs in the first 10000 sec of aging. Further aging leads to an extremely slow change in the composition caused by the decrease of Fe content in the precipitates. The R-value investigations lead to the conclusion that the investigated precipitates are in fact magnetic, which is possibly caused by the remarkable containing amount of Fe. The 3DAP measurements show a concentration gradient of Ni and Al atoms across the particles containing the highest amounts in the core and decreasing to the edge. This gradient also ranges into the matrix since the overall matrix composition is present. Hence, in case of the SANS experiments the magnetic inhomogeneities according to the precipitates appear to be larger than the particles detected by the 3DAP evaluations. The thickness of this mentioned interface between particle and matrix is in the range of the particle radii. The obtained effective activation energy of 258 kJ/mol according to the NiAl precipitation reaction confirms the transformation to be a diffusion controlled process since the activation energies of Al and Ni for diffusion in α Fe are in the same range. Additionally, a JMA exponent $n = 1.68$ has been found which stands for decreasing nucleation rate during particle growth.

7 References

1. Seetharaman V., Sundararaman M.,Krishnan R.: Precipitation hardening in a PH 13-8 Mo stainless steel, Materials Science and Engineering, 47(1): p. 1-11, (1981).
2. Miller M. K.: Atom probe field ion microscopy, Clarendon Press ; Oxford University Press, (1996).
3. Reimers W., Pyzalla A.R., Schreyer A., Clemens H.: Neutrons and Synchrotron Radiation in Engineering Materials Science, Wiley-VCH, (2008).
4. Gottstein G.: Physical foundations of materials science, Springer, (2004).
5. Christian J.W.: The theory of transformations in metals and alloys, (1981).
6. Porter D. A., Easterling K. E.: Phase transformations in metals and alloys, Van Nostrand Reinhold, (1981).
7. Cahn R. W., Haasen P., Kramer E. J.: Materials science and technology : a comprehensive treatment, 5, VCH, (1991).
8. Staron P.: Frühstadien der Entmischung in einer Ni-13at%Al-Legierung - polarisierte Neutronen-Kleinwinkelstreuung und clusterdynamische Modellierung, Universität Hamburg, (1997).
9. Bergmann W.: Werkstofftechnik,
10. Sauthoff G.: Intermetallics, VCH, (1995).
11. http://cst-www.nrl.navy.mil/lattice/, (2009).
12. Schultz P. A., Davenport J. W.: Calculations of systematics in B2 structure 3d transition metal aluminides, Journal of Alloys and Compounds, 197(2): p. 229-242, (1993).
13. Fox A. G., Tabbernor M. A.: The bonding charge density of β'NiAl, Acta Metallurgica et Materialia, 39(4): p. 669-678, (1991).
14. Miracle D. B.: Overview No. 104 The physical and mechanical properties of NiAl, Acta Metallurgica et Materialia, 41(3): p. 649-684, (1993).
15. Bradley A.J.: Microscopical studies on the iron-nickel-aluminium system Part I, Journal of the Iron and Steel institute, 163(19-30, (1949).
16. Bradley A.J.: Microscopical studies on the iron-nickel-aluminium system Part II, Journal of the Iron and Steel institute, 168(233-244, (1951).
17. Rivlin V.G., Raynor, G.V.: Critical evaluation of constitution of aluminium-iron-nickel system, International Metals Reviews, 25(3): p. 79-93, (1980).
18. Budberg P., Prince A.: Ternary alloys, VCH: Weinheim, (1992).
19. Eleno L., Frisk K., Schneider A.: Assessment of the Fe-Ni-Al system, Intermetallics, 14(10-11): p. 1276-1290, (2006).
20. Raghavan V.: Al-Fe-Ni (aluminum-iron-nickel), Journal of Phase Equilibria and Diffusion, 26(1): p. 70-71, (2005).
21. Raghavan V.: Al-Fe-Ni (aluminum-iron-nickel), Journal of Phase Equilibria and Diffusion, 27(5): p. 489-490, (2006).
22. Raghavan V.: Al-Fe-Ni (Aluminum-Iron-Nickel), Journal of Phase Equilibria and Diffusion, 29(2): p. 180-184, (2008).
23. Chumak I., Richter K.W., Ipser H.: Isothermal Sections in the (Fe, Ni)-Rich Part of the Fe-Ni-Al Phase Diagram, Journal of Phase Equilibria and Diffusion, 29(4): p. 300-304, (2008).
24. Chumak I., Richter K.W., Ipser H.: The Fe-Ni-Al phase diagram in the Al-rich (>50 at.% Al) corner, Intermetallics, 15(11): p. 1416-1424, (2007).

25. Blavette D., Martin C., Gallot J.: Analyse a la sonde atomique de precipites dans un alliage Fe Cr20 Ni2 Al2, Scripta Metallurgica, 16(1): p. 59-64, (1982).
26. Taillard R., Pineau A., Thomas B.J.: The precipitation of the intermetallic compound NiAl in Fe-19wt.%Cr alloys, Materials Science and Engineering, 54(2): p. 209-219, (1982).
27. Decker R.F., Floreen S.: Maraging Steels - the 1st 30 Years, Journal of Metals, 39(10): p. A6-A6, (1987).
28. Robino C., Cieslak M., Hochanadel P., Edwards G.: Heat treatment of investment cast PH 13-8 Mo stainless steel: Part II. Isothermal aging kinetics, Metallurgical and Materials Transactions A, 25(4): p. 697-704, (1994).
29. Guo Z., Sha W., Vaumousse D.: Microstructural evolution in a PH13-8 stainless steel after ageing, Acta Materialia, 51(1): p. 101-116, (2003).
30. Ping D.H., Ohnuma M., Hirakawa Y., Kadoya Y., Hono K.: Microstructural evolution in 13Cr-8Ni-2.5Mo-2Al martensitic precipitation-hardened stainless steel, Materials Science and Engineering A, 394(1-2): p. 285-295, (2005).
31. Cloué J.-M., Viguier B., Andrieu E.: Effect of the metallurgical variables on the yield stress of PH 13-08 steel, Metallurgical and Materials Transactions A, 36(10): p. 2633-2639, (2005).
32. Garrison Jr. W.M., Strychor, R.: Preliminary study of the influence of separate and combined aluminum and nickel additions on the properties of a secondary hardening steel, Metallurgical transactions A, 19 A(12): p. 3103-3107, (1988).
33. Erlach S., Danoix F., Lemarchand D., Leitner H., Bischof M., Siller I., Clemens H.: On the precipitation behaviour of a Ni and Al alloyed martensitic tool steel, Materials Science and Technology, 1(633-641, (2004).
34. Erlach S., Danoix F., Leitner H., Auger P., Siller I., Clemens H.: Precipitation reactions during the early stages of aging in a Ni and Al alloyed martensitic medium carbon steel, Surface and Interface Analysis, 39(2-3): p. 213-220, (2007).
35. Erlach S., Leitner H., Bischof M., Clemens H., Danoix F., Lemarchand D., Siller I.: Comparison of NiAl precipitation in a medium carbon secondary hardening steel and C-free PH13-8 maraging steel, Materials Science and Engineering: A, 429(1-2): p. 96-106, (2006).
36. Erlach S., Siller, I., Leitner, H., Clemens, H.: Isothermal aging kinetics of NiAl precipitates in a secondary hardening steel, International Journal of Microstructure and Materials Properties, 3(2-3): p. 373-382, (2008).
37. Hamano R.: Effect of the precipitation of coherent and incoherent precipitations on the ductility and toughness of high-strength steel, Matallurgical Transactions A, 24A(127-139, (1993).
38. Calderon H., Fine M., Weertman J.: Coarsening and morphology of β′ particles in Fe-Ni-Al-Mo ferritic alloys, Metallurgical and Materials Transactions A, 19(5): p. 1135-1146, (1988).
39. Calderon H.A., Kostorz G., Qu Y.Y., Dorantes H.J., Cruz J.J., Cabanas-Moreno J. G.: Coarsening kinetics of coherent precipitates in Ni-Al-Mo and Fe-Ni-Al alloys, Materials Science and Engineering A, 238(1): p. 13-22, (1997).
40. Cayetano-Castro N., Dorantes-Rosales H.J., López-Hirata V.M., Cruz-Rivera J.J., Moreno-Palmerin J., González-Veláquez J.L.: Coarsening kinetics of coherent precipitates in Fe-10 % Ni-15 % Al alloy, Revista de Metalurgia (Madrid), 44(2): p. 162-169, (2008).

41. Satyanarayana D.V.V., Malakondaiah G., Sarma D.S.: Steady state creep behaviour of NiAl hardened austenitic steel, Materials Science and Engineering A, 323(1-2): p. 119-128, (2002).
42. Stallybrass C., Schneider A., Sauthoff G.: The strengthening effect of (Ni,Fe)Al precipitates on the mechanical properties at high temperatures of ferritic Fe-Al-Ni-Cr alloys, Intermetallics, 13(12): p. 1263-1268, (2005).
43. Schatz G., Weidinger, A. : Nukleare Festkörperphysik, Teubner, (1992).
44. Kostorz G.: Neutron scattering, 15, Academic Press, (1979).
45 http://www.gkss.de/central_departments/genf/instruments/003124/index 0003124.html.de, (2009)
46. Guinier A., Fournet G.: Small-angle scattering of X-rays, Wiley, (1955).
47. Bacon G.E.: Neutron diffraction, Oxford Univ. Press, (1975).
48. Glatter O.: A new method for the evaluation of small-angle scattering data, Journal of Applied Crystallography, 10(5): p. 415-421, (1977).
49. Glatter O.: Determination of particle-size distribution functions from small-angle scattering data by means of the indirect transformation method, Journal of Applied Crystallography, 13(7-11, (1980).
50. Leitner H., Staron P., Clemens H., Marsoner S., Warbichler P.: Analysis of the precipitation behaviour in a high-speed steel by means of small-angle neutron scattering, Materials Science and Engineering A, 398(1-2): p. 323-331, (2005).
51. Vaumousse D., Cerezo A., Warren P.J.: A procedure for quantification of precipitate microstructures from three-dimensional atom probe data, Ultramicroscopy, 95(215-221, (2003).
52. Schmölzer T.: Microstructural investigation of a Fe-Co-Mo alloy be means of SANS and atom probe analysis, Diploma thesis, Department for physical metallurgy and materials testing, Montanuniversität Leoben, (2008).
53. Guo Z., Sha W., Li D.: Quantification of phase transformation kinetics of 18 wt.% Ni C250 maraging steel, Materials Science and Engineering A, 373(1-2): p. 10-20, (2004).
54. Borrego A., González-Doncel G.: Calorimetric study of 6061-Al-15 vol.% SiCw PM composites extruded at different temperatures, Materials Science and Engineering A, 245(1): p. 10-18, (1998).
55. Höhne G.W.H., Hemminger W., Flammersheim H.-J.: Differential Scanning Calorimetry, Springer-Verlag, (1996).
56. Setaram Instrumentations, User manual Labsys Evo,
57. Staron P.: Einführung in die Nutzung von Streumethoden in der Werkstoffforschung, Vorlesungsskriptum SS 2008, (2008).
58. Gröbner P.: Hutn. Listy, 10: p. 200, (1955).
59. Hirano K., Cohen M., Averbach B.L.: Acta Metallurgica, 9(440, (1961).